N°03/2023

PEOPLE'S DEMOCRATIC REPUBLIC OF ALGERIA
MINISTRY OF HIGHER EDUCATION AND SCIENTIFIC RESEARCH
UNIVERSITY OF ECHAHID CHEIKH LARBI TEBESSI - TEBESSA
FACULTY OF SCIENCE AND TECHNOLOGY

THESIS

Presented for obtaining the diploma of

3^{rd} **Cycle LMD DOCTORATE**

In : **AUTOMATIC**

Speciality: Automatic and Systems

by : **Meriem Mebarkia**

TITLE

Advanced Image Content Analysis Techniques Applied to Medical Imaging

Discussed publicly at: 2023 in front of the assessment committee:

Mahmoud Maameri	*Lecturer A*	*Echahid Cheikh Larbi Tebessi University*	*Chairman*
Hakim Bendjenna	*Professor*	*Echahid Cheikh Larbi Tebessi University*	*Examiner*
Toufik Thelaidjia	*Lecturer A*	*Mohamed-Chérif Messaadia University*	*Examiner*
Laatra Yousfi	*Lecturer A*	*Echahid Cheikh Larbi Tebessi University*	*Examiner*
Abdallah Meraoumia	*Professor*	*Echahid Cheikh Larbi Tebessi University*	*Supervisor*
Lotfi Houam	*Lecturer B*	*Echahid Cheikh Larbi Tebessi University*	*Co-supervisor*

بسم الله الرحمن الرحيم

وقل رب زدني علما

صدق الله العظيم

بِسۡمِ ٱللَّهِ ٱلرَّحۡمَٰنِ ٱلرَّحِيمِ

To Allah, The Almighty; who gave me the strength and patience to finish this work.

There are a number of people without whom this dissertation might not have been written, and to whom I am greatly indebted.

To my dear parents who have always been a source of encouragement. You Were an inspiration to me throughout my life. You taught me the sense of responsibility, hard work, and happiness. May Allah bless your lives and give you eternal happiness.

I dedicate this dissertation to all of my beloved brothers and sisters who have supported me throughout the process. I will always appreciate what you have done.

I dedicate this dissertation to all of my family. You are all a true manifestation of love and support.

Finally, I dedicate this thesis to my best friends whom I have shared a great time with and spent countless hours learning and enjoying life.

Meriem Mebarkia

Acknowledgment

In the name of ***Allah****, the Most Gracious and the Most Merciful*

Alhamdulillah, all praises to ***Allah*** *for giving me the courage and the patience finish this thesis..*

My sincere thanks and gratitude to Mr. ***Abdallah Meraoumia****, my thesis supervisor and Professor at Cheikh Larbi Tebessi University in Tebessa, for his scientific support, his availability, his judicious orientations and whose intellectual skills, experience, modesty and patience have greatly contributed to the completion of this thesis. May he find here the expression of my deep respect.*

I would also like to thank Mr. ***Lotfi Houam****, Professor at Cheikh Larbi Tebessi University, for his permanent follow-up, his availability and his practical advice which helped me to better approach and design the subject of the thesis.*

I would particularly like to thank all the members of the jury who have done me the honor of agreeing to read and judge this work. Much appreciation and gratitude to all the teachers of the Electrical Engineering Department of Cheikh Larbi Tebessi University for their help and advice, especially Professor ***Seddik Khemaissia****. As well as all the staff of the LABGET and LAMIS laboratory.*

Finally, I would like to thank everyone who has contributed directly or indirectly to the completion of this work.

Abstract

Artificial Inteligence (AI) techniques like Machine Learning (ML) and Deep Learning (DL) have the potential to revolutionize healthcare by helping doctors and healthcare professionals to analyze and diagnose patient data and images more accurately and efficiently. The integration of methods and techniques that support more effective clinical diagnosis based on images obtained from various imaging modalities, which have become increasingly widely and successfully used to detect illnesses, is necessary for a correct diagnosis, which necessitates the precise identification of each disease. Texture analysis involves the use of computer algorithms to analyze the spatial distribution of gray levels in an image of a bone sample. This analysis can provide information about the size, shape, and orientation of the bone's microstructure, which can be used to estimate the degree of osteoporosis. Despite the substantial correlation between sick and healthy bones, the limited results of the majority of this context's research result from the use of handcrafted methods to directly extract bone image features. To bring performance closer to clinical diagnosis, novel learning, optimization, and inference methods for processing biomedical and healthcare data must be investigated. In this work, a set of descriptors derived from a thorough study of bone texture images will be applied to a handcrafted feature extraction method (such as HOG and/or LPQ) using Gabor's filter bank. In addition, the classifier uses bat-inspired algorithm-based optimization to automatically adjust the Gabor filter settings in order to achieve deep analysis behavior and optimal performance. With a good performance of 89.66 % for Osteoporosis diagnosis, our experimental results using a standard osteoporosis database demonstrate a significant improvement over current Deep/Handcrafted methods. Deep Feature Analysis enables the model to automate the extraction of relevant features and complete the necessary classification. By automating the feature extraction process, deep feature analysis can significantly improve the accuracy and efficiency of classification tasks.

Contents

List of Figures

List of Tables

Chapter 1

General Introduction

Healthcare systems play a vital role in maintaining the well-being of individuals and communities by providing care for their physical and mental health. These systems have been in place since the time people started prioritizing their health and seeking medical attention for illnesses. However, the healthcare landscape is evolving as people's lifestyles and technological advancements are changing rapidly. Although life expectancy has increased in recent decades, it is projected to change significantly due to the aging population. The number of people aged 65 or older is expected to double by 2050, and the majority of illnesses are predicted to be linked to chronic comorbid conditions by 2025. As the population ages, healthcare costs are also expected to rise. Therefore, healthcare procedures must be modified to meet the growing demand for care, as suggested by Bohr & Memarzadeh (2020). In addition, primary care services must ensure equitable access to curative, rehabilitative, and palliative care services. To strengthen healthcare systems, the health emergency protection domain aims to provide adequate and timely services to prevent and manage disease outbreaks, while the universal health coverage domain focuses on preventing and treating communicable and noncommunicable diseases and addressing the health impacts of climate change.

In recent years, public health has emerged as a critical global concern, highlighting the need to establish rigorous technical standards to measure and ensure the quality of public health practices. While public health is undoubtedly vital, the increasing number of patients and the use of conventional diagnostic methods for various diseases can burden healthcare providers and compromise the efficiency of diagnosis and care delivery. Nonetheless, recent technological advancements, particularly in automation, have the potential to significantly enhance the efficiency and effectiveness of healthcare delivery, while simultaneously reducing the time and costs associated with patient care. These technological innovations have the potential to revolutionize healthcare systems, eliminating the need for extensive and expensive infrastructure projects. Although technological advancements in the field have been made, misdiagnosis and missed diagnoses persist, particularly in the emergency department, which creates challenges for healthcare administrators. Scientists, legislators, and successful businesspeople assert that Artificial Intelligence (AI) will be an essential component of the solution to address the deteriorating outcomes of healthcare systems. Thus, as the population continues to grow, the demand for healthcare services is expected to increase. Consequently, the healthcare industry is actively pursuing innovative methods to enhance efficiency and effectiveness while minimizing costs. One approach to achieving this goal is by leveraging rapid technological advancements, particularly in the field of AI.

The use of AI in clinical applications has been gaining attention due to its potential to replicate human perception, reasoning, learning, and problem-solving methods [1]. One notable application of AI is in classical statistical approaches, where it can extract data that improves research and decision-making across various clinical research sectors and technology domains [2]. A press survey reported that 63% of respondents believe that AI and machine learning (AI/ML) is already delivering significant benefits to specialist fields such as radiology, general medicine, and pathology [3]. In fact, AI is gradually replacing traditional public health as it aids in risk prediction through improved diagnostics and screening. With the use of an AI-powered screening model, potential dangers and vulnerabilities of diseases and disorders can be identified. The most promising application of AI in healthcare is its ability to enhance intelligence. Data-driven treatment recommendations that physicians and nurses can quickly accept, modify, or reject based on their experience and expertise can improve their performance. By combining augmented intelligence with human intelligence, gaps can be addressed, and human errors can be reduced. On the other hand, the future of healthcare is closely intertwined with that of machine learning and artificial intelligence. Medical professionals and researchers input data into computers, which are then utilized to analyze, comprehend, and resolve issues. The potential uses of artificial intelligence in the medical field are vast and diverse [4].

In 2012, the term "radionics" was first introduced by Dutch researcher Lambin P [5]. His definition of "radionics" is "the extraction of a large number of image features from radiographs using high-throughput technology." As more medical images are generated and artificial intelligence becomes increasingly prevalent, radionics is experiencing rapid growth. In fact, radiological data such as intensity, shape, texture, and wavelength can be extracted from medical images [1] and used in diagnostic procedures or in combination with them. One of the most promising applications of artificial intelligence is image processing and analysis, which leads us to radiology. Even the most complex issues can be resolved when machine learning systems are fully utilized. Some early examples include computer-assisted breast cancer diagnosis on mammograms, automatic bone age calculation on plain X-ray images of the hand, and identification and definition of lung nodules on CT scans.

During the past decade, the volume of medical imaging data has significantly increased, making it difficult for doctors to effectively process and understand images. However, this issue has also presented opportunities for artificial intelligence to flourish in medical imaging-related research. Researchers in radiology have successfully used AI to analyze images and determine results that may not be visible to the naked eye. For example, in radiation therapy for tumors, AI can be successfully used to automatically determine the segments of tumors and organs and monitor the tumor during adaptive therapy [3] [6]. This makes it easier to predict treatment response, distinguish between benign and malignant elements, and evaluate patient outcomes using machine learning.

Medical imaging is an important diagnostic tool for various diseases. X-rays were the first diagnostic imaging tool after Roentgen's discovery that they could be detected in the human body without invasive procedures in 1895 [7]. Since then, more advanced imaging procedures and several imaging techniques, such as computed tomography, ultrasonography, magnetic resonance imaging, and positron emission tomography, have been developed. Imaging information is critical for decision-making at various stages of patient care, including detection, characterization, staging, treatment response evaluation, disease recurrence monitoring, and guidance for radiological treatments, surgery, and radiation. The number of images has significantly increased from a few two-dimensional (2D) images to hundreds of three-dimensional and thousands of dynamic four-dimensional images in a single patient case. Multimodal imaging further increases the amount of image data that must be interpreted. As workloads increase, radiologists and clinicians face a challenge of utilizing all available visual information to improve accuracy and patient care while maintaining efficient workflows. Recent advancements in machine learning and computational methods have identified the development of efficient and dependable computerized methods as a crucial area of medical imaging research to assist radiologists and physicians in image analysis at various stages of disease diagnosis and management during the patient care process [8].

1.1 Motivation and Goal

Osteoporosis is a condition that affects the skeleton and is characterized by changes in bone microarchitecture and reduced bone density, which can lead to increased bone fragility and a higher risk of fractures. Considerable research has been conducted on osteoporosis, including the clinical implications of bone fractures. In fact, it's estimated that osteoporotic fractures will affect around 50% of women and 20% of men over their lifetime [2]. Recently, advances in machine learning (ML) have enabled significant progress in analyzing complex data sets with high-dimensional connections that are difficult for humans to detect. Despite the technical and clinical challenges associated with applying machine learning techniques in the field of osteoporosis, it holds great promise as a way to improve diagnosis and treatment of the disease.

To diagnose osteoporosis, the standard approach is to assess Bone Mineral Density (BMD) using Dual-energy X-ray Absorptiometry (DXA) at the proximal thigh and lumbar spine. The American Working Group on Preventive Services recommends screening for osteoporosis in women over the age of 65 to prevent osteoporotic fractures [9]. Since early treatment can be more effective in preventing fractures, early diagnosis of osteoporosis is essential [10]. One limitation of DXA is that it can be affected by measurement errors caused by surrounding soft tissue [11]. Moreover, the high cost and radiation exposure associated with DXA are additional drawbacks [12]. Identifying patients at risk of bone fractures is a challenging task in osteoporosis [13]. To address this issue, researchers are exploring the use of machine learning classifiers that can predict osteoporotic bone fractures based on imaging features and anatomical regions that have the greatest impact on prediction accuracy [14]. Identifying patients at risk for fractures is a significant challenge in the field of osteoporosis, and finding machine learning classifiers that highlight imaging features and anatomical regions that have the greatest impact on data-driven predictions is crucial. Machine learning (ML) can play a significant role in diagnosing opportunistic osteoporosis or detecting fractures by analyzing images. However, the challenge lies in the fact that osteoporotic and healthy images share many similarities, making it difficult for human radiologists to distinguish between them. Future research aims to create machine-learning models that can better predict fractures and identify new risk factors. Radiologists use the output of computerized schemes for automated image analysis to aid in their diagnoses. The performance of computers need not be superior to that of doctors; rather, it should complement their abilities and serve as a second opinion. Computer-Aided Diagnosis (CAD) has been introduced to assist experts and other clinicians in detecting osteoporosis disease and improving diagnosis accuracy.

1.2 Contribution

Feature extraction is a crucial step in image-based medical diagnostic systems to ensure reliable and useful recognition results. However, traditional machine learning techniques like Support Vector Machine (SVM) rely on handcrafted features that are limited by human developers' inability to translate complex illness patterns into a small number of descriptors. Consequently, existing machine learning techniques are limited even when observing a large patient population. Moreover, the variations in normal and abnormal patterns within a population make it challenging to tolerate Handcrafted features. We have developed a method for feature extraction that aims to increase class interaction while minimizing class interdependence. Our innovative techniques allow for multi-scale image analysis to extract features that improve the precision of feature vectors, ultimately increasing the accuracy of pattern recognition systems. While we faced challenges, particularly when using the datasets mentioned in Appendix A, our data is so similar between classes that it is difficult for a human to differentiate between healthy and osteoporosis images without aid. Our main contributions in this context are outlined below:

- To start the process, the raw image will be subjected to a thorough analysis using a designated group of Gabor filters before the direct application of the handcrafted feature extraction method. The Gabor filters extract multiple line orientations and merge them into a single descriptor.

- Once the raw image has been analyzed using the Gabor filters, the resulting descriptor will be subjected to two unique feature extraction methods: Histogram of Oriented Gradient (HOG) and Local Phase Quantization (LPQ).
- In order to optimize its performance and achieve deep analysis behavior, the classifier uses a technique inspired by bats to adjust the Gabor filter settings. This optimization method enhances the classifier's ability to process data efficiently.
- The proposed method can implement the multimodality principle in two ways. Firstly, it can combine data from HOG and LPQ. Secondly, it can employ a texture analysis that is based on multiple filter sizes.

According to the experimental results, the deep texture analysis method for bone images is considerably more precise than previous studies.

1.3 Structure of the Thesis

This thesis describes a supervised learning algorithm for building various models to test the efficiency of feature extraction methods based on osteoporosis image texture analysis. We utilized state-of-the-art feature extraction techniques to further demonstrate the efficiency of our method. The support vector machine (SVM) was highly effective in distinguishing features, resulting in improved accuracy in osteoporosis detection. Our results demonstrate the effectiveness of the proposed method, which compares favorably to existing literature.

The thesis is divided into five chapters. In Chapter 2, modern computer-aided diagnostics are discussed. Chapter 3 provides a general overview of the skeletal and bone systems before focusing on bone diseases specific to osteoporosis. Chapter 4 outlines the concept behind the suggested method. Chapter 5 evaluates the proposed method, presents the results, and compares them to recent approaches in the literature using a public database. Finally, the thesis concludes with a general conclusion that includes the perspectives to be considered.

Chapter 2

Computer Aided Diagnosis

2.1 Introduction

Computer-Aided Diagnosis (CAD) systems have been developed to improve the accuracy of medical examinations, promote consistency in image interpretation, aid in prognostic assessment, and assist in therapeutic decision-making [16]. Although these systems have significant potential, their use in routine clinical practice remains limited. However, with the emergence of Artificial Intelligence and big data, efforts are being made to overcome these limitations, expand the use of CAD tools, and bring radiology closer to the concepts of a multidisciplinary approach and precision medicine [18].

According to Carlos Caldas, Professor of Cancer Medicine and Director of the Breast Cancer Research Unit at the University of Cambridge, the study greatly enhances our understanding of the biological mechanisms underlying the response to chemotherapy in breast cancer patients [19]. By incorporating this knowledge into a Machine Learning framework that uses predictive methods, the study was able to predict the response to treatment before it was administered, based on analysis of the primary tumor and the tumor microenvironment (i.e., surrounding blood vessels, immune cells, and fibroblasts).

2.2 Clinical Diagnosis of the disease

Medical diagnosis is the process of identifying a disease or condition that explains a person's signs and symptoms. In the case of cancer, Doctors may use one or more approaches for diagnosis:

2.2.1 Physical Examination

A Medical Examination, also known as a Physical Examination, is a routine medical examination once a year that aims to check a person's physical health and note any changes or signs indicating possible health problems. A person does not have to be sick to have a thorough medical and physical examination, this is also an opportunity to speak with a doctor about any pain or symptoms they are having, which is especially important for people over the age of 50. The physical exam is typically performed by a medical professional in a doctor's office or private hospital [20], and it may begin with areas of the patient's body that have lumps that could indicate cancer. During the physical exam, the expert can look for any abnormalities, such as a change in skin color or enlargement of an organ, that could indicate cancer.

Benefits of a Physical Examination [21] [22]:

- Early detection of any disease symptoms and confirmation of possible diseases, aid in the initiation of treatment.
- Increase the chances of complete recovery and avoid any serious complications.
- Determine whether the patient has any problems or risk factors that could lead to disease in the future.
- Determine if the patient needs additional tests and investigations.
- Updating the patient's vaccinations as needed.
- Ensure that the patient maintains a healthy lifestyle.
- Develop a relationship between the patient and the caregivers.

2.2.2 Laboratory Tests

Laboratory tests, such as urine and blood tests, can help in the detection of abnormal changes that may be caused by cancer, it is used for:

- Confirmation of the diagnosis of the disease: some of these tests are confirmatory, and others are indicative of the disease, such as:
  - Bone marrow examination for the type of leukemia.
  - Hemoglobin for the diagnosis of anemia
  - Thyroid function tests to diagnose hypo or hyperthyroidism.
  - Widal's test for the diagnosis of enteric fever.
- Aid in Differential Diagnosis: Laboratory tests help diagnose diseases such as:
  - TLC for acute appendicitis or other cause.
  - LFT to determine the type of jaundice.
- To know the prognosis: Laboratory tests help to know the progress of the disease, such as:
  - ESR in case of tuberculosis.
  - Tumor markers in the treatment of cancers.
- To determine the prognosis: Laboratory tests such as those listed below can help determine the progression of the disease.
  - Chemotherapy for ovarian cancer.
  - Kidney function tests in nephrology.
  - INR in anticoagulant therapy.
- Screening tests: Laboratory tests are carried out in the form of panels to diagnose the disease in the community, such as:
  - Examination in the donor blood bank.

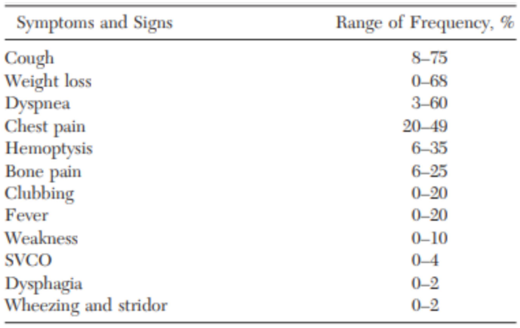

Symptoms and Signs	Range of Frequency, %
Cough	8–75
Weight loss	0–68
Dyspnea	3–60
Chest pain	20–49
Hemoptysis	6–35
Bone pain	6–25
Clubbing	0–20
Fever	0–20
Weakness	0–10
SVCO	0–4
Dysphagia	0–2
Wheezing and stridor	0–2

Figure 2.1: Range of Frequencies of Initial Symptoms and Signs of Lung Cancer [23]

2.2.3 Imaging Examination

Imaging examinations allow the examination of bones and internal organs in a non-invasive way. CT scans, bone scans, magnetic resonance imaging, positron emission tomography, ultrasound, x-rays, and other imaging tests can be used to diagnose disease. This element will be discussed in more detail in the next Chapter.

2.2.4 Biopsy

A biopsy is a procedure in which a sample of tissue from the body is removed for examination. Biopsy specimens can be obtained in a variety of ways. Needle biopsy is used when a lesion or tumor can be felt or identified in imaging studies [24]. During the procedure, a thin, hollow needle is inserted into the lesion and guided through an X-ray or ultrasound machine. A small amount of tissue is taken for examination. Doctors use a microscope to examine cell samples:

- **Normal Cells:** appear uniform and similar in size and organization.
- **Cancer Cells:** appear less organized and appear in different sizes and without a clear arrangement.

The appropriate biopsy procedure is determined by the type and location of cancer, in most cases, a biopsy is the only way to confirm a diagnosis of cancer.

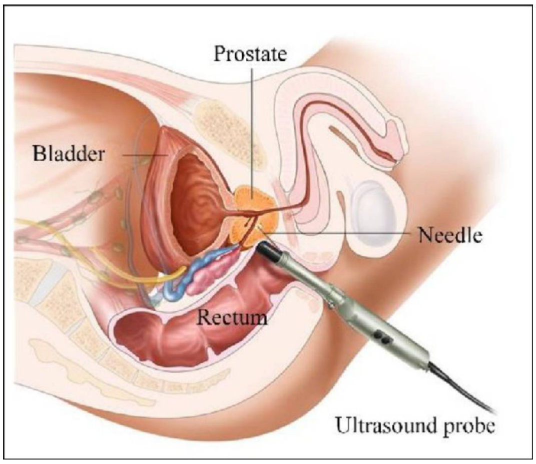

Figure 2.2: Schematic drawing of a biopsy procedure illustrates how a forward viewing probe captures images of the prostate and nearby organs bladder and urethra [25].

2.3 Artificial Intelligence and Diagnosis: Interest, impact, and trend

In 1956, John McCarthy introduced the concept of Artificial Inteligence (AI). His definition of AI is "the science and engineering of creating intelligent machines". Artificial intelligence is the development of computer systems capable of performing tasks that require human intelligence, such as decision-making, object detection, complex problem-solving, and so on [26].

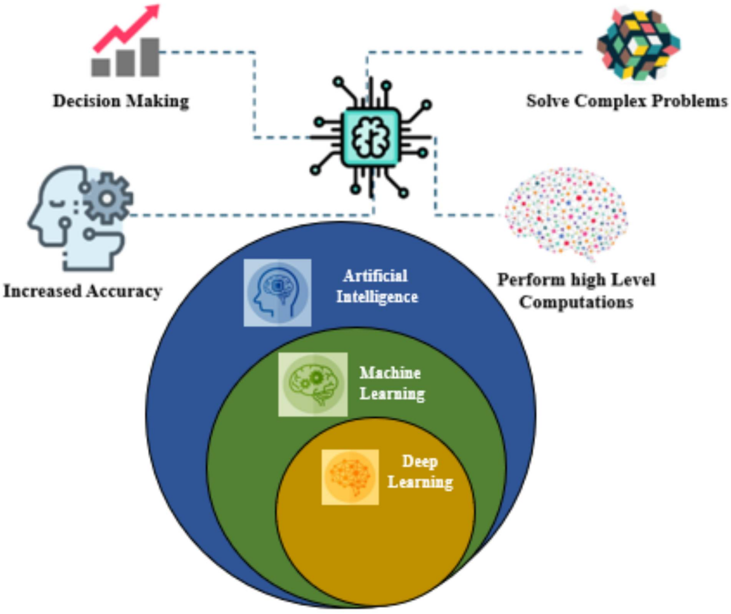

Figure 2.3: Relationship between Artificial Intelligence, Machine Learning, and Deep Learning

2.3.1 Types of Artificial Intelligence

There are four primary AI types, according to the current classification system: Reactive, Limited Memory, Theory of Mind, and Self-award. These four types are not all the same: Some are far more advanced than others [27]. Some of these AI systems are not even scientifically feasible right now.

1. Reactive systems

The reactive system is the oldest and most basic type of artificial intelligence. These systems have a single function, no memory, and no comprehension of the world outside of their function, even though they approximate the human mind in how they react to specific stimuli.

Such Artificial intelligence has machines that only operate based on the data that is now available and only take into consideration the current circumstances. Reactive AI devices are unable to conclude the data to evaluate their potential course of action. They can only carry out a small number of predetermined duties.

The well-known IBM chess software that defeated Garry Kasparov as the world champion is an illustration of reactive AI. It understands the pieces on the board and predicts possible next moves, it selects what it considers to be the best profitable outcome based on a limited set of rules. but without learning from the past. It only reacts after seeing what is in front of it.

Reactive machine learning is an extension of the reactive systems approach that addresses the specific challenges of building machine learning systems.

2. Limited Memory

Is a Reactive Learning System, a category that encompasses practically all of today's working AI tools. By observing actions or data, Limited Memory AI learns from the past and accumulates experiential knowledge. This type of AI makes predictions and performs complex classification tasks by combining historical observational data with pre-programmed information.

3. Theory of Mind

Machines will acquire true decision-making abilities similar to humans with this type of AI. Machines equipped with the theory of mind AI will be able to understand and remember emotions, and then adjust their behavior in response to those emotions as they interact with humans [29].

4. Self-award

The final stage of AI development involves creating systems that can form representations of themselves. In some ways, this is an extension of the "theory of mind" that Type III artificial intelligence have. Consciousness is also known as "self-awareness" for a reason. Conscious beings are aware of themselves, their internal states, and their ability to predict the feelings of others.

2.3.2 Branches of Artificial Intelligent

The fields of application and potential uses of Artificial Intelligence are increasingly diverse: Natural language Processing [17], visual recognition, Robotics, Expert systems, Machine Learning, Deep Learning, and Fuzzy logic. In this section, we will focus on the Machine and Deep Learning detail.

Machine Learning

Machine Learning (ML) is the technique that enables computers to learn without being programmed [15], and it is in use daily, it is the study of using computers to read, analyze, and process data to solve real-world problems [30].

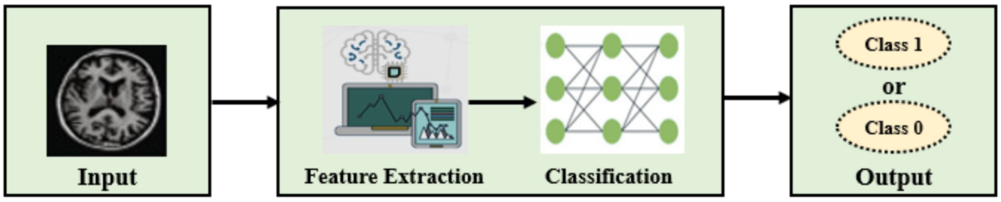

Figure 2.4: General workflow diagram of machine learning algorithms

Machine Learning is divided into three categories: Supervised Learning, Unsupervised

Learning, Semi-supervised learning, and Reinforcement Learning.

1. Supervised Learning

In this type of learning, data experts feed labeled training data to algorithms and define variables for algorithms to access and find correlations. The algorithm has defined input and output [31]. Supervised learning is commonly used in the context of Classification and Regression.

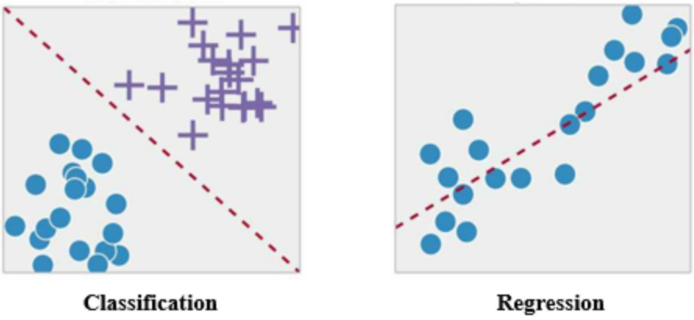

Figure 2.5: Classification vs. Regression

2. Unsupervised Learning

Unsupervised learning is the use of artificial intelligence algorithms to identify patterns in data sets that contain no classified or labeled data points. As a result, the algorithms can classify, label, and/or group the data points contained within the data sets without any external guidance [32].

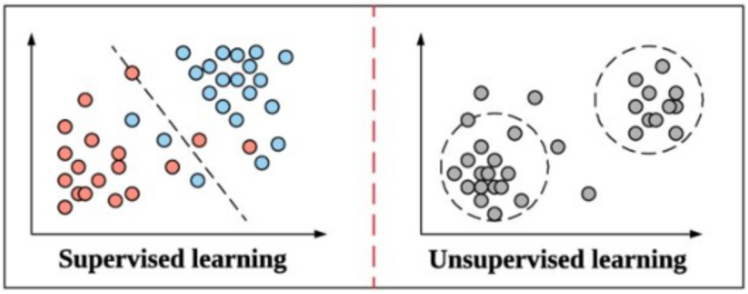

Figure 2.6: Traditional Machine Learning. Examples of Supervised Learning (Linear Regression) and Unsupervised Learning (Clustering).

3. Semi-Supervised

Semi-supervised learning can be defined as a hybrid of the above supervised and unsupervised methods as it works with both labeled and unlabeled data [33]. So it falls between "unsupervised" learning and "supervised" learning. In the real world, labeled data can be sparse in multiple contexts, and unlabeled data is plentiful where semi-supervised learning is useful [34]. The ultimate goal of a semi-supervised learning model is to provide a better prediction result than one obtained from the model using only labeled data.

4. Reinforcement Learning

Used to train a computer program to complete a multi-step procedure with well-defined rules. An algorithm is created by programmers to carry out a task, and it is given a positive and negative signal to act when the algorithm executes to carry out the work [35]. In other cases, the algorithm even chooses for itself what to do next.

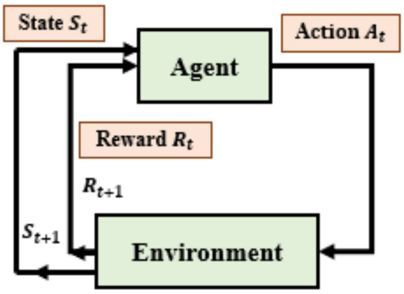

Figure 2.7: Reinforcement Learning Model.

Deep Learning

Deep Learning (DL) is a subset of (ML) that can solve more complex problems. It is the learning process in which the machine processes and analyzes the input data using a variety of approaches until it finds the single desired output. It is sometimes referred to as machine self-learning [36].

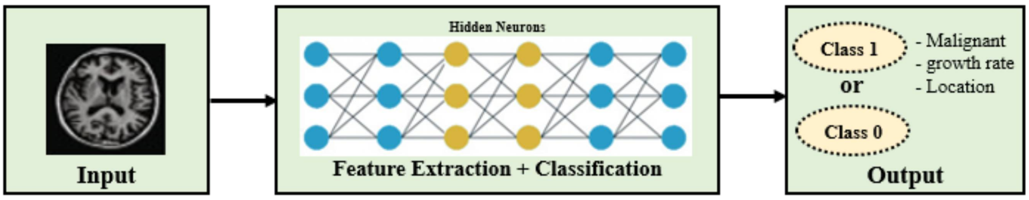

Figure 2.8: General workflow diagram of Deep learning algorithms.

2.3.3 Computer Aided Diagnosis (CAD)

Several factors including fatigue, lack of experience in medical imaging and the number of images to be analyzed each day make radiologists' diagnoses tedious and, as a result, prone to errors with potentially fatal consequences for the patients. Computer-Aided Diagnosis (CAD) for disease detection has been introduced to improve and assist experts and other clinicians in cancer prevention, this diagnosis is performed by a radiologist using the output of a computerized scheme for automated image analysis as a diagnostic aid [37], the performance of computers does not have to be comparable or superior to that of doctors but must be complementary to that of doctors, it is considered as a synergy and a second opinion.
The construction of a CAD (see Figure 2.10) is mainly based on four essential steps: image preprocessing, segmentation, Feature extraction, and classification.

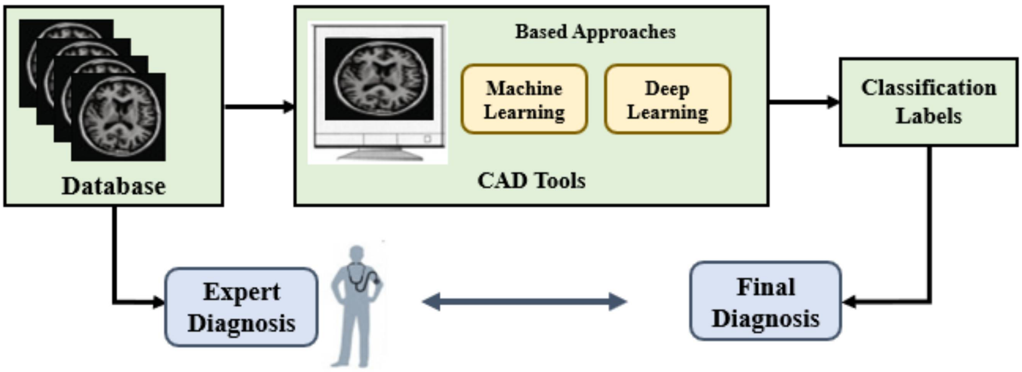

Figure 2.9: Computer-aided Diagnosis for disease detection diagram.

- The patient visits the doctor with a complaint.
- If necessary, the doctor refers the patient to specific imaging to diagnose the problem.
- The acquired images are analyzed by experts to establish a diagnosis.
- The diagnostic report is used by the doctor to plan treatment.

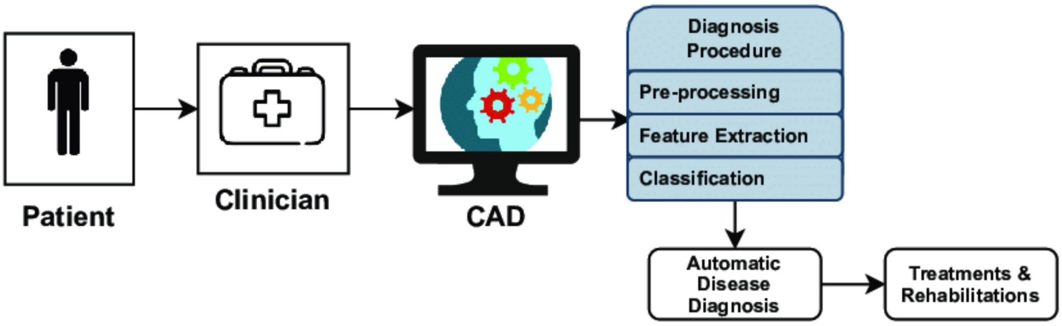

Figure 2.10: Computer-Aided Diagnosis System Architecture.

Computer Aided Diagnosis (CADx) (usually focused on classifying detected structures or regions) and Computer Aided Detection (CADe) (usually confined to marking suspicious structures and sections) are medical decision support systems used in the process of medical diagnosis, it provides access to medical Database information and can suggest differential diagnoses based on pre-populated data after clinical examination, prognostic estimates, or flag missing information to determine the correct diagnosis.
Computer-Aided Diagnostic (CAD) systems use artificial intelligence to analyze lesion data and diagnose skin cancer. When used in the primary care setting, they can assist doctors or other physicians in better triaging high-risk lesions and referring them to secondary care. For example, when combined in conjunction with a suspicion of malignancy on clinical and dermoscopic examination, they can reduce the number of unnecessary excisions without leaving melanomas undetected [38].
A Computer-Aided automatic Diagnostic (CAD) system designed on a model that takes into account the relevant pathology descriptors will always be robust, which could help radiologists reduce the number of unnecessary biopsies and avoid unnecessary patient stress, especially in cases of a cancer diagnosis. The CAD system used in a screening or diagnostic context will therefore serve as a second opinion for the radiologist and is not intended to replace the latter. Studies show that screening tests for certain types of cancer can save lives by detecting cancer early. Screening tests for other types of cancer are only advised for those who are at high risk.
Many medical organizations and patient advocacy groups issue cancer screening recommendations and guidelines. The various guidelines can be discussed with the doctor, and the best one can be chosen based on the patient's cancer risk factors. Even if the lesion appears to be suspicious on a medical image or ultrasound, preoperative

diagnosis is now required for two reasons:

- If it is not cancer, it can prevent many unnecessary surgeries.
- When it comes to surgery it assists doctors in optimizing it from the start.

2.4 CAD Design

In general, the operation of the CAD system consists of several equally important steps. When the system receives an input image, the following steps must be taken in this Section to design the diagnostic support system during the Machine and Deep Learning phases (see Figure 2.11):

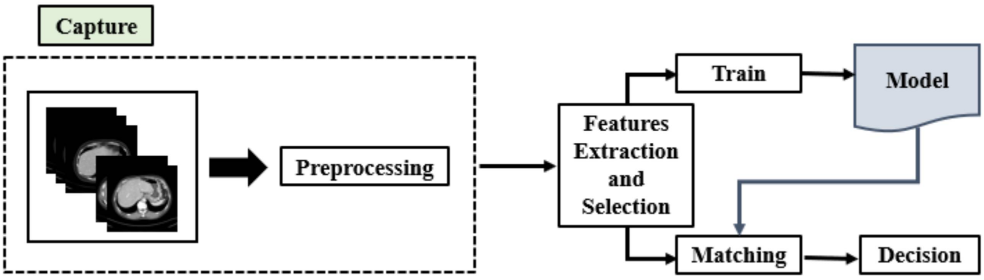

Figure 2.11: Computer-Aided Diagnosis System Design.

2.4.1 Model Building (Train Phase)

During the learning phase, the classifier is built by learning from the labeled dataset. When training a model, engineers choose and collect a large and representative sample of data.

A corpus of text, a collection of images, sensor data, and data collected from specific service users are just a few examples of the data that can be included in the training set.

Data Preprocessing

Whether they are used for medicinal purposes or not, the images that are taken are frequently corrupted by sensors and light noise. Each image analysis is required to

Figure 2.12: Train Phase Model.

include a pretreatment step that entails all of the processing operations intended to enhance the quality of the acquired image. The CAD system removes obvious noise or specks and improves image contrast to achieve the best image quality through denoising, edge enhancement, and other features.

The purpose of the preprocessing step is to facilitate the segmentation by reinforcing the similarity between the pixels belonging to the same region or by highlighting the dissimilarity between pixels belonging to different regions [39].

The purpose of applying image enhancement technology is to: eliminate image defects (errors in images), reduce image noise (image noise - random color differences scattered in an image), flatten (format) image quality to remove different ground states of the image such as different exposure variables, Distinguish between different structures of the image, such as the heart, lungs, rib cage, and annular flares, Correspondence to anatomical data.

1. Contrast

Contrast indicates how black can be distinguished from white at a given resolution. For the image to appear well-defined, black parts must appear black and white parts white (see Figure 2.13) [40]. The more black and white information is oriented towards the intermediate grays, the lower the contrast at this frequency.

The greater the difference in intensity between the light and dark lines, the greater the contrast. While this may seem obvious, it is of the utmost importance. The contrast at a given frequency can be calculated from equation (2.1), where: I_{max} is the maximum intensity (usually in pixel grayscale values, if a camera is used), and I_{min} is the minimum intensity.

$$Contrast = \frac{I_{max} - I_{min}}{I_{max} + I_{min}} \tag{2.1}$$

In medical diagnostics, MRI is performed with a contrast agent for better resolution of the examination, rather than with additional procedures to clarify problems in the case of non-contrast imaging (see Figure 2.14).

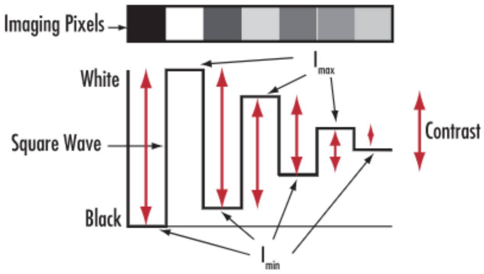

Figure 2.13: The transition from black to white corresponds to high contrast, while intermediate grays indicate lower contrast.

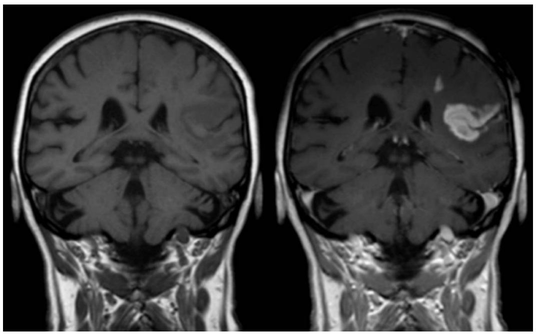

Figure 2.14: MRI of the brain with and without Contrast. Both images suggest an arachnoid cyst: The left image (without Contrast) showed a left frontal hypointense extra-axial lesion. The image on the right (with contrast) showed a left frontal hyperintense extra-axial lesion

2. Histogram Equalization

To improve the characteristics of the image (to enhance contrasts), a common approach is to use a function that assigns a new value to each intensity value of the image, this function modifies the histogram of the image. Its principle is to subject each pixel and its context region to a Histogram Equalization. This region actually represents the neighboring pixels surrounding the pixel being processed (see Figure 2.16) [41]

The probability of occurrence of the intensity level r_j is [42]:

$$P_n(r_j) = \frac{n_i}{n} \qquad 0 \leq i < L \tag{2.2}$$

where:

n_i denote the number of pixels with intensity r_j n denotes the total number of pixels in the image.

L the total number of gray levels in the image (typically 256).

The transformation function used here is :

$$s_k = T(r_k) = (L-1)\sum_{j=0}^{k} P_r r_j \tag{2.3}$$

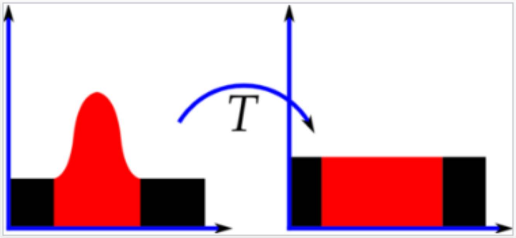

Figure 2.15: Histograms of an image before and after equalization.

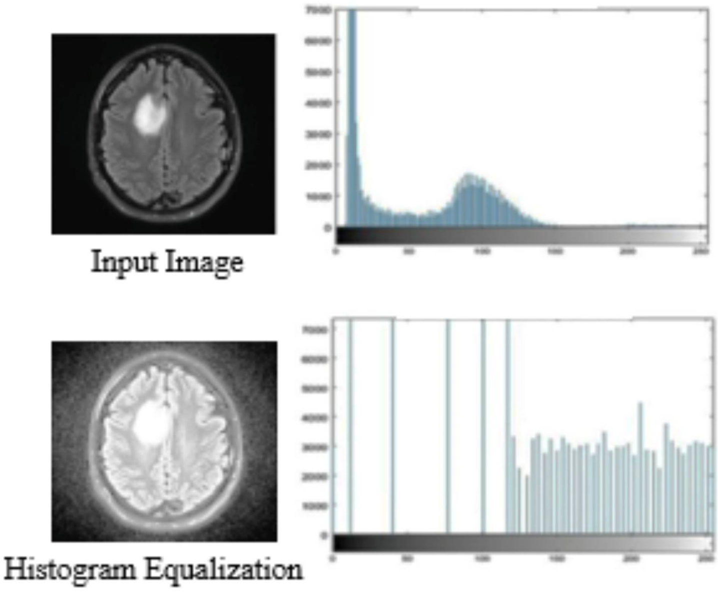

Figure 2.16: Histogram Equalization for a brain tumor [43].

3. Normalization

Normalization is a data preprocessing technique that reduces the complexity of models. It is also a requirement for implementing certain algorithms. This technique re-scales features with a distribution value between 0 and 1. For each feature, the minimum value of that feature gets transformed into 0, and the maximum value gets transformed into 1 (see Figure 2.17).

Normalization standardizes the mean and the standard deviation of any type of data distribution and allows the learning problem to be simplified by avoiding these two parameters.

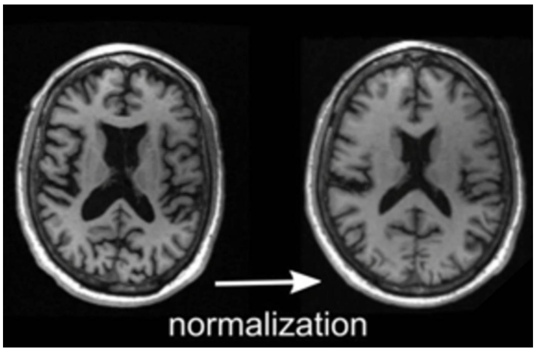

Figure 2.17: Applying the image Normalization process for an MRI brain [44].

The general equation is shown below:

$$x_{norm} = \frac{x - min(x)}{max(x) - min(x)} \tag{2.4}$$

4. Standardization

The result of standardization (or Z-score normalization) is that the features are rescaled to ensure the mean and the standard deviation are 0 and 1, respectively. The equation is shown below:

$$x_{stand} = \frac{x - mean(x)}{standarddeviation} \tag{2.5}$$

This method of rescaling feature values with a distribution value between 0 and 1 is useful for optimization algorithms, such as gradient descent, which is used in machine learning algorithms that weigh inputs (e.g., regression and neural networks).

5. Region Of Interest Detection

Segmentation means the division of an image into homogeneous regions according to a determined criterion: color, texture, gray level, etc. In this step, the image is partitioned to select the Region of Interest (ROI), and each region is analyzed separately

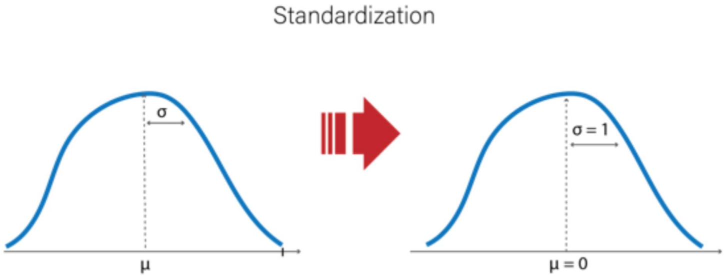

Figure 2.18: The concept of standardization.

to reveal certain distinguishing features: compactness, shape, size, and location of the region, an indication of nearby structures (region of interest), the average value of the analysis of the gray levels in the ROI, the ratio of the gray levels to the boundaries of the structure in the ROI.

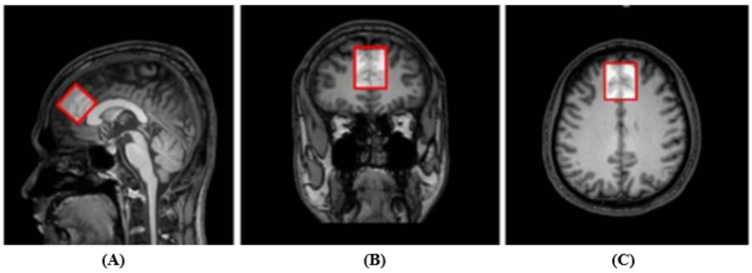

Figure 2.19: Position of MRS region of interest. A region of interest (ROI) with a size of 30 × 30 × 30 mm 3 was created over the anterior cingulate cortex according to a high-resolution anatomic 3D T1WI MRI scan. The ROI is shown in (a) sagittal, (b) coronal, and (c) transversal orientations [45].

Feature Extraction

Feature extraction is a component of image processing that often involves classification. Indeed, in general, setting a classification rule (supervised or not), relies on a set of numerical criteria for an observed object or phenomenon. In practice, we aim to extract relevant information that characterizes each category, depending on the context. If anomalies are detected anomaly, several mathematical attributes are extracted which to help better describe the nature of the lesion, two types of features can be extracted:

- Generic descriptors that do not necessarily have a physical or biological interpretation: (SIFT, SURF, oriented gradient histograms, shape context, word of bags).

- Descriptors have a physical meaning. In the biomedical field, it is usually the morphological features (cell size, blood vessel thickness, etc.) that describe what is being observed.

Training

The training test remains the most characteristic phase of the machine. Given the data, the model is trained over time to gradually improve its ability to react to a given situation, solve a complex problem, or perform a task. For this learning phase, the training data (also known as the “training set”) should be used. All the information collected often becomes too heavy and resource-intensive:

- Then just select part of the data set (sampling) to train the model more efficiently and improve its predictions.
- A representative sample of data should be selected without the risk of bias.
- Request data transformation instructions.
- Training setting to control the learning algorithm. content...

2.4.2 Classification Phase

The extracted descriptors are classified according to algorithms adapted to this task, segmented objects are assigned to specific classes to determine the type of mass, and class identification is based on selected features. After structural analysis, an area-by-area assessment (recording) is performed to determine the likelihood of a true positive.

A. Most tasks of Classification

1. Binary Classification: It is a type of classification with two outcomes, true or false.
2. Multi-Class Classification: The classification with more than two classes, in multi-class classification each sample is assigned to one and only one label or target.

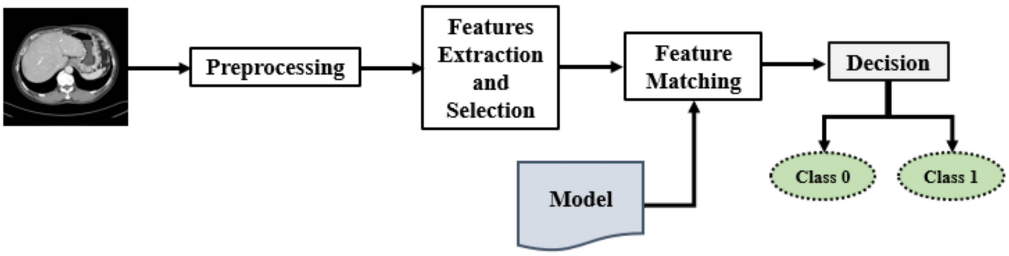

Figure 2.20: Classification Phase Model.

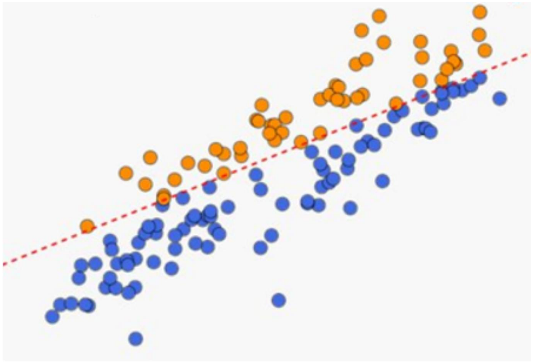

Figure 2.21: Binary Classification task [46].

3. Multi-Label Classification: This is a type of classification where each sample is assigned to a set of labels or targets.

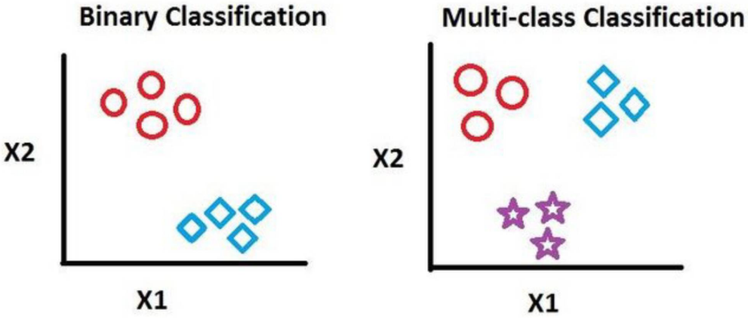

Figure 2.22: Binary vs Multiclass classification [47].

4. Imbalanced Classification: This is a classification dataset with skewed class ratios. Classes that occupy a large part of the data set are called majority classes. Those who represent a smaller percentage are the minority classes.

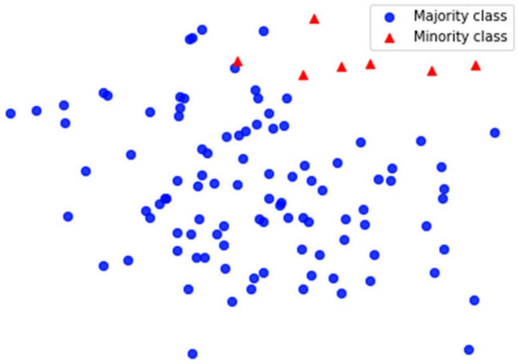

Figure 2.23: Class imbalance distribution [48].

B. Classification Algorithms

The study of classification in statistics is broad and there are different types of classification algorithms that you can use depending on the data set. Below are some of the most popular classification algorithms.

- k-Nearest Neighbors
- Logistic Regression
- Decision tree
- Random forest
- Support Vector Machine
- Naive Bayes
- Stochastic Gradient Descent
- Artificial Neural Networks

2.5 Field of application

A primary use of CAD systems is to find abnormalities in the human body. Among these, tumor detection is a typical application as listed below.

1. Breast Cancer

Breast cancer is a malignant tumor that develops in the breast. As in all cancers, the initially local tumor can then spread to neighboring tissues(see Figure 2.24).

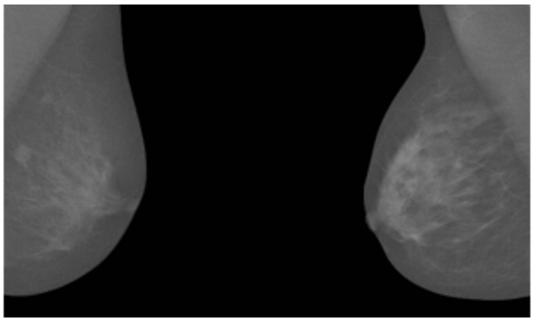

Figure 2.24: Mamogram example, On the Right Normal Mammogram and the left Abnormal Mammogram [49].

2. Lung Cancer

Lung cancer starts in the cells of the lung. A cancerous (malignant) tumor is a group of cancerous cells that can invade nearby tissues and destroy them. The tumor can also spread (metastasize) to other parts of the body(see Figure 2.25).

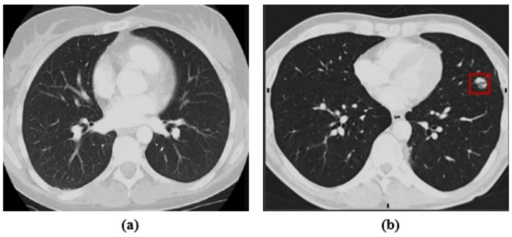

Figure 2.25: MRI Scan of chest showing cancer in (b), and a normal chest in the left.

3. Colon Cancer

Colorectal cancers start in the mucous membrane that lines the inside of the colon or rectum. In the majority of cases, it is an adenocarcinoma resulting from the malignant transformation of an intestinal polyp(see Figure 2.26).

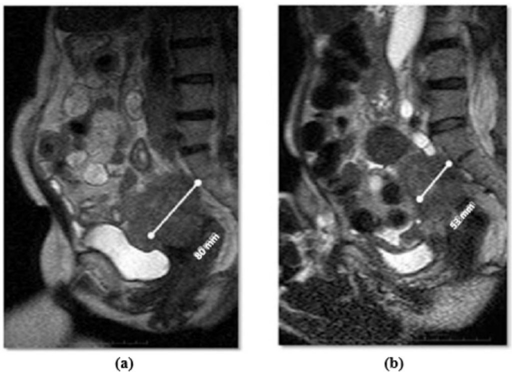

Figure 2.26: local recurrence of sigmoid colon cancer in the pelvis. (a) This MRI scan shows a local recurrence of sigmoid colon cancer in the pelvis before treatment. The tumor was 80 mm in size. (b) After 1 course of treatment, the tumor decreased in size to 53 mm [50].

4. Diabetic retinopathy

Diabetic retinopathy (eye damage: eye and retina) is a serious complication of diabetes that affects 50% of type 2 diabetic patients. The eyes are particularly sensitive to damage to small vessels(see Figure 2.27).

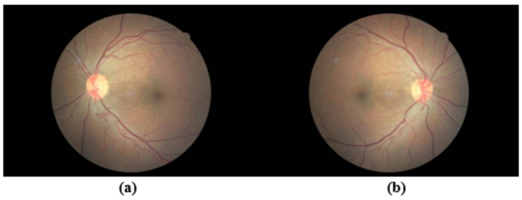

Figure 2.27: Example of Diabetic Retinopathy normal patient on the left, and patient sick on the right.

5. Alzheimer's disease

Is a neurodegenerative disease (i.e. progressive brain damage leading to neuronal death) characterized by progressive loss of memory and certain intellectual functions leading to repercussions in the activities of daily living(see Figure 2.28).

5. Liver Cancer

Liver cancer starts in liver cells. A cancerous (malignant) tumor is a group of cancerous cells that can invade nearby tissues and destroy them. The tumor can also spread to other parts of the body (metastasize)(see Figure 2.29)

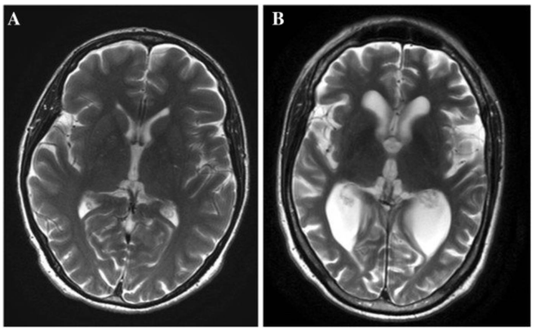

Figure 2.28: Brain MRI. Axial T2 images show cerebral atrophy in a patient with Alzheimer's disease (A) and a normal brain in a control patient of the same age (B) [51].

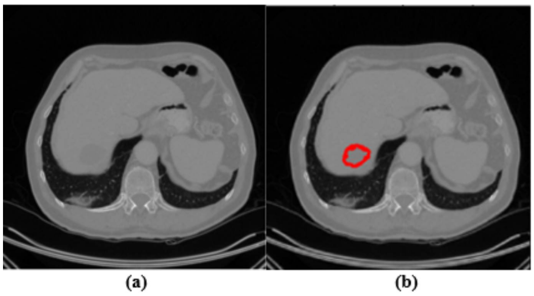

Figure 2.29: Computed tomography (CT) images of liver tumors in (b), and normal liver in (a).

6. Fracture

Bones are part of the musculoskeletal system, which also includes muscles and the tissues that attach them (ligaments, tendons, and other connective tissues, so-called soft tissues).

Figure 2.30: Radiograph of the same patient of a 26-year-old male who has fractured both bone legs.

These structures give the body its shape, stabilize it and allow it to move. We speak of a fracture when a bone is cracked or broken.

2.6 Conclusion

The term "Computer-Aided Diagnosis" (CAD) refers to a vast field of computerized methods that support radiologists in their clinical Decision-Making processes by integrating image processing, Machine Learning/Deep Learning, Computer Vision, Mathematics, Physics, and Statistics. These methods include cancer risk assessment, physiologic evaluation, volumetric analysis, Classification of Lesions, quantification of illness and anatomic structures (including disease progression and temporal response to therapy), and detection of disease and interesting anatomic structures. The creation of such methods necessitates expertise in the physics of picture acquisition, characteristic descriptor mathematics, software development, and rigorous statistical validation techniques.

Chapter 3

Bone Strength and Diagnosis of Osteoporosis

3.1 Introduction

Osteoporosis is a systemic skeletal disease characterized by reduced bone mass and architectural deterioration of bone tissue leading to increased bone fragility and increased risk of fracture. Its management is one of the priority public health missions. Indeed, this disease is responsible for many accidents and deaths. In addition, it generates significant health costs, because it is known that more than 30% of women reaching the age of 50 will present at least one osteoporotic fracture during their life [52]. These fractures usually occur in the hip, vertebrae or wrist and occur most often in men and women aged 65 and over. Although osteoporosis cannot yet be cured, there are treatments that can help reverse bone loss or prevent its progression. Thus, early diagnosis can help reduce the number of these osteoporotic fractures [53].

Initially, this chapter focuses on the structure of the bone, Osteoporosis and its challenges. In a second step, we expose the main techniques allowing the diagnosis of osteoporosis.

3.2 Bone Architecture

Bone is the main component of our skeletal system (see Figure 3.1), giving us size and shape, and performs several important functions including support, protection, movement, mineral storage, and, indirectly, the formation of blood cells in the red marrow.

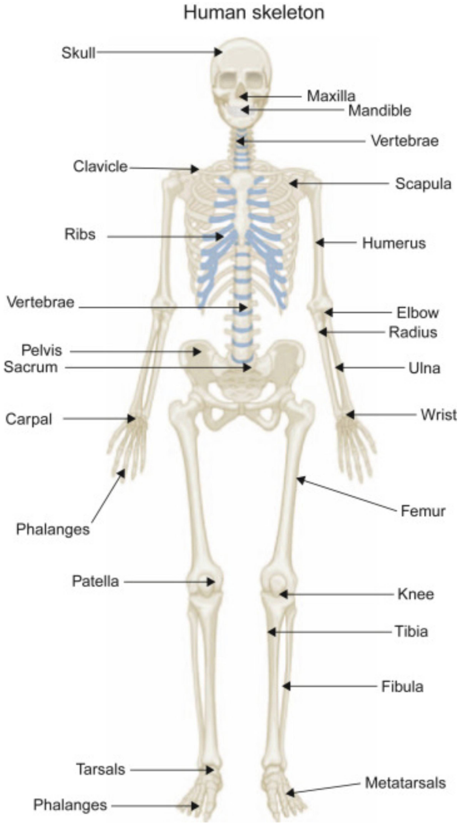

Figure 3.1: Gross structure of the human skeleton [54].

3.2.1 Bone and the skeletal system

Many bones made at birth fuse together as they grow, to form the skeleton of 206 bones in adulthood, these bones are distributed as follows (Table 3.1) [55].

3.2.2 Type of Bone

Five types of bones, taken from a human skeleton have varying shapes and sizes depending on their function and location in the body.

Table 3.1: Distribution of skeletal bone in the adult body

206	80 bones	Head axis (Fig 3.2)	14	the Face
			8	the Skull
		Neck axis (Fig 3.3)	24	Movable vertebrae (Cervical/thoracic/ lumbar)
		Trunk axis (Fig 3.4)	9	Fused vertebrae (sacrum/coccyx)
			24	ribs
			1	Sternum
	126 bones			For members

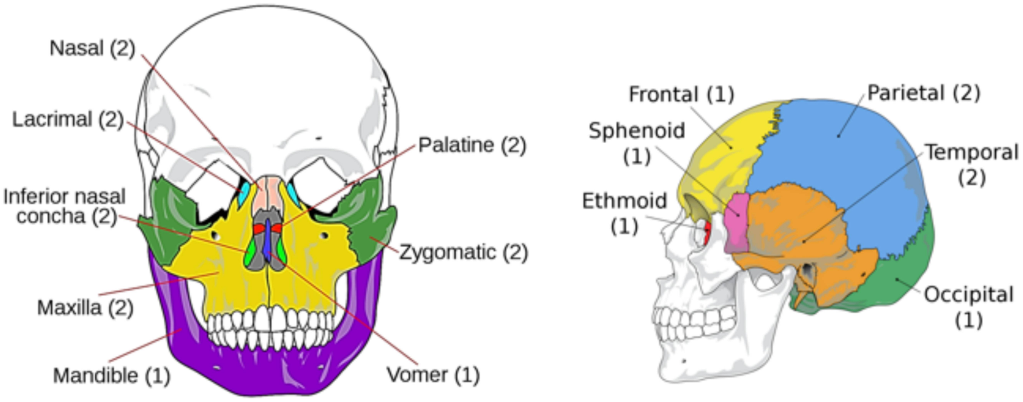

Figure 3.2: Schematic diagram illustrating the subunits of the facial skeleton on the left and the skull on the right [56].

1. **Long bones:** Support weight and promote movement, they are characterized by a shape much longer than wide such as the radius, the humerus, and the femur. Are composed of the body, or diaphysis, and the extremities, or epiphyses, where the trabecular (spongy) bone is found. Most of the limb bones are long despite varying sizes.

2. **Short bones:** Cubic in shape, such as the carpal bones, the tarsal bones, the phalanges of the hand and foot, and the calcaneus, which are smaller and have many articular surfaces.

3. **Flat bones:** Protect internal organs, such as the scapula, sternum, and skull bones, thin.

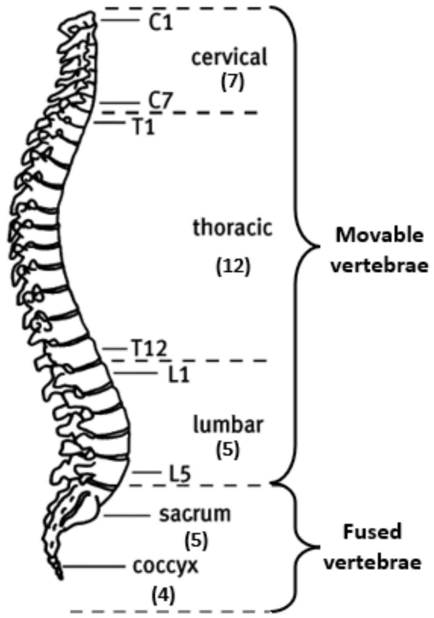

Figure 3.3: Diagram of Vertebral column showing different parts and regions of the spine [57].

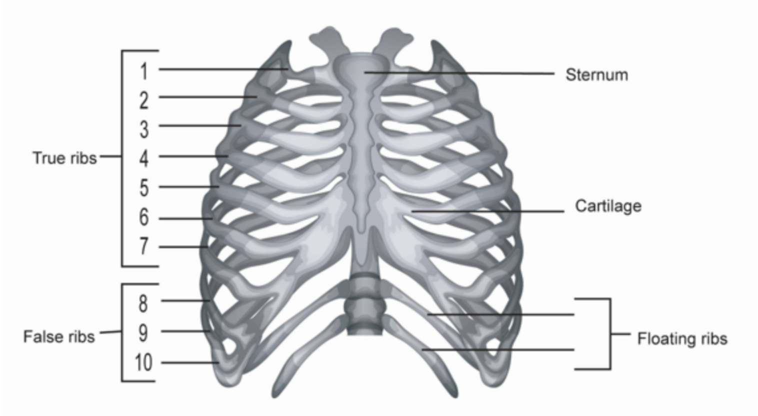

Figure 3.4: Human thoracic cage.

4. Irregular bones: Complex shapes, such as the vertebrae, cannot be classified into the preceding groups.

5. Sesamoid Bones: Strengthen Tendons, such as bones of the hand or the patella, small bones located in the thickness of the tendons.

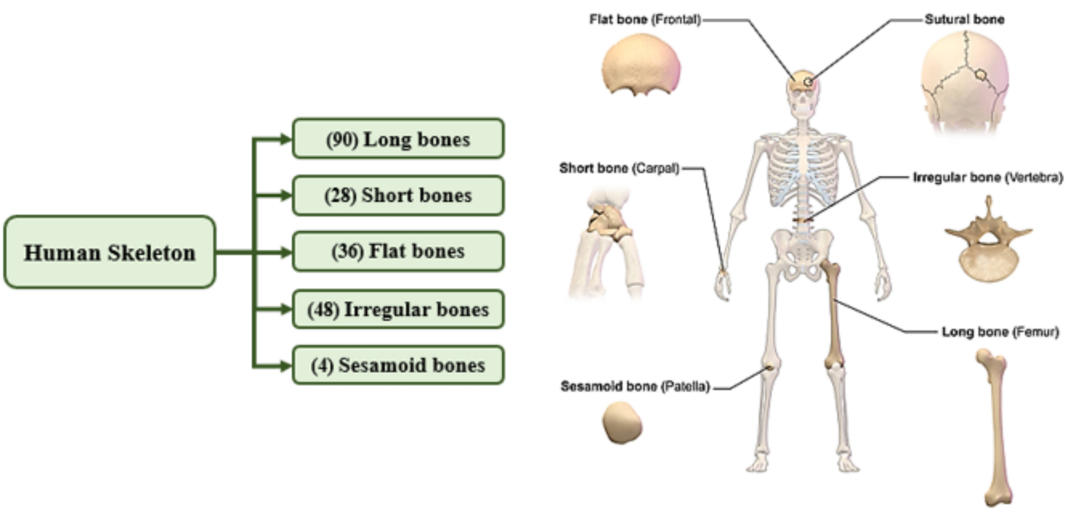

Figure 3.5: Classification of Bone by shape [58].

3.2.3 Bone Anatomy

1. Macroscopic Bone Structure

The diaphysis of a long bone is essentially made up of compact (cortical) bones (Figure 3.6). The center of this diaphysis is hollow and forms the medullary canal. In which the bone marrow is located. It is essentially a lipid tissue (Figure 3.7.(a)).

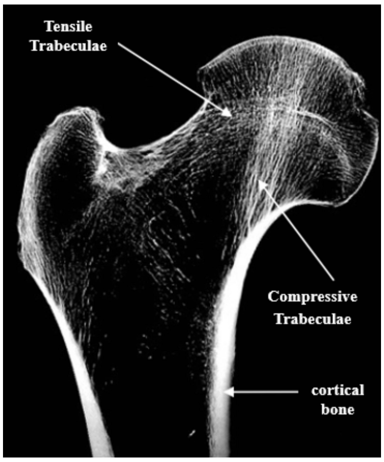

Figure 3.6: Diagram of the ‘compression’ and ‘tension’ trabecular columns in the femoral neck [59].

The outer surface of this diaphysis is covered with per bone which is anchored to the bone by collagen fibers also called skeletal fibers. The diaphysis is perforated by numerous canals, which are called: Volkman’s perforating canals; they allow vessels and nerve extensions to cross the diaphysis. These canals are lined with endosteum (pro-

tective membrane). The epiphyses of a long bone are composed at the periphery of a thin layer of compact bone and the center of the trabecular (spongy) bone.
On the surface, the peri bone covers the bone and gives rise to the articular cartilage, this cartilage will cover the articular surfaces (Figure 3.7.(b)), such as the diaphysis where there are perforating canals. The flat, irregular, and short bones have a simple structure, with a thin layer of compact bone on the periphery covered with the periosteum, and in the center, there is trabecular bone, the perforating canals covered with endosteum and the articular surfaces, hyaline cartilage.

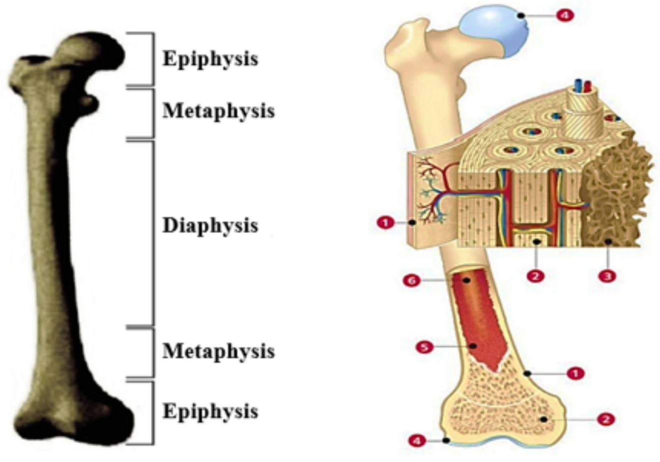

(a) (b)

Figure 3.7: Long bone. The external structure of a long bone (femur) is formed by a central shaft or diaphysis, and two extremities, or epiphyses, covered with articular cartilage. The metaphyses constitute the intermediate parts between epiphysis and diaphysis (a), Cross-sectional view of a bone showing the different types of tissue that make it up (b), (1) periosteum, (2) cortical bone, (3) cancellous or trabecular bone, (4) cartilage articular or hyaline, (5) bone marrow or red marrow and (6) yellow marrow [60].

2. Microscopic Bone Structure

At the microscopic level, the bone contains different types of tissue:

- **Bone Cortical:** Cortical bone is the strong and compact type of bone found on the outer layer of the long bones and makes up about 80% of the skeleton.
- **Bone Trabecular:** The spongy-looking porous interior part of the bones (mainly vertebra and at the end of long bones) is called trabecular or cancellous bone.

It has a greater surface area than cortical bone and is more actively remodeled. The effects of therapeutic agents are seen earlier in trabecular bone than in the cortical bone.

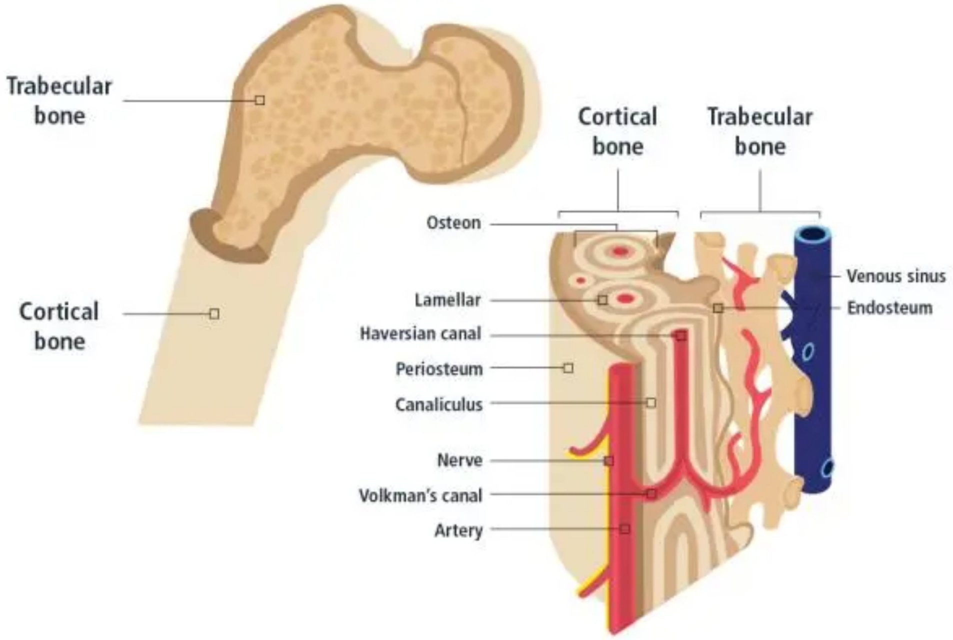

Figure 3.8: Microscopic structure of Cortical and Trabecular bone [60].

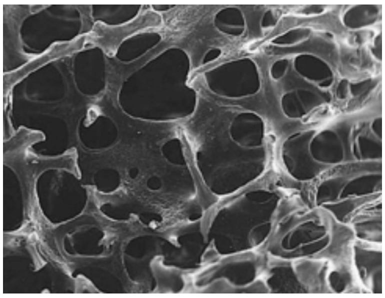

Figure 3.9: Example of a photomicrograph that shows the porosity of human trabecular bone.

The femoral neck is made up of both cortical and trabecular bone. The vertebrae are largely composed of trabecular bone as is the lower end of the radius and ulna (bones in the forearm fractured with Colle's fractures)[61].

Periosteum and Endosteum: Periosteum and Endosteum are two membranes that cover the lining of bones, both are made up of connective tissue. Also, both contain cells including fibroblasts, osteoblasts, and osteoprogenitor cells. Besides, both structures play a key role in bone remodeling.

3. Chemical Composition of Bone

Bone is made up of two phases, Organic and Mineral. The Organic matrix which accounts for about 35% of the total dry weight of bone, which includes specific Proteins, Osteoclasts, Osteoblasts and Osteoids . The inorganic (Mineral) components, which account for about 45% of the total dry weight of bone, consist mainly of Mineral Salts, or Hydroxyapatites which are essentially Calcium Phosphate. Remaining 20% being essentially water(Table 3.2) [62].

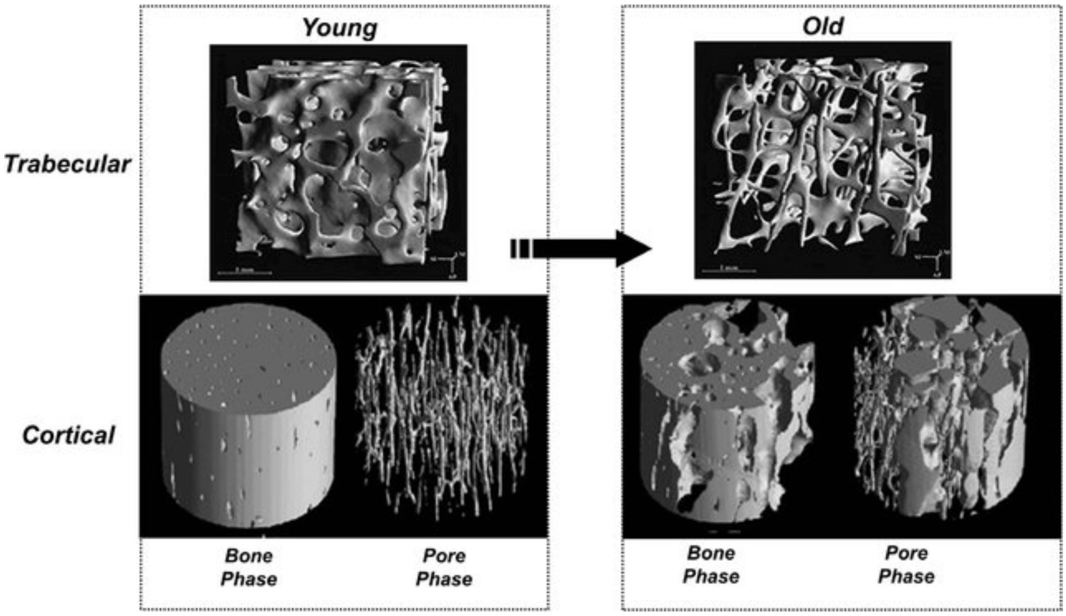

Figure 3.10: The effect of aging and osteoporosis on bone loss. On the left side, the trabecular and cortical bone images of a young adult, and on the right side, the corresponding images of an old adult are indicated. Porosity increases with advancing age and this process is further accelerated in osteoporosis. This effect is compounded with a loss in mechanical competence [60].

Table 3.2: Chemical Composition of Bone

Organic 35%	Protein		Mineral 65%	mineral salts	Hydroxyapatite
	Osteoblasts/Osteoclasts				Calcium Carbonate
	Osteoid	Proteoglycans			Magnesium Hydroxide
		Glycoproteins			Fluoride/Sulfate.
		Collagen Fibers		Water	

3.2.4 Bone Remodeling

1. Bone remodeling (fracture healing)

Life long process where old bone is removed (bone resorption) and new bone is added (bone formation). This occurs in fracture healing as well over a shorter time.

2. Bone Resorption

Begins when Osteoclasts remove a portion of the bone to be replaced later by the action of Osteoblasts. This is a vital step for signaling bone formation.

3. Bone Formation

Osteoblasts lay down collagen and mineral deposits over the area previously remodeled by Ostoclastes. Osteoclast activity is vital for maintaining bone mineral density and bone strength.

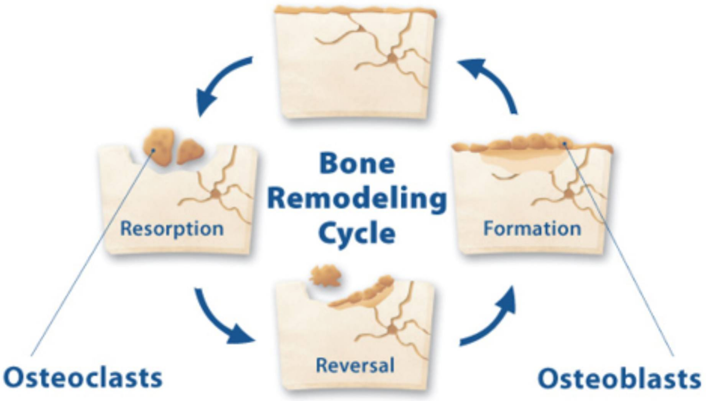

Figure 3.11: Bone renewal via the cycle of bone remodeling.

3.3 Osteoporosis

Osteoporosis and osteoporotic fractures constitute, at present, a considerable public health problem both in terms of disabilities and repercussions on the patients quality life and the resulting mortality. Osteoporosis is defined as a diffuse skeletal disease characterized by low bone mass and micro-architectural alterations of bone tissue, leading to increased bone fragility and risk of fracture [63]. This definition was modified in 2001 by the World Health Organization (WHO), which defines osteoporosis as a generalized disease of the skeleton characterized by a decrease in bone strength predisposing the individual to an increased risk of fractures [64]. Bone strength is determined on the one hand by the quantity of bone material, measured by Bone Mineral Density (BMD), and on other hand by the quality of the bone tissue, which depends on the microarchitecture, remodeling, accumulation of fatigue damage (such as microfractures) and degree of mineralization [64]. These definitions remove the ambiguity of the diagnosis of this disease long defined by its complication: the fracture, and underline the importance of taking into account bone resistance.

Osteoporosis is usually painless until a fracture occurs. An osteoporotic fracture also called a fragility fracture, is defined as a fracture caused by minor trauma (insufficient to fracture normal bone) such as a fall from a standing or sitting position, or occurring spontaneously [65]. These fractures usually occur in the hip, vertebrae, or wrist and occur most often in men and women over the age of 65 [65]. According to the WHO, in Europe, the United States, and Japan it can be assumed that 75 million people suffer from osteoporosis. This disease can now be treated effectively thanks to new therapeutic approaches provided it is detected early.

Osteoporosis has become a major public health problem due to the morbidity and mortality associated with osteoporotic fractures, particularly in the hip and vertebrae. In a British study, mortality at 12 months after a hip fracture was 33% [66]. From the age of 50, the risk of having an osteoporotic fracture of the hip, forearm, or spine is estimated at 30% - 40% for a white woman. In comparison, the percentages of breast cancer or cardiovascular disease are 9% - 12% and 30% - 40% respectively. These figures show the interest in preventing these fractures by favoring an early diagnosis of the disease to prescribe a treatment.

According to WHO experts, osteoporosis can be defined from a densitometric result, the T-score (see Table 3.3) [67]

T-Score: Difference in standard deviations, between the measured Bone Density and the theoretical Bone Density of young adults of the same sex, at the same bony site, and of the same ethnic origin.

Table 3.3: Criteria defined by the WHO for the classification of patients by Bone Mineral Density (BMD) measured by Biphoton X-ray Absorptiometry.

Classification	**T-Score**
Normal Bone Density	T-Score> -1
Low Bone Density (Osteopenia)	-1 > T-Score> -2.5
Osteoporosis	T-Score ≤ -2.5
Severe Osteoporosis	T-Score ≤ -2.5+1 or more fractures

3.4 Methods Dedicated to the evaluation of bone strenght

Bone mineral content is commonly assessed in clinical routine in a precise and reproducible way by a densitometry examination and, thus, makes it possible to assess the risk of osteoporosis. Several methods make it possible to measure bone mineral density (BMD) in many sites such as the radius, calcaneus, vertebra, hip, and even the whole body without risk and with precision. The measurement of the quantity of bone in vivo is the technique that is currently the clinical reference for the evaluation of the risk of fracture and the assessment of risk factors.

The main methods studied or used to investigate bone density are Dual-Energy X-ray Absorptiometry (DEXA) , Quantitative Computed Tomography (QCT), ultrasound, and nuclear magnetic resonance relaxometry [68].

Studies show that x-ray images, Computed Tomography (CT) images, and Magnetic Resonance Image (MRI) contain textural information that relates to trabecular density and network connectivity, Trabecular Bone. In this part, we will present the different methods for assessing bone microarchitecture as well as the advantages and limitations of each of them.

3.4.1 Dual photon X-ray absorptiometry (DEXA)

The measurement of Bone Mineral Density (BMD) by two-photon X-ray absorptiometry is currently the reference technique for measuring bone density. This technique is the most accurate way to obtain a surface mass commonly called bone mineral density (BMD) in (g/cm^2), needed in the screening or diagnosis of Osteopenia or Osteoporosis (Figure 3.12).

DEXA is also used to predict a person's fracture risk and may also be useful in monitoring response to treatment. This test is quick and painless and involves minimal radiation. During DEXA examination, X-Rays are used to examine Bone Density in the lower spine, hip, wrist, or entire body. Bone Density measurements are very accurate at these sites.

Absorptiometric techniques are based on the quantification of the attenuation of an X-ray beam passing through bone sites resulting from their interactions with matter. During its crossing, the X-ray beam interacts with the bone tissue, the bone marrow as well as the peri-osseous tissues, often called soft tissues. Each of its tissues has different physical characteristics. This attenuation is governed by the Beer-Lambert law given by the following equation [69]:

$$I = I_0 e^{(\frac{\mu}{\rho})m} \tag{3.1}$$

I_0: Intensity of the incident beam.

I: Intensity of the transmitted beam.

m: Mass of the medium traversed by an X beam with a section of 1 cm^2.

μ: Mass attenuation coefficient

ρ: density of the medium

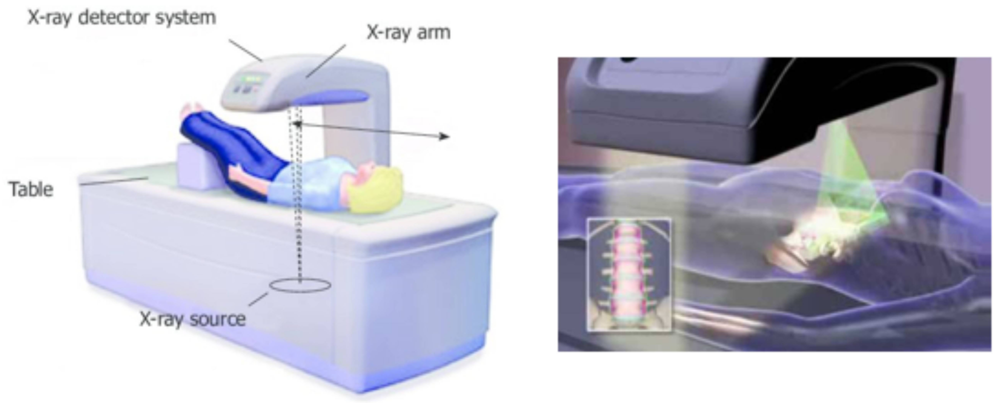

Figure 3.12: Bone densitometry Scan (dual X-ray absorptiometry). Schematic representation of X-rays source and detector system in dual X-ray absorptiometry device, in the left. And a Dual Energy X-ray Absorptiometry example, in the right.

The projection image obtained corresponds to an integration over the entire thickness of the zone to be analyzed (Figure 3.13). The contrast in the image is given by the attenuation of the beam which is much more sensitive in bone tissue than in soft tissue: the more the material attenuates X-rays, the more the corresponding pixel will be characterized by a strong signal. Bone tissue, therefore, appears white in the image. This technique makes it possible to determine the surface BMD, expressed in g/ cm^2.

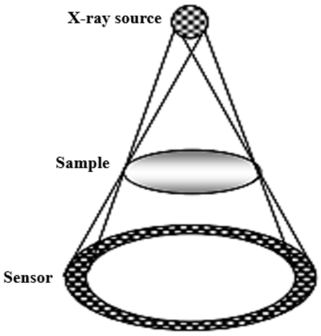

Figure 3.13: Principle of X-ray absorptiometry.

An example of an image obtained from the two images acquired at two different energies is shown in (Figure 3.14).

Generally, the measurement of the BMD is carried out at the level of the hip and the spine (vertebrae L2 to L4, see Figure 3.14), one can also operate at the level of the forearm at the proximal site (cortical component) or distal (trabecular component). Depending on the devices and the site analyzed, BMD measurement is more or less rapid (5 to 15 minutes) and reproducible (from 1 to 2%), this precision is represented by the standard deviation calculated from a certain number of successive measurements carried out with the same device. In terms of irradiation, DEXA ranks among the least irradiating methods, it varies from one device to another and according to the measurement site. The effective dose is between 0.5 and 4 millisieverts (mSv).

Large population studies have established normality curves for bone mineral content and bone mineral density. Each device manufacturer must establish "normal" reference values corresponding to the site analyzed (femoral neck, vertebrae, etc.), the age, sex, and ethnic characteristics of the subject.

The diagnosis is based on the Z-Score and especially the T-Score tool:

Z-Score: is the measure of the difference between the measurement of bone mineral density (BMD) corresponding to the patient m_p and the mean value m_R reported to

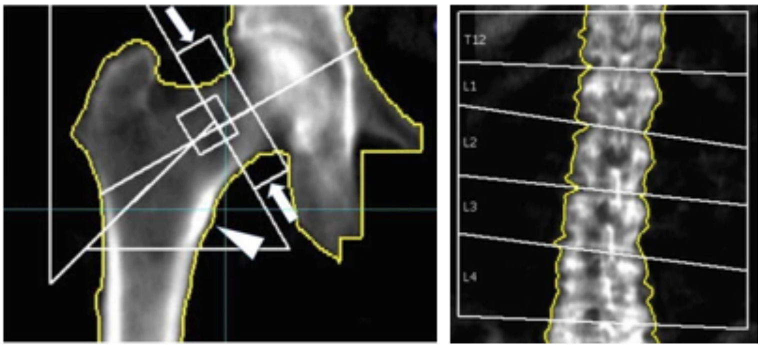

Figure 3.14: (Right): Spine Bone Density, initial DXA for pretreatment assessment of a 72-year-old woman, The scan includes the inferior portion of T12 and the superior portion of L5. The DXA image shows the scanned regions from which the BMD measurement has been obtained. (Left): DXA of the hip. The hip is in internal rotation to obtain a more en-face projection of the femoral neck. With internal rotation, the lesser trochanter is small or invisible (white arrowhead). The markup of the ROI varies with the manufacturer. In this image, the total hip is indicated by the (yellow outline) of the bone margins, the superior margin of the femoral neck ROI, and the subtrochanteric (horizontal line). The (arrows) indicate the femoral neck ROI. The femoral neck ROI varies with the manufacturer but should not include the ilium or ischium (Color figure online) [70].

the standard deviation σ of the distribution of the reference population of the same age and same sex [71]:

$$Z - score = \frac{m_p - m_R}{\sigma} \tag{3.2}$$

The Z-Score is useful for assessing the risk of fracture in osteoporotic patients. A decrease of one unit would mean that the risk of fracture would be doubled.

The T-Score differs from the Z-Score by the definition of the reference population. This is made up of young adults (20-30 years), of the same sex and the same ethnicity, with maximum bone mass. This index, therefore, assesses the decrease in bone mass.

- **pDEXA (Peripheral DEXA)**

Small portable scanners are applied to peripheral sites, usually the radius and calcaneus.

Advantage: being portable and gives measurements of bone mineral density (BMD) comparable to measurements obtained by central densitometers.

Bone Mineral Density testing by DEXA is the only clinically accepted technique for diagnosing osteoporosis. BMD alone is not sufficient to predict individual fracture risk only provides a projection of the distribution of average global bone mineral density and does not allow the separation of cortical bone from spongy bone [72].

Main Parameters Characterizing the trabecular microarchitecture : The reference method for evaluating the microarchitecture of trabecular bone is histomorphometry. It consists of performing a biopsy of bone tissue in the iliac wing, cutting samples approximately 8 μm thick, and observing these cuts under high magnification microscopy.
The parameters most often calculated are:
Bone Volume (BV/TV): for Bone volume / Tissue Volume (in %)
Number of Spans (Tb. N): for Trabecular Number (in mm^{-1})
Span Thickness (Tb. Th): for Trabecular Thickness (in μm)
Span Spacing (Tb. Sp): for Trabecular Separation (in μm)

The connectivity indices of the trabecular bone network: The Number of Nodes, Terminals, Free ends, Ends connected, and, Free segments.
This examination involves risks inherent in its invasive nature and cannot be performed in clinical routine.

3.4.2 Quantitative Computed Tomography (QCT)

Is based on the same physical principles as absorptiometry, where an X-ray source is used to describe a rotation around the patient (scanner-type tomograph see Figure 3.15). For each position of the beam, the attenuation of the radiation is measured according to BeerLambert's law [73].

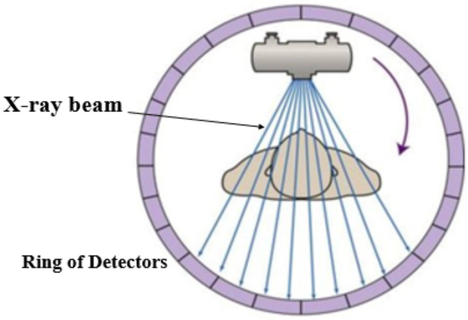

Figure 3.15: Block diagram of acquisition of tomographic by CT-scan.

This technique is the only one that can directly obtain a 3D measurement of Bone Mineral Density (BMD) expressed in g/cm3. The technique consists in assigning to each of the pixels of the 2D sections acquired by the X-ray scanner, a value on a grayscale, values of the linear attenuation coefficients μ_i (each pixel (i, j) corresponds to a value of $\mu_{i,j}$). Each μ is expressed in Hounsfield units, on a scale from -1000 to +1000 (2000 different values of μ). These attenuation coefficients are expressed in Hounsfield units (HU) from the water attenuation coefficient and are given by [65]:

$$C_{HU} = \frac{\mu - \mu_{water}}{\mu_{water}} \times 1000 \tag{3.3}$$

C_{HU}: the CT-scan number.
μ: linear attenuation coefficient
μ_{water}: water attenuation coefficient which depends on the intensity of the incident X-ray.

The CT-scan numbers characterize the linear attenuation coefficients of the tissue in each volume element compared to that of water (bone $>$ 1000 HU, fat $<$ -80 HU, air = -1000 HU).

The preferred site for this technique is the lumbar spine, and the measurement is mainly done on trabecular bone volumes of the vertebral body. However, one of the strengths of this technique lies in its ability to differentiate during the measurement, between the trabecular bone and the cortical bone. In addition, it provides information such as bone size and bone density distribution. Several clinical studies have shown the ability of QCT measurements to estimate vertebral fracture risk, with QCT even being considered the "gold standard" for this assessment. Nevertheless, this technique is not used in clinical routine due to a high radiation dose (7 to 10 mSv) and poorer reproducibility (5 to 15%) than that obtained by dual-photon absorptiometry [65].

- **pQCT (peripheral QCT)**

Intended for the evaluation of bone mass at peripheral sites such as the radius, tibia, and wrist. This technique has the advantage of having very good reproducibility. In addition, it makes it possible to have a real measurement of the trabecular volumetric density and thus to be able to differentiate the cortical bone component from that of spongy bone with a device much cheaper than a conventional CT scanner

[74].Nevertheless, the clinical impact of pQCT in the diagnosis of osteoporosis is rather small compared to DEXA or vertebral QCT, it offers fewer possibilities of measurement sites than the technique of densitometry (CT) and by dual-photon absorptiometry for an equivalent price.

3.4.3 Quantitative Ultrasound (QUS)

The majority of ultrasound imaging systems exploit the dual capacity of probes to emit and receive to work from information resulting from the reflection of the waves emitted. However, contrary to acquisition modes based on wave reflection at interfaces (used in echography and echocardiography), the mode used to characterize bone tissue is based on the transmission modifications that the signal (ultrasound wave) undergoes in passing through the bone structure. The reception of the signal is done at the other end of the structure studied by appropriate transducers (Figure 3.16). These modifications are a function of the density and certain mechanical properties of the material (elasticity, microarchitecture, the density of the material, etc.).

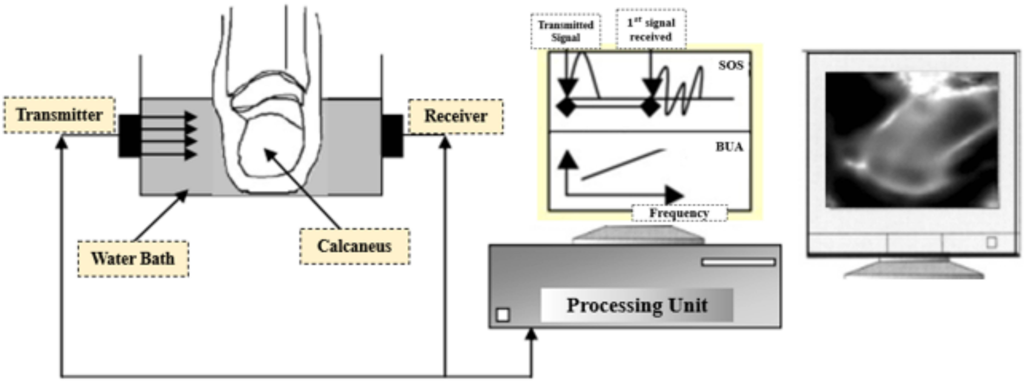

Figure 3.16: Block Diagram of an Ultrasound device used in vivo on a calcaneus [75].

In (Figure 3.16) the foot and the transducers are immersed in a water bath. Water is used to ensure proper coupling of the acoustic wave into the skin. Two parameters are mainly evaluated during the examination:

- **BUA (Broadband Ultrasound Attenuation)**

Consists in estimating the slope of the curve representing the attenuation in the medium as a function of the emission frequency and is expressed in [dB/MHz]. The value of the BUA is all the less strong as the density of the medium is low (therefore in the cortical tissue) [65].

- **SOS (Speed Of Sound) or UBV (Ultrasound Bone Velocity))**

The ratio between the distance traveled by the ultrasounds and the propagation time of the latter expressed in [m/s], is higher in the cortical tissue than in the trabecular. The images obtained are maps of these parameters measured point by point by moving the transducers transmitting and receiving ultrasonic waves. So these are projection images. Some manufacturers combine these two parameters to obtain the QUI (Quantitative Ultrasound Index)
The technique of ultrasound measurement has considerable advantages (non-invasive, non-irradiating nature, low cost), but it seems to be increasingly abandoned by clinicians since it seems less effective than DEXA and QCT when monitoring patients. and their treatment [65].

3.4.4 Magnetic Resonance Imaging (MRI)

In recent years, several studies have been performed that applied magnetic resonance imaging (MRI) for the study of trabecular bone and bone quality.
MRI is an extremely complex imaging technique, that obeys elaborate physical principles. Everything is based on the exploitation of a magnetic field, approximately 4000 to 60000 times the Earth's magnetic field. This field (in Tesla) is created by a magnet which can take different forms, most often a tunnel or 2 discs representing the two poles of the magnet. MRI is based on the magnetic properties of certain atoms with an odd number of protons in their nucleus ($^1H,^{13}C,^{17}O,^{19}F,^{31}P,^{23}Na,^{39}K$). These protons have the particularity of rotating on themselves (spin) thus creating a bipolar magnetic field [65]. They then become comparable to small magnets defined by their magnetic moment. However, knowing that hydrogen has the largest magnetic moment and that the human body is 70% water (H_2O), Magnetic Resonance Imaging is often referred to as proton imaging, H^+. Obtaining an MRI image is essentially based on the variations of signals emitted by these small magnets. Spatial resolutions were obtained in vivo on bone specimens and in vivo at the phalanges, distal radius, and calcaneus. MRI is especially useful for studying muscles, ligaments, and tendons. MRI may be used if

the cause of the pain is considered to be a serious soft tissue problem (for example, a rupture of a major ligament or tendon or damage to major structures within the body 'knee joint').

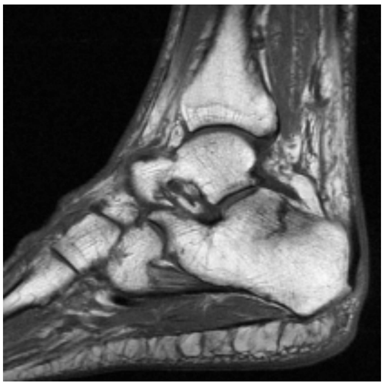

Figure 3.17: Example image of a calcaneus in the left foot obtained from an MRI acquisition sequence.

3.4.5 Radiography (X-Ray)

X-rays do not show soft tissues, such as muscles, bursae, ligaments, tendons, or nerves. Faced with the difficulties observed in performing a real 3D analysis of the trabecular microarchitecture, techniques for analyzing bone radiographs have been developed. Compared to the techniques previously described, radiography has the advantage of being simple to implement and the examination time is very short. This technique requires an X-ray source and a receiver to record and view the resulting image (CCD sensor). X-rays, created by the collision of electrons on atoms of matter, are electromagnetic waves of very short wavelength, between 10E-7 and 10E-11 meters, and carry great energy (electromagnetic energy). These wavelengths of the order of Angström (10E-10 m), are close to interatomic distances, which allows the passage of radiation through matter [76], while radiation of longer wavelength is reflected by the surface of the studied material. A textured grayscale image of the projected trabecular meshwork is obtained as shown in (Figure 3.18).

Three elements are essential to the formation of a radiological image: the radiogenic focus (F), the almost punctual, source of the X-ray beam, the radiographed object (O),

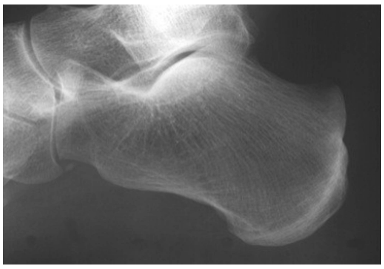

Figure 3.18: Example of an X-ray image of a foot allowing visualization of the calcaneus.

of which we want to form an image, usually the anatomical region and the receiver (R), most often film, but gradually replaced by electronic processes (digital sensors), which supports the useful image. During the formation of the image, a certain number of parameters will influence the quality of the image obtained (Figure 3.19).

The radiographic image is formed by the conical projection of the rays from the focus The two main modes of acquisition of radiographic images are the silver film and the digital sensor.

Generally, X-Rays are more appropriate for detecting bone abnormalities and are done to examine painful, deformed, or suspected abnormal areas of bone, they can often help diagnose fractures, tumors, lesions, infections, and deformities.

Also, X-Rays can sometimes show changes that confirm a person has a certain type of arthritis (for example, Rheumatoid Arthritis or Osteoarthritis).

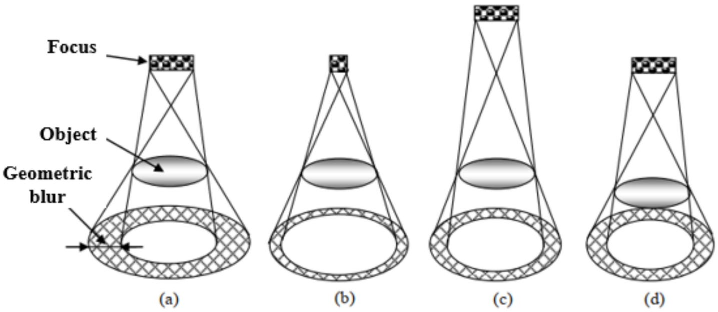

Figure 3.19: Geometric blur. Reference drawing (a). Effect of decreasing focus size (b). Effect of increasing focus-receiver distance (c). Decrease in receiver object distance (d).

Synthesis

CT scan is useful in cases where MRI is not recommended or not available. CT is more suitable for the study of bone. However, MRI is more effective than CT in revealing certain bone abnormalities, such as small hip and pelvic fractures.

CT and MRI scans provide much more accurate detail than traditional X-rays and are used to determine the exact extent and location of the lesion. These tests can also be used to detect fractures that are not visible on X-rays.However, ultrasound is increasingly being used because it is less expensive and, unlike CT, does not involve any radiation exposure. For osteoporosis screening, doctors prefer to take measurements below the spine and hip. To help differentiate osteoporosis from other bone diseases, doctors may need to consider symptoms, conditions, medications being taken, and certain results from blood or bone tests. The person's urine, as well as the results of DEXA. Therefore, The X-ray is considered the best for diagnosing osteoporosis disease.

3.5 Conclusion

The review of the bibliography of the different medical imaging modalities, used to explore the properties of human bone in vivo, as well as the different estimated parameters characterizing the bone microarchitecture, showed that there is a wide spectrum of imaging techniques, which make it possible to situate the place of each system in current clinical use.

The reduced availability and the high investment cost of MRI are major drawbacks in view of an important clinical use. Ultrasound imaging has advantages such as its cost, its small size and its non-irradiating nature, but the prospective studies carried out demonstrate the limits of this technique for detecting variations in Osteoporosis.

The systems, DEXA and QCT are currently the world references for evaluating the risk of fracture linked to Osteoporosis. These two instruments make it possible to perform a quantitative measurement (the BMD), but not a qualitative one (the modifications of the bone microarchitecture).

2D imaging and more particularly X-Ray radiography seems to be a good alternative, due to its many advantages: availability, low irradiation, low cost, non-invasive, etc. Our objective is therefore to contribute to the analysis of X-Ray textures to assess changes in bone microarchitecture related to Osteoporosis.

Chapter 4

Characterization of Textures in Medical Imaging

4.1 Introduction

Texture image analysis is an old subject, found in several application areas such as scene analysis, video, medical imaging, etc.

Texture analysis refers to the discipline of image analysis that deals with the description of image characteristics by textural features. However, there is no universally accepted definition of what is an image texture; in general, different researchers use different definitions depending on their areas of interest [77].

In this chapter, the texture is considered as the spatial variation of pixel intensities, which is a definition that is widely used and accepted in the field of medical imaging. The objective of this chapter is to present a bibliographic review of existing texture analysis methods, with an interest in the techniques used in medical imaging. We will start by defining texture before presenting texture perception properties and classifications. We will highlight the types of textures. Emphasis will be placed on some features of the latter, and we ended with the application domains and the methods of exploitation of the texture characteristics.

4.2 Texture

The texture is also defined as being a region of an image for which it is possible to define a window of minimum size, such that observation through it results in an identical visual perception (impression) for all translation possibilities of this window inside the considered space 'Region'.

The texture is used to translate a homogeneous aspect of objects in an image, so it can be considered as visual information that can be associated with adjectives such as smooth, curly, fine, and coarse [78].

Researchers in visual perception or artificial vision has been trying to characterize it for several years. We recognize texture when we see it, but it is very difficult to define. Shape and color are two other very important characteristics. To discriminate, for example, between an orange and a cherry, the shape and color information are certainly more significant than the texture information. But the texture information becomes essential when we want to discriminate between two areas of an image or two images of the same color or the same level of gray.

4.3 Visual Perception of Texture

Two properties are essential in the way of perceiving a texture:

4.3.1 Regionality

Indeed, the notion of textures appears when a region is composed of a pixel/voxel and a non-zero neighborhood associated with it.

The computation that can be obtained on a texture, therefore, depends very strongly on the size of the neighborhood considered [79]. It is therefore difficult to correctly characterize a texture if the regionality is not chosen appropriately.

4.3.2 Resolution

In the sense that a texture can appear different depending on the level of precision, we characterize what constitutes the basic primitiveness of a texture (sand, stones, etc.), at low resolution, the texture can appear as a neighborhood of the coarser basic

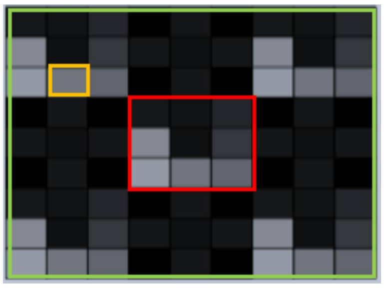

Figure 4.1: Several Regionalities of the same texture, the yellow square: a regionality of 1, we cannot yet speak of textures since the region is described by a single pixel. the red square: a regionality equal to 3^2, contains only part of the patterns present in the texture, and the green square: a regionality equal to 9^2.

patterns, depending on the scale of observation.

The following figure represents the phenomenon of moving away the information concerning the texture at high resolutions lost in favor of low-resolution texture information.

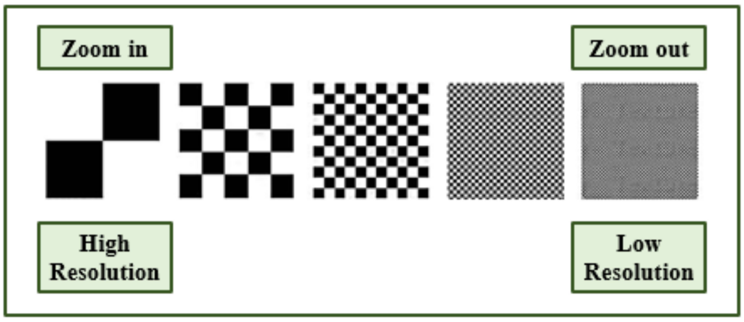

Figure 4.2: Image with different resolution.

4.4 Type of Texture

In practice, we distinguish two main types of textures, which correspond to two levels of perceptions

4.4.1 Macro-Texture

Present a regular aspect, in the form of repetitive patterns spatially placed according to a precise rule, therefore a deterministic structural approach [80].

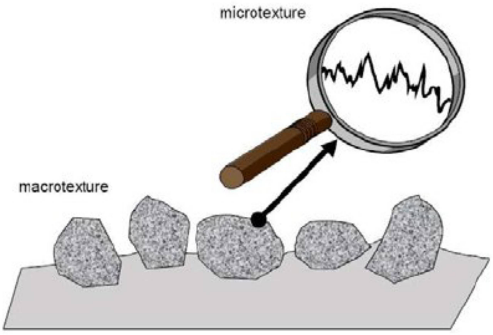

Figure 4.3: Difference between macrotexture and microtexture [81].

4.4.2 Micro-Texture

Present randomly distributed "microscopic" primitives, hence a probabilistic approach seeking to characterize the anarchic and homogeneous aspect.

4.5 Texture Classification

There are three main Classes of textures: Structural, Random, and Directional Texture [82].

4.5.1 Structural Texture

Also called macro-textures, they consist of the more or less regular spatial repetition of a basic pattern, in different directions, (Figure 4.4). shows an example of two Structural Texture images. Several methods of analysis are called structural. These methods are therefore based on the fact that textures are made up of basic structuring elements (textons).

Nevertheless, it is not always possible to characterize the texture by primitives, because there are not always isolatable patterns or dominant spatial repetition frequency. This is the case of random and directional textures (Figure 4.5) and (Figure 4.6).

4.5.2 Random Texture

In these textures, no particular pattern is localizable or detectable. They have an anarchic and disorganized aspect while remaining homogeneous and do not comply with any particular rules of arrangement.

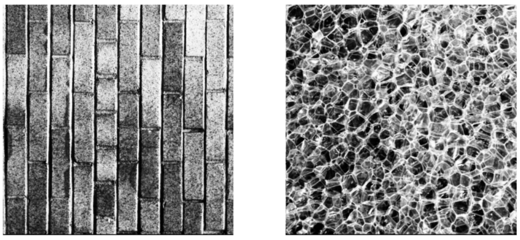

Figure 4.4: Example of two Structural Texture images. Indeed, we see that the image on the left, represents a brick wall, it is composed of a set of basic elements (structuring element, the bricks) arranged regularly in a vertical manner. The image on the right is also composed of basic honeycomb patterns arranged in a particular way next to each other.

For this kind of analysis, the image is considered to be associated with a two-dimensional random process.

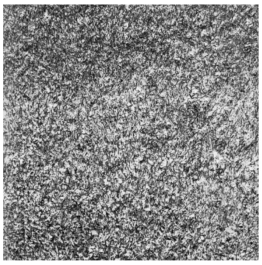

Figure 4.5: Example of the random texture.

4.5.3 Directional Texture

Not random and does not have basic structuring elements. They are essentially characterized by certain orientations. These different categories of texture show that it is difficult to give a precise definition of texture. On the one hand, we have structural and constructive information, and on the other hand, information that is messy and more difficult to describe even visually.
It is, in particular, this type of texture that we will attempt to characterize in our approach to early diagnosis of osteoporosis (Figure 4.6).

4.6 Texture Analysis for Bone X-rays

The analysis of trabecular bone texture from an X-ray image consists in associating a texture with mathematical parameters. In this case, the parameters observed are a combination of the orientation of the spans on the one hand and the connectivity of the network on the other.

Our study aims to develop texture attributes that can quantify bone microarchitectural alterations caused by osteoporosis on X-ray [65].

As a result, four known classes of texture attributes can be distinguished for Bone Analysis: Statistical Features, and Frequency Features.

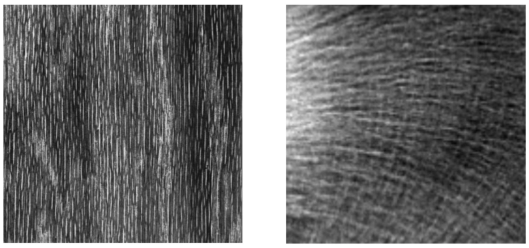

Figure 4.6: Example of Directional texture. The texture on the left shows vertical lines, while the one on the right has curved lines in preferred directions that represent the bone spans.

4.6.1 Statistical Features

Statistical Features are features extracted from textures using mathematical calculations. These features allow the characterization of any type of texture, even fine textures with no apparent regularity. For this type of feature, the texture is defined in terms of variation of the gray level intensity and it is also the relations between the pixels and their neighbors that are studied.

Many statistical descriptors have been used within the framework of the classification or evaluation of the Trabecular Texture. These descriptors can be classified into several categories according to their order, the order of the descriptor depends essentially on the type of spatial interaction between the pixels considered.

1. First-order Statistical Features

The analysis by the first-order Features is done in levels of the individual pixels of a region of the image, the parameters are calculated from the histogram of the intensities, which we find in this case: Image Statistics and Image Histograms.

A. Image Statistics

Many statistics can be directly extracted from an image to characterize the texture it contains. The most commonly used statistics (the Average, the Variance, Skewness, Kurtosis). These statistics only take into account the gray-level information of the pixels and ignore the spatial relationships between them. The characterization of the Trabecular Texture from these features seems inefficient.

B. Image Histograms

They describe the distribution of gray levels in the image to be analyzed. If the pixel intensities are coded on 8 bits, the histogram of the image will then contain 256 cells, each of these cells contains the number of pixels of the image characterized by the level of intensity considered.

However, these histograms are very little used directly for the classification or analysis of bone textures.

Features are usually extracted from these histograms to distinguish between different classes (the Median, the Mode, the Interquartile Range)

As with image statistics, the major drawback of histograms is that they only take into account the gray-level information of pixels and ignore the spatial relationships between them.It is therefore essential to consider higher-order statistical features for a more adequate texture characterization.

- **Histogram of Oriented Gradients (HOG)**

Histogram of Oriented Gradient (HOG) descriptors [83] can be considered as a map of contours containing information about both gradient magnitude and the location of the contours at the cell level. The coarseness of the location and the normalization of HOG features are essential as they provide a certain level of invariance to minor geometric and photometric modifications [113]. To create an HOG function, we begin with an input window I of a grayscale image with dimensions $H \times W$, or even the entire image, and follow these steps:

Calculating Gradients: Determine the components of the gradient, i.e., horizontal and vertical derivatives, for each pixel in the image (I_x, I_y) by:

$$\begin{cases} I_x(i,j) = I(i,j+1) - I(i,j-1) \\ I_y(i,j) = I(i-1,j) - I(i+1,j) \end{cases} \quad i = 1..H, j = 1..W \tag{4.1}$$

The gradient is converted into polar coordinates, with the angle constrained to a range of 0o to 180o degrees, to detect opposing gradients.

$$\begin{cases} \mu = \sqrt{I_x^2 + I_y^2} \\ \theta = \frac{180}{\pi}(tan^{-1}(I_x, I_y) mod \pi) \end{cases} \tag{4.2}$$

Here, the inverse tangent function (denoted by tan^{-1}) is used to calculate the angle (between $-\pi$ and π) and the magnitude (represented by μ) of the gradient for each pixel, with θ indicating The gradient's direction.

Histograms of Cell Orientation: The window is divided into adjacent, non-overlapping cells of size $c \times c-$ (with c set to 8), and For every individual cell, a histogram of gradient directions is generated using B bins (where B is equal to 9). This results in bins Assigned a numerical value ranging from 0 to $B - 1$, All having the same width of $w = \frac{180}{\pi}$.

It should be emphasized that the limited number of bins used in the HOG descriptors can result in the misclassification of A pixel positioned on a boundary between two bins if the image undergoes significant changes. To address this issue, the HOG algorithm employs a technique called voting by bilinear interpolation, this approach enables every pixel within a cell to contribute to both adjacent bins [114]. In this approach, the gradient magnitude of each pixel is apportioned between two bins by taking into account the proximity of the gradient orientation to the midpoint of each bin, This process allows for approximating the distribution of gradient magnitude over the two bins [113]:

$$F_{vote} = (\mu_i, \theta_i, B_i, B_{i+1}) = \begin{cases} k_1\mu \rightarrow B_i \\ k_2\mu \rightarrow B_{i+1} \end{cases} \quad /k_1 + k_2 = 1 \tag{4.3}$$

As the gradient magnitude is always positive, the resultant histogram for each cell is a vector of length $B-$.

Normalization Using Block Technique: This phase involves the grouping of cells into blocks of $2c \times 2c$ pixels, where the blocks overlap by c pixels in both horizontal and vertical directions. To obtain a feature descriptor for each block, the histograms of the four cells within the block are combined or concatenated into a single vector, resulting in a block feature descriptor. The resulting block features are The concatenated block feature is then subject to Euclidean normalization, ensuring that the descriptor is invariant to changes in illumination and contrast [114]:

$$b_k = [h_{(i,j)}, h_{(i,j+1)}, h_{(i+1,j)}, h_{(i+1,j+1)}] \tag{4.4}$$

In the above equation, b_k represents the feature vector of block k, while $h_{(i,j)}$ represents the histogram of the cell (i, j). Normalization of the block feature vector is achieved using the following formula:

$$\tilde{b}_k = \frac{b_k}{\sqrt{\|b_k\|^2 + \varepsilon}} \tag{4.5}$$

In the normalization step, ε is added to the denominator to prevent division by zero in blocks with a zero gradient.

HOG Feature: The normalized feature vectors for all blocks, denoted as $\tilde{b}_k$, are concatenated to create a single HOG feature vector (H) that represents the entire window feature, as illustrated below:

$$H = [\tilde{b}_1, \tilde{b}_2, ..., \tilde{b}_k, ..., \tilde{b}_\rho] \tag{4.6}$$

Here, ρ represents the total number of blocks within the window. Lastly, The HOG function obtained after the normalization of block feature vectors is further normalized using (Equation 4.5). [114].

2. Second-order Statistical Features

In the first order, there is no information on pixel location, therefore, it is necessary to use the second-order features.

- **Co-occurrence Matrix**

Used to determine the frequency of appearance of pairs of pixel values located at a certain distance in the image. It is based on the calculation of the probability, which represents the number of times a pixel of the gray level appears at a relative distance from a pixel of the gray level and according to the orientation of the straight line connecting these two pixels concerning the horizontal (θ). We generally take the value 1 for the relative distance and $\theta = 0°$, 45°, 90° and 135°.

The neighborhood relations between pixels concerning the orientation, necessary for the calculation of the co-occurrence matrices, are illustrated in (Figure 4.7).

From the co-occurrence matrices, we have created a whole series of new descriptors (a limited number this time) making it possible to highlight the most important parameters of these co-occurrence matrices. the 6 parameters considered to be the most used and the most relevant:

Energy (ENE), Contrast (CST), Entropy (ENT), Variance (VAR), Correlation (COR), and Inverse Difference Moment (IDM).

Recently, many studies have been conducted to characterize and classify bone textures using these parameters [81].

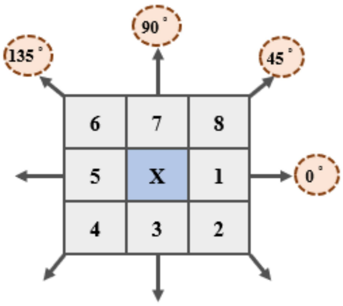

Figure 4.7: Eight nearest neighbor pixels are used to calculate the co-occurrence matrix. the nearest neighbors of x along the direction $\theta = 0°$ are pixels 1 and 5, for $\theta = 45°$ pixels 4 and 8, for $\theta = 90°$ pixels 3 and 7 and finally for $\theta = 135°$ pixels 2 and 6.

3. Higher-order Statistical Features

- **Run-length Matrix**

Based on the analysis of Higher-order Statistical data. A range is a connected and linear set of pixels having the same gray level. This method, therefore, consists, firstly, in determining all the ranges present in the image and, secondly, of extracting statistics on their length. We thus define several matrices, each corresponding to an orientation θ of the ranges in the image.

It is therefore a question of finding the maximum number of adjacent pixels having the same level of gray in one direction.

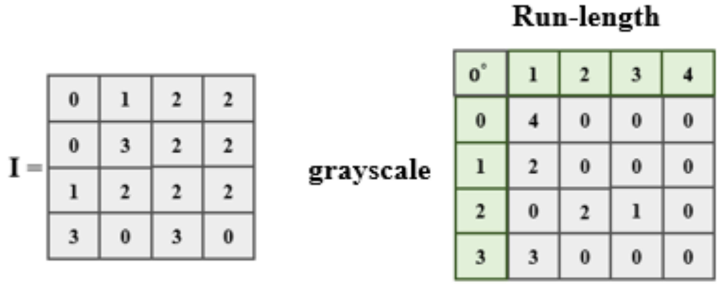

0	1	2	2
0	3	2	2
1	2	2	2
3	0	3	0

0°	1	2	3	4
0	4	0	0	0
1	2	0	0	0
2	0	2	1	0
3	3	0	0	0

Figure 4.8: Simple example showing the formation of a Run-length Matrix. On the left, a 4×4 pixel image with only 4 levels of gray. On the right is the resulting Run-length Matrix at $\theta = 0°$. The gray table represents the Run-length Matrix.

Galloway proposed five parameters calculated from these matrices and considered as texture features, five numbers of features such as Short Run Emphasis (SRE), Long Run Emphasis (LRE), Gray Level Non-uniformity (GLN), Run Length Non-uniformity (RLN), and Run Percentage (RP) [85].

Similar to co-occurrence matrices, this method has been adopted by several researchers as an aiding tool for classification, osteoporosis assessment, and trabecular texture analysis.

4.6.2 Spatio-Frequency Features

The Spatio-Frequency Features are divided into three categories: the features which are calculated in the Spatial Domain, the features calculated in the Frequency Domain, and the features extracted from the Spatio-Frequency Domain, as shown in (Figure 4.9).

1. Spatial Domain

In this spatial domain, the calculation of texture features consists of characterizing the texture by the number of transitions per unit area.

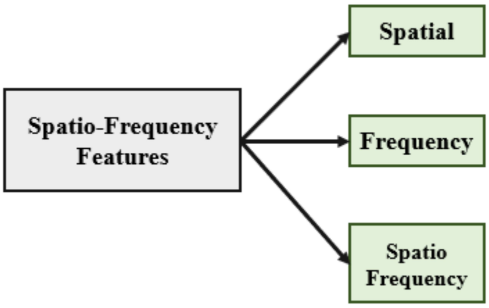

Figure 4.9: Spatio-Frequency Features categories

2. Frequency Domain

Computing texture features in the frequency domain consist of performing a transformation from the spatial domain to the frequency domain.

A. Texture Analysis by the Fourier transform

This approach consists in extracting the frequency characteristics of the texture. The two-dimensional discrete Fourier transform is most often used to classify textures. The gray level of a pixel is expressed here by the weighted sum of complex exponential functions corresponding to different spatial frequencies. The low-frequency terms represent the smooth variations of gray levels in the image, while the high-frequency terms represent the rapid variations.

- **Local Phase Quantization (LPQ)**

Local Phase Quantization (LPQ) [84] is a technique that captures local phase information from an image that has been blurred, Utilizing the ability of the Fourier phase response to remain invariant to blurring.

Local Frequency Analysis: In order to use the LPQ operator on a pixel in an image, the Short-Term Fourier Transform (STFT) is utilized within a window of size $(M \times M)$, denoted as W_n. For an image with dimensions $(H \times W)$, The local image patches inside W_n are specified for every pixel location $x = x_1, x_2, ..., x_{HW}$ in the following manner:

$$f_x(y) = f(x - y), \qquad \forall y \in W_n \tag{4.7}$$

By applying STFT, we obtain the local representation of the image in the frequency domain:

$$F_x(u) = \sum_{y_i \in W_n} f_x(y_i) e^{-j2\pi u^T y_i} \tag{4.8}$$

Here, i ranges from 1 to M^2, and the variable u is composed of l frequency variables, denoted as $(u_1, u_2, ..., u_l)$, which serve as local descriptors that are insensitive to blur. (Equation 4.8) can be rephrased as follows:

$$F_x(u) = \psi_u^T f_x, \qquad \psi_u^T(y) = e^{-j2\pi u^T y} \tag{4.9}$$

where:

$$\psi_u^T = [\psi_u(y_1), \psi_u(y_2), ..., \psi_u(y_{M^2})] \tag{4.10}$$

and:

$$f_x = [f_x(y_1), f_x(y_2), ..., f_x(y_{M^2})] \tag{4.11}$$

Decorrelation is performed by applying a linear transformation that converts the original samples into a new set of independent samples. In the case of LPQ, decorrelation is achieved by computing the local phase of each pixel relative to its surrounding neighborhood. The phase is then quantized into L equally spaced bins, and each pixel is assigned a label according to which bin its phase falls into. The resulting sequence of labels forms the LPQ codeword.

Phase Quantization: The technique of blur-insensitive representation involves utilizing a set of frequencies l, which generates a feature vector of the same length l for every pixel. In practical applications, the quantization of the phase into four quadrants is achieved through the use of the following quantizer:

$$\mathcal{Q}(F_x(u)) = (Re\{F_x(u)\} > 0) + 2(Im\{F_x(u)\} > 0) \tag{4.12}$$

For each pixel, the quantization process described above requires 2 bits to represent each frequency component, resulting in a total of $2l$ bits. These bits are concatenated to form a single codeword. Since the low-frequency components of an image typically contain the bulk of its energy, only these components are utilized in generating a blur-insensitive representation. In practical applications, the local coefficients F_x are computed at four low frequencies, with $l = 4$, for each pixel.

$$[u_1, u_2, u_3, u_4] = \begin{bmatrix} a & 0 & a & a \\ 0 & a & a & -a \end{bmatrix} \tag{4.13}$$

The value of scalar a corresponds to the highest positive frequency in the Point Spread Function (PSF) and is typically calculated using M, that is, $a = \frac{1}{M}$.
Subsequently, an 8-bit codeword, denoted as $([q_7, q_6, q_5, ..., q_0])$, It is possible to acquire a description of the local texture encompassing each pixel in W_n by utilizing reference [84]. A straightforward binary decoding process can readily convert this codeword into a decimal number between 0 and 255:

$$LPQ_i = \sum_{j=1}^{8} q_i 2^{j-1} \tag{4.14}$$

Decorrelation: If the coefficients that require quantization are interdependent, vector quantization tends to be more efficient. In order to eliminate correlation between frequency coefficients, the first step is to split $F_x(u)$ into its real and imaginary components, and then combine them by concatenation using the following approach:

$$F_x(u) = [F_x(u_1), F_x(u_2), ..., F_x(u_l)] \tag{4.15}$$

$$F_x = [Re\{F_x(u)\} \quad Im\{F_x(u)\}] = [F_x^R \quad F_x^l] \tag{4.16}$$

The STFT transformation shown in (Equation 4.9) indicates that F_x and f_x are linearly dependent, allowing us to express this relationship as follows:

$$F_x = \psi.f_x \tag{4.17}$$

where:

$$\psi = [\psi_R \quad \psi_l]^T \tag{4.18}$$

and:

$$\psi_R = Re\{\psi_{u_1}, \psi_{u_2}, ..., \psi_{u_l}\} \tag{4.19}$$

and:

$$\psi_l = Im\{\psi_{u_1}, \psi_{u_2}, ..., \psi_{u_l}\} \tag{4.20}$$

Ojansivu et al. [86] proposed a transform to decorrelate F_x, which is given by the following expression:

$$G_x = V^T.F_x \tag{4.21}$$

The orthogonal matrix V used to perform the decorrelation of F_x is obtained from the matrix D, which is defined as follows:

$$D = U \sum V^T \tag{4.22}$$

The matrix D, which is the covariance matrix of F_x, can be computed using the following expression:

$$D = \psi \; C \; \psi^T \tag{4.23}$$

Where C is the $M \times M$ covariance matrix of samples in W_n. Following the decorrelation process, a scalar quantizer quantizes the j^{th} coefficient (g_j) of G_x [113]:

$$q_j = \begin{cases} 1, & if \quad g_j \geq 0 \\ 0, & otherwise \end{cases} \tag{4.24}$$

The LPQ operator computes a codeword for each pixel in the image, and these codewords are transformed into a decimal number between 0 and 255 to create an LPQ image that contains the information about the texture of the input image at a local level. To generate an LPQ feature vector for the whole input image, the LPQ image is divided into non-overlapping sub-regions of size $r \times c$, and histograms are computed for each sub-region. Finally, the histograms are merged together to form the LPQ feature vector.

$$H = [h_1, h_2, ..., h_{rc}] \tag{4.25}$$

To retain specific details about the spatial distribution of patterns, it is necessary to partition the LPQ image into disjointed sub-regions. When histograms are computed for each sub-region, this information is not lost as it would be if histograms were computed for the whole image [84].

B. Texture Analysis by the Autocorrelation Function

An important property of some textures is the repetitive nature of texture-structuring elements in the image. The Autocorrelation Function (ACF) of an image can be used to assess the rate of regularity such as the fineness or coarseness of the texture present in the image (Figure 4.10).

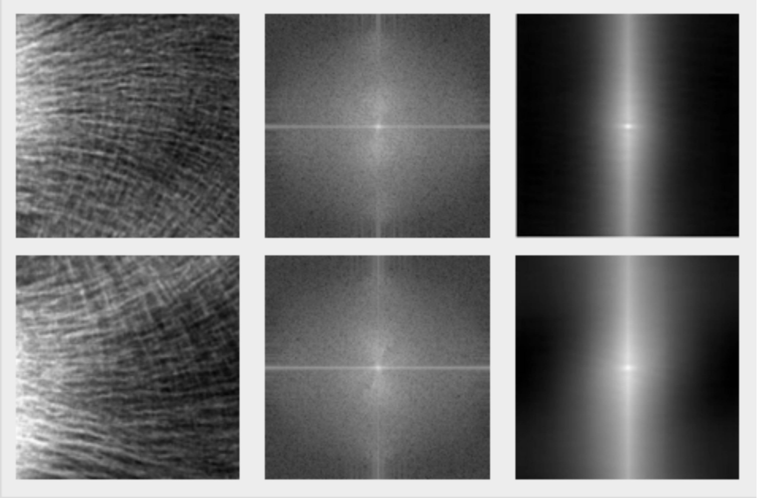

Figure 4.10: First column, Two bone x-rays of the calcaneus. The upper image is for a healthy subject, the Lower image is for an osteoporotic patient. The second column presents their Energy Distribution in the power spectrum for the two trabecular textures (The Fourier transform) and the third column presents their Autocorrelation Function performed on the two bone x-rays.

3. Spatio-Frequency Domain

This type of texture features associates both spatial and frequency domains. Some of them are presented in this section.

A. Gabor transformation

- **Gabor Filter Bank**

A Gabor filter's [87] impulse responseA function that exhibits a sine or cosine wave-like pattern can be referred to as a sinusoidal function The given function has undergone multiplication by a Gaussian function. According to the source cited as reference 84, a $2-D$ complex Gabor filter with dimensions of N_x by N_y in discrete space can be expressed as:

$$G_{(\theta,f_0,\gamma,\eta,\phi)}(x,y)=\frac{\gamma.\eta}{\pi}e^{-((\alpha x_\gamma)^2+(\beta x_\gamma)^2)}e^{j2\pi f_0(x_c cos\theta+y_c sin\theta+\phi)} \tag{4.26}$$

with:

$$\alpha=\frac{f_0}{\gamma} \qquad ,\beta=\frac{f_0}{\eta} \tag{4.27}$$

The phase of sinusoidal rotation, digital frequency, and carrier phase are the parameters associated with the sinusoidal wave represented by θ, f_0, and ϕ, respectively, in a Gabor filter. Additionally, According to reference [113], the normalized scale factors for the along-wave envelope and the wave-orthogonal Gaussian envelope are represented by γ and η, respectively.

$$\begin{cases}(x_c,y_c)=(x-x_0,y-y_0),(x_0,y_0)=(\frac{N_x}{2},\frac{N_y}{2})\\ x_r=x_c cos(\theta)+y_c sin(\theta)\\ y_r=-x_c cos(\theta)+y_c sin(\theta)\end{cases} \tag{4.28}$$

The Gabor filter exhibits several fascinating properties such as invariance to illumination, rotation, scale, and translation. It is also localized both in the spatial and frequency domains, which makes it an ideal candidate for wavelet analysis. In practical applications, filter banks [88] consist of numerous Gabor filters that form a Gabor space. The principles governing the functioning of the human visual cortex are also utilized in the operations of this space and can rapidly detect intricate visual patterns. Referring to Equation (4.26), The definition of the collection of K-component Gabor filters, represented by W, is given below:

$$W_{n,m}(x,y)=G_{(\theta_m,f_{0n},\gamma,\eta)}(x,y) \qquad /\phi=0 \tag{4.29}$$

The number of Gabor filters in a given setup is denoted by $\mathcal{K}$ and is equal to the product of the number of scales, represented by K_s, and the number of orientations, represented by K_o.

$$\begin{cases} f_{0n} = \frac{f_0}{(\sqrt{2})^{n-1}} & n = 1, ..., K_s \\ \theta_m = (m-1)\frac{\pi}{K_o} & m = 1, ..., K_o \end{cases} \tag{4.30}$$

To calculate the values of α and β for each component or scale, the following procedure is typically used:

$$(\alpha_n, \beta_n) = (\frac{f_{0n}}{\gamma}, \frac{f_{0n}}{\eta}) \tag{4.31}$$

The Gabor filter set, denoted by W, consists of various components, Each element in the collection represents a sine angle (θ_m),specific square Gabor filter size and (f_{0n}) digital frequency. These parameters are usually selected empirically to achieve a better description of bone line details.

B. Wavelet Transform

Gabor's representation is based on an observation window of fixed length, which can be a drawback because some textures can be characterized according to different scales. To remedy this limitation, the wavelet transform is based on multi-scale analysis of the texture, in the sense that analysis windows of different sizes are used [89]. Many statistical or co-occurrence attributes (Wavelet Statistical Features (WSF) and Wavelet Co-occurrence Features (WCF)) can be extracted from the wavelet transforms of an image. The energies calculated for the different filters are also used to characterize the textures with a view to classification. The advantage of this transformation is that it allows a multi-scale characterization of the texture by considering both the global and local information contained in the image.

4.7 Deep Feature and Proposed Method

The distinction easily made by the human eye between several textures is a difficult task to achieve in computer vision, insofar as there are an infinite number of textures and each one has its characteristics. There are no methods capable of classifying all textures as well as a human observer would, however, a certain number of properties defining the visual impressions can be extracted and therefore make it possible to best reproduce the classification of texture carried out by this method. human observer.

Features can be defined as numeric type data describing the content of an image. Osteoporosis can lead to significant changes in bone structure and porosity, especially as the disease advances. As a result, bone images can exhibit instability and alterations in line and pore density. In healthy bones, line density increases while pore density decreases, but the opposite is observed in diseased bones. Consequently, these features can provide valuable information and aid in the accurate diagnosis of osteoporosis progression. Due to the significant overlap in bone structure between healthy and diseased bones, it's crucial to focus exclusively on these features for effective diagnosis. Unfortunately, previous studies have often been limited by the inefficient use of bone line and pore imaging data for osteoporosis diagnosis.

Without taking into consideration these features, a texture analysis-only approach can lead to feature vectors that exhibit increased rates of interclass correlation. Our proposed method is designed to produce distinctive features by following this principle:

1. The process involves extracting lines and/or pores in multiple orientations or directions.
2. The system automatically adjusts its parameters to handle diverse scenarios, such as lines with different thicknesses.
3. Multi-level analysis capability.
4. Ability to conduct multiple bone image analyses, after the integration of results allows for the system to make a well-informed decision.

We have suggested a Deep Analysis method based on Convolution to describe the texture of the X-Ray image of bones. In order to improve the contrast of the bone images, each image received initial preprocessing. We will go into more information about the techniques implemented in the suggested approach below. The aim is to identify feature vectors that exhibit strong similarities within a class and significant differences between classes, Considering the strong similarity between bone images of healthy and diseased samples. For our Deep Analysis method, we utilized a dataset obtained from the IEEE-ISBI Challenge: Characterization of Bone Tissue (explained in Appendix A). In 3D pictures, the osteoporosis-related bone tissue can be shown to frequently decrease in depth. Unfortunately, our dataset only contains 2D images, making it difficult for specialists to diagnose the condition with their naked eyes, Handcrafted feature extraction methods have proven to be ineffective in generating distinct vectors for automated diagnosis [113].

Taking inspiration from the benefits of Deep Analysis and Gabor's descriptor, we present a new method for extracting features to detect Osteoporosis in this section. (Figure 4.11) illustrates the complete feature extraction process, which includes Gabor filtering, data reduction, and feature vector extraction.

The objective is to detect various image features such as wrinkles, lines, singular points, ridges and texture, we will utilize a Gabor filter bank with specific orientations. The Gabor transform-based feature space enables This enables us to extract features specific to bone tissue, particularly the lines, from their surrounding areas in the processed image. Through the identification of gradual variations in the dimensions, configuration, and intensity of lines in a bone image, osteoporosis can be diagnosed. Next, Our approach involves combining all the filtered images into a unified descriptor to minimize the data size. To generate a feature vector, we will use HOG/LPQ to process the descriptor in the last stage. The parameters of the Gabor Filter Bank will be optimized during training utilize Bat Algorithm Optimization to obtain precise feature vectors.

For the purpose of discussing the system's architecture, we will make the assumption that This method assumes that the input images have dimensions of $H \times W$ and utilizes a patch size, which refers to the size of the 2D convolutional filter, for the convolution layer:

$$W_{(n,\theta_i)} = k_1 \times k_2 \qquad i \in [1..N] \tag{4.32}$$

In our work, the scale number n ranges from 1 to 8. We employ 16 orientations of Gabor filters θ, with values ranging from 0 to π and a step size of π /16. The quantity of filters utilized is denoted as N. It is important to note that the system must be supplied with the scale number and filter count, which can be less than eight filters. In the following section, we will describe our approach for selecting The angular positions of the filters.

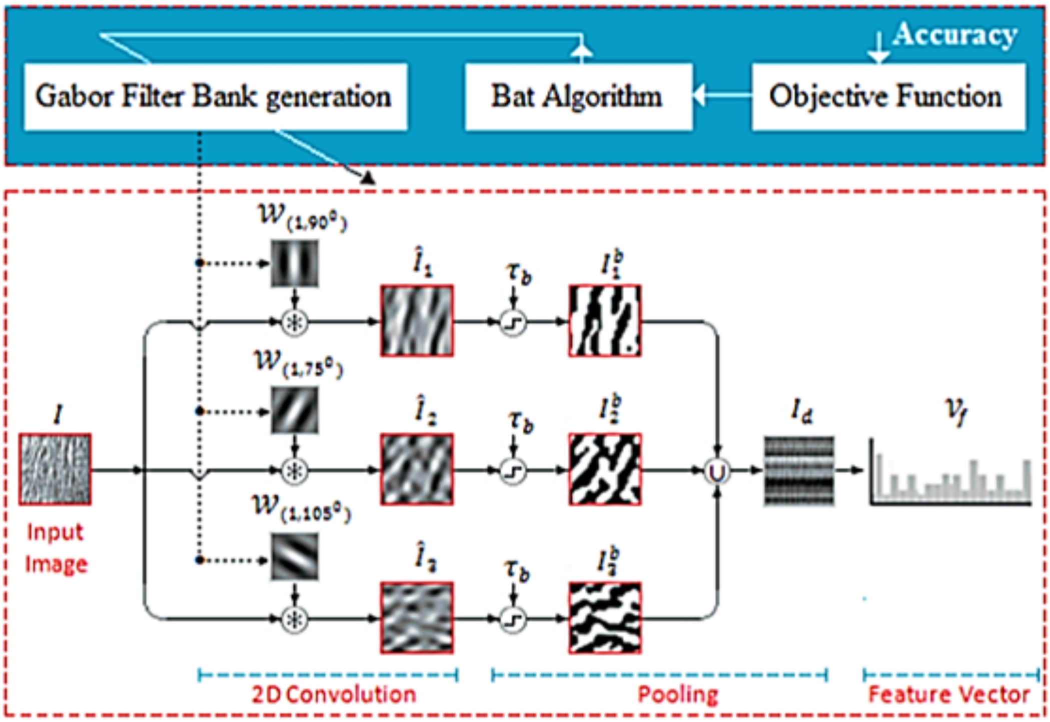

Figure 4.11: Example of One-Scale Feature Extraction Structure with Convolution Filters of Different Orientations

4.7.1 Orientations of Gabor filters.

By filtering an image, the intention is to highlight its crucial features. For this reason, the orientation of the Gabor filter chosen is of paramount importance and should be dependent on the features that require highlighting. In the bone image displayed in (Figure 4.12), the most prominent feature is the lines, which are typically vertically inclined.

(Figure 4.12) shows line orientations in images. Top to bottom is the prevailing direction of the lines and are typically within an angle range of $90° \pm 30°$. (Figure 4.12(a)) Represents an image with a particular orientation of around 75°, while (Figure 4.12(c)) Indicates an image with an orientation of roughly 105°. In contrast, the lines in the image shown in (Figure 4.12(b)) point in the direction of 90°. Generally, the orientations of the lines are determined by The quantity of filters employed, with a preference for vertical directions., as illustrated in Figure 4.12(d) [113].

Mathematically, the orientation of each Gabor filter can be expressed as follows if N is the total number of filters:

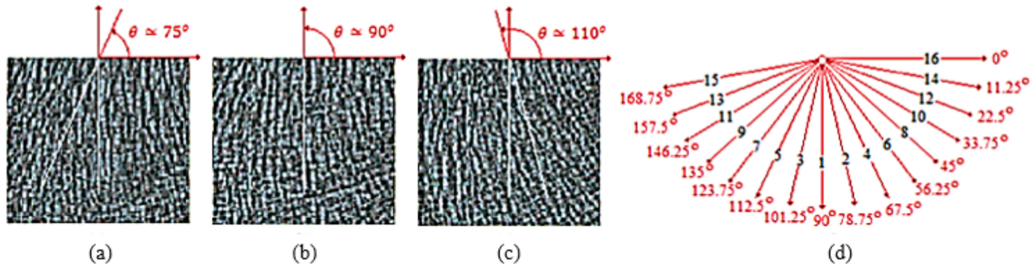

(a) (b) (c) (d)

Figure 4.12: Choosing the orientations of Gabor filters involves considering: (a) lines predominantly located in the first quadrant, (b) a tendency towards vertical lines, (c) lines mostly situated in the fourth quadrant, and (d) the preferred orientation.

if N odd: $N = 2p + 1 \quad \Rightarrow$

$$S_\theta = \{\theta_j\}_{j=0..p}, \quad \theta_j = \frac{\pi}{2} \pm j\frac{\pi}{16}, \quad p = \frac{N-1}{2} \tag{4.33}$$

if N even: $N = 2p \quad \Rightarrow$

$$S_\theta = \{\theta_j\}_{j=0..(p-1)} \cup \left\{\frac{\pi}{2} + \frac{N}{2}.\frac{\pi}{16}\right\}, \quad \theta_j = \frac{\pi}{2} \pm j\frac{\pi}{16}, \quad p = \frac{N-1}{2} \tag{4.34}$$

To improve the accuracy of the system, we chose to increase the step size to $\frac{\pi}{16}$ when selecting the orientations of the filters. However, it is possible to adjust this step size to further improve accuracy if needed. With the scale number and filter orientations determined, we can now explain The performance of our feature extraction technique can be described in terms of its functional behavior.

4.7.2 Functional Architecture

In the following section, we'll explore how the feature extraction function operates to produce a precise feature vector that optimizes performance.

1. Convolution Layer

The primary goal of a convolutional layer is to emphasize the essential features present in the input image. Besides the filter size, the filter orientation or variance is also crucial, this is because the size of the surrounding pixels used in calculating the coefficient for each pixel is determined by this specification. The layer generates its outputs by convolving all the images in the training database (ψ_{train}) with the filters $\mathcal{W}(n, \theta i)$ through a 2D convolution process [113]:

$$\widehat{I}_{ji} = I_j * \mathcal{W}_{(n,\theta_i)}, \quad i \in [1..N], \quad \theta_i \in S_\theta, \quad j \in [1..N_{train}] \tag{4.35}$$

The notation N_{train} represents the total number of images within the set ψ_{train}. The 2D convolution process is denoted by the symbol *, which results in filtered output images are denoted as $\widehat{I}_{ji}$.

2. Pooling Layer

The application of N filters to images results in the generation of N supplementary images, which increases the data significantly. To reduce the data while retaining image features, we use a pooling layer.High and positive values represent the significant features, making it possible to locate them using quantization. To accomplish this, we employed the following linear threshold function in our research:

$$I^b_{ji}(x, y) = \begin{cases} 0 & if \quad \widehat{I}_{ji}(x, y) < \tau_b \\ 1 & if \quad \widehat{I}_{ji}(x, y) \geq \tau_b \end{cases}, \quad i \in [1..N] \tag{4.36}$$

where τ_b is the threshold for binarization. In our study, we established a threshold of 0 for the coefficients of the filtered image ($\widehat{I}_i(x, y), \forall x, y$) as they had an equal likelihood of being negative or positive. Subsequently, the N-binarized images ($I^b ji \mid i = 1..N$) are transformed into an image with integer values. Afterwards, the codeword consisting of N binary digits around each pixel is subjected to the following formula [110]:

$$I_{ji}(x, y) = \sum_{i=1}^{N} I^b_{ji}(x, y) \cdot 2^{(i-1)} \tag{4.37}$$

Consequently, we will obtain a singular image that will undergo A feature extraction algorithm that is performed manually is used to isolate its features.

3. Feature Vector Layer

At this stage, an expert-designed feature extraction technique such as HOG and/or LPQ is employed to process the analyzed image. (I_j) and generate a feature vector ($\mathcal{V}_I$).

$$\mathcal{V}_j^{MTD} = \mathcal{F}_{MTD}(I_{jd}), \quad MTD \equiv \{HOG, LPQ\} \tag{4.38}$$

Both the HOG and LPQ methods have multiple parameters that can be apdated to regulate the size and accuracy of the feature vector. The precision of the vector influences the detection system's effectiveness; thus, we quantized and selected its coefficients during the training phase using the following formula:

$$\widetilde{\mathcal{V}}_j = \mathcal{F}_{QNTZ}(v_j(x)) = \begin{cases} v_j(x) \quad if \quad v_j(x) \geq \lambda_0 \cdot \rho_v \\ 0 \qquad Otherwise \end{cases}, \quad \widetilde{\mathcal{V}}_j \in \mathbb{R}^{1\times L}, \quad w \in [1..L] \tag{4.39}$$

and:

$$v_j = \mathcal{F}_{SLCT}(\widetilde{\mathcal{V}}_j^{MTD}) \tag{4.40}$$

Here, v_j signifies the feature vector that is rearranged based on the coordinates obtained through Fisher's selection method [90]. This method generates a vector with a predetermined number of coordinates (L) sorted in descending order of significance. Additionally, ρ_v denotes the average value of v_j, while λ_0 represents a predetermined value.

4.7.3 Optimization

In general, an optimization algorithm is a computational mathematical process for finding the minimum or maximum of an objective function (optimization problem). Metaheuristic algorithms treat optimization problems like a black box. These algorithms have shown their performance in various areas of optimization, they could lead to the resolution of optimization problems whether they are constrained or unconstrained, complex, multimodal, or discontinuous, without having any particular knowledge of the objective function or its differential information.

Three parameters (f_0, γ, and η) are required to construct a Gabor filter bank. In our study, during the training phase, we utilized the Bat Algorithm Optimization to determine the optimal settings that enhance the system's performance (f_0^{best}, γ^{best}, and η^{best}) [87].

$$[f_0^{best}, \gamma^{best}, \eta^{best}] = \mathcal{F}_{OPT}(S_{accuracy}) \tag{4.41}$$

where $S_{accuracy}$,The objective function in our study, which is represented by the system's accuracy, is the metric used to evaluate performance.

- **Bats Algorithm**

A metaheuristic optimization method, proposed by Xin-She Yang in 2010, is an optimization method based on the echolocation behavior of micro-bats in the hunting process. The micro-bats produce a sonar vibration which locates the position of prey in the search space, the micro-bats could locate a target thanks to an echo received this phenomenon is called echolocation.

Each microbat is characterized by five variables, the frequency f_i , the velocity v_i, the position x_i, the loudness A_i , the pulse rate r_i.These variables are calculated using the following equations:

$$\textbf{Frequency:} \qquad f_i = f_{min} + (f_{max} - f_{min})\beta \tag{4.42}$$

With, f_{min} and f_{max} Depending on the nature of the problem, β is a random number between 0 and 1.

Velocity:

$$v_i(t+1) = v_i(t) + (X_i(t) - X_{best})f_i \tag{4.43}$$

$v_i(t+1)$ is the new velocity of bat i, and $X_i(t)$ is its current position, X_{best} is the current best position.

Position:

$$X_i(t+1) = X(t) + v_i(t+1) \tag{4.44}$$

Loudness and Pulse rate: Initially, it is calculated using the following equation:

$$A_i = rand \times (A_{max} - A_{min}) + A_{min} \tag{4.45}$$

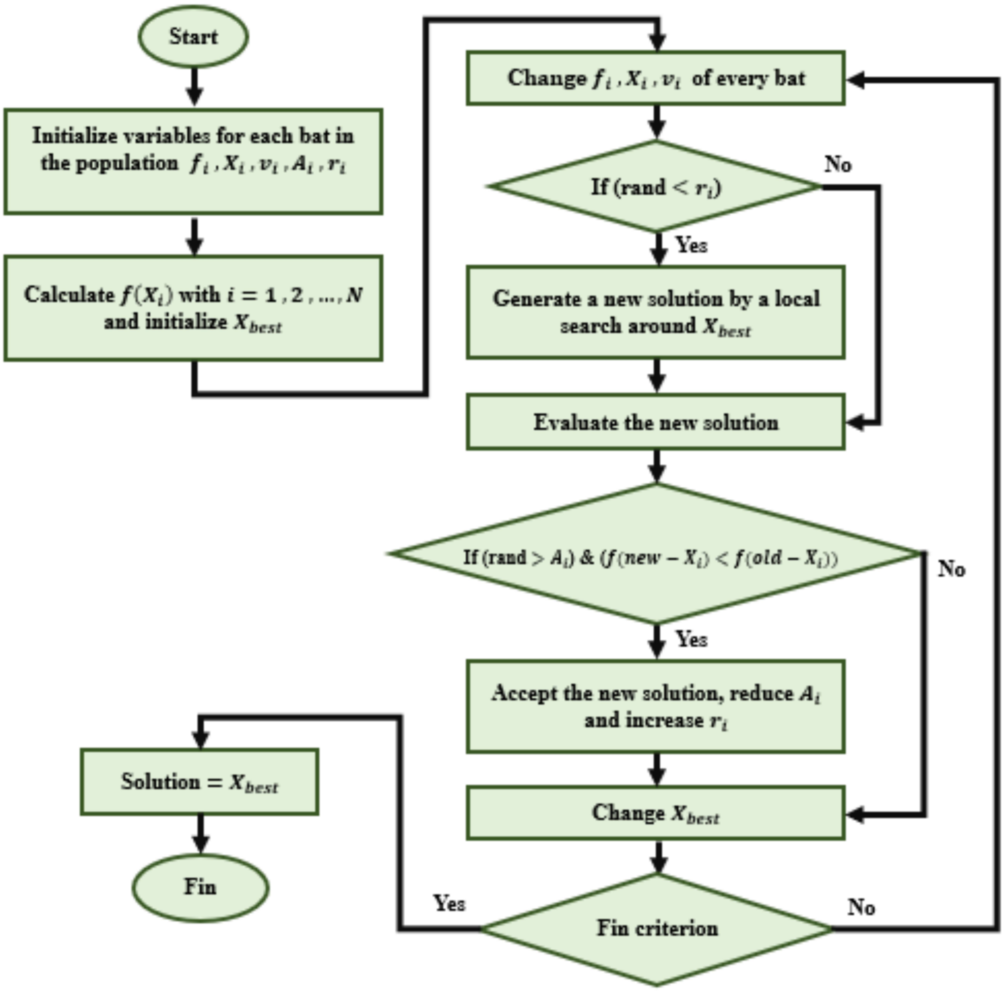

Figure 4.13: The organization chart of the BAT algorithm.

$$r_i = rand \times (r_{max} - r_{min}) + r_{min} \tag{4.46}$$

If the generated random number is smaller than A_i and $f(X_i)$ is less than $f(X_{best})$, Thereafter decreases A_i and r_i in each iteration according to the following equation with, f denote the objective function:

$$A_i = \alpha A_i^t \quad with \quad 0 < \alpha < 1 \qquad r_i = r_i^t[1 - e^{-\gamma^t}] \quad with \quad 0 < \gamma \tag{4.47}$$

The organization chart of the BAT Algorithm is shown as follows in (Figure 4.13)

4.8 Conclusion

In this chapter, we have presented the main approaches used for the characterization of textured images and in particular images of bone radiographs. Texture analysis is a difficult problem. This difficulty is essential because there is no precise and rigorous definition allowing the notion of texture to be completely defined.

The choice of texture features in general is a delicate point since it depends on several factors. The features should therefore be chosen with care because not only do they depend on the application considered, but they also influence the quality of the discrimination. Our objective is to propose an approach that allows extracting from images of bone radiographs, information characteristic of the texture. We then described the approach that we propose for the extraction of the different features of bone textures and which will be used in the classification phase. The concepts of classification as well as the methods commonly used for the classification of textures have been presented synthetically.

Chapter 5

Experimental Results: Implementation and Results

5.1 Introduction

Supervised Machine Learning techniques can effectively differentiate between images of healthy and diseased bones by analyzing their texture characteristics. The texture analysis provides a rich set of data that can be used to successfully classify the images. Specifically, The size and density of texture lines are crucial factors in determining the probability of osteoporosis and the extent of bone loss.

The proposed approach in this study involves applying a specific set of Gabor filters to the raw image, which enables extraction of various orientations of lines. The resulting features are merged or combined into a single descriptor, which is then subjected to various handcrafted feature extraction algorithms. A classifier is used to optimize the Gabor filter settings by utilizing a bat-inspired algorithm to attain optimal performance and enable deep analysis behavior. Furthermore, the proposed method is capable of functioning based on the multimodality principle, which combines information from HOG and LPQ or texture analysis utilizing various filter sizes. The experimental results indicate that this deep texture analysis approach is highly effective in accurately analyzing bone images, outperforming previous studies [113].

To evaluate the effectiveness of the proposed osteoporosis diagnosis system, a three-part experiment was conducted in this chapter. Firstly, a comprehensive evaluation of the proposed method was carried out. Secondly, the optimal settings for the feature extraction method were determined. Lastly, the impact of data fusion on the system's performance was examined.

5.2 Evaluation Protocol

For all subjects, radiography of the calcaneus was obtained with a high-resolution Xray device with direct digitization (BMATM, D3A Medical Systems, Orleans, France) with a focal distance set at 1.15m and X-ray parameters set at 55kV and 20mA. The heel is scanned by the device using anatomical landmarks positioned by the operator on the image in order to correctly extract the Region of Interest (ROI) (400 × 400) pixels (1.6 × 1.6 cm^2) (Figure 5.1).

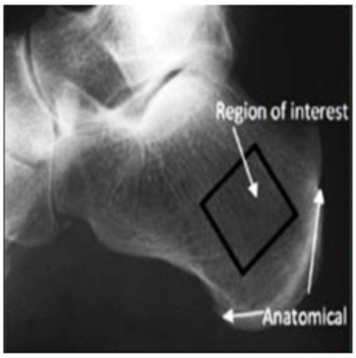

Figure 5.1: Region Of Interest (ROI).

The dataset used in this study consisted of 174 samples that were divided into three galleries, as shown in (Figure 5.2). The classifier was trained using the first and second galleries, The third gallery was utilized for blind classification evaluation purposes. A 10-fold cross-validation was performed to train the classifier using the 116-sample dataset, where the datasetwas randomly divided into 10 subsets, and we performed 10 rounds of training and testing. The best model was then selected once the classifier was trained and the ideal parameters for the proposed feature extraction method were identified, which was then used to classify the remaining 58 blind samples [113]. It was challenging to classify the images due to the high similarity between the classes, and it was difficult for a human observer to differentiate between healthy and osteoporotic images with the naked eye, as demonstrated in (Figure 5.2).

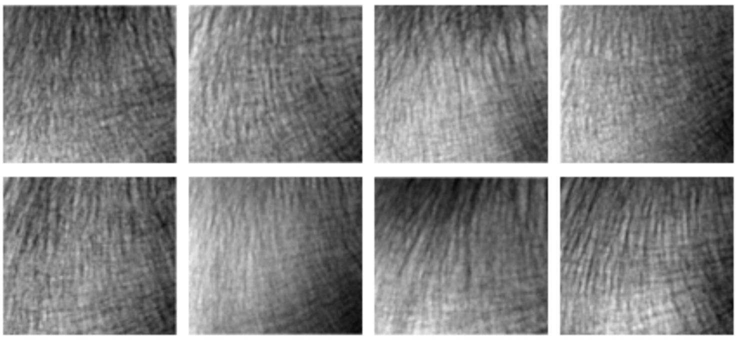

Figure 5.2: Osteoporosis comparison image between the healthy people from the first row, and the osteoporosis patients from the second row.

5.3 Impact of Filtring CLAHE image on model Performance

This section will provide a thorough evaluation of the proposed method, covering all steps from normalization to fusion, as well as the selection of The best settings for the Gabor filters were determined (optimal parameters)

5.3.1 Evaluation of the Proposed Methods

1. CLAHE-based Analysis markedly Improves Performance

Prior to performing feature extraction, the region of interest in the bone images undergoes a contrast enhancement step using the Contrast Limited Adaptive Histogram Equalization (CLAHE) method.

The tile sub-region (shown in Figure 5.3) is a crucial parameter in this method, and we will investigate three different tile sizes to determine which one results in the most enhanced image. We will incorporate the enhanced images into an osteoporosis diagnosis model that uses handcrafted feature extraction techniques (Filtering-free model) to accomplish this.

Our evaluation dataset consists of (400 × 400) pixel images, so we will explore tiles with medium-sized (20 × 20, 40 × 40 and 80 × 80) [113]. (Figure 5.4) depicts the results for the three examined sizes using the six handcrafted feature extraction techniques (HOG, Pyramid of Histogram of Oriented Gradients (PHOG), Local Binary Pattern (LBP), LPQ, Gradient Directional Pattern (GDP), Improved Weber Binary

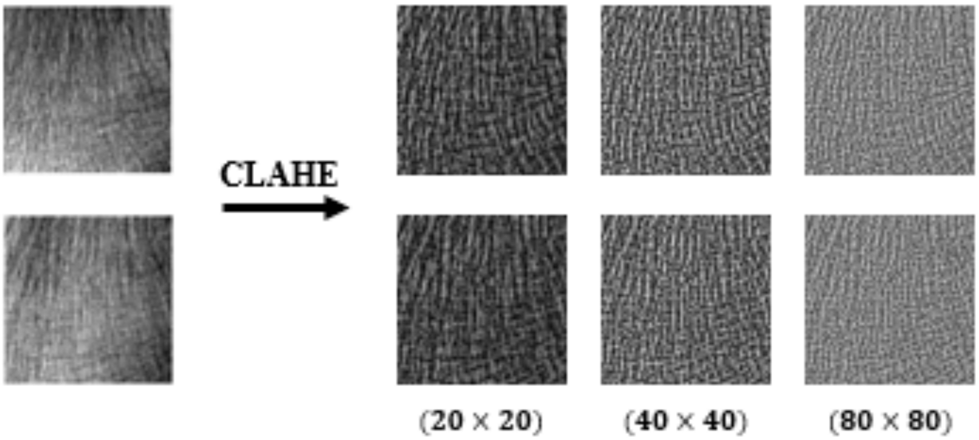

Figure 5.3: Osteoporosis comparison CLAHE image with different tile sizes between the healthy people from the first row, and the osteoporosis patients from the second row.

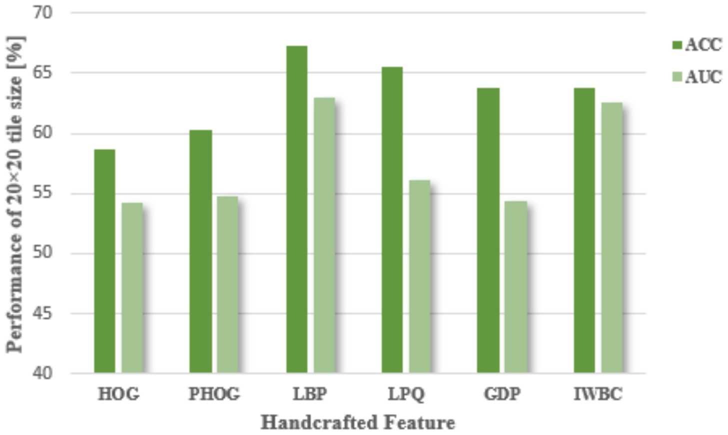

Figure 5.4: Performance comparison under the six Handcrafted Features with 20 × 20 CLAHE tile size.

Coding (IWBC)) in the case of 20 × 20 tile size.

In the (20 × 20) tiles size, (Figure 5.4) shows the performance of the LBP-based model in terms of the ACC and the AUC) reaches 67.24% and 63.02% at the decision threshold T_d^{LBP} equal to 1.0275, and a confusion matrix M_{conf}^{LBP} (FP, TP, TN, FN) = (7, 17, 22, 12) with a 5 features Number N_f^{LBP} and a λ_0^{LBP}= 0.35.

Similarly, the other handcrafted-based model works with an (ACC, AUC) equal to {(58.62%, 54.22%), (60.34%, 54.70%), (65.52%, 56.12%), (63.79%, 54.34%), (63.79%, 62.54%)} at the T_d equal to (-0.2854, -0.0047, -1.1210, -0.6814, 1.0928), and a confusion matrix of M_{conf} (FP, TP, TN, FN) = {(6, 11, 23, 18), (10, 16, 19, 13), (5, 14, 24, 15), (5, 13, 24, 16), (16, 24, 13, 5)} with (N_f, λ_0) = {(6, 0.65), (5, 0.45), (6, 0.50), (35, 0.80), (5, 0.90)} for the (HOG, PHOG, LPQ, GDP, and IWBC), respectively.

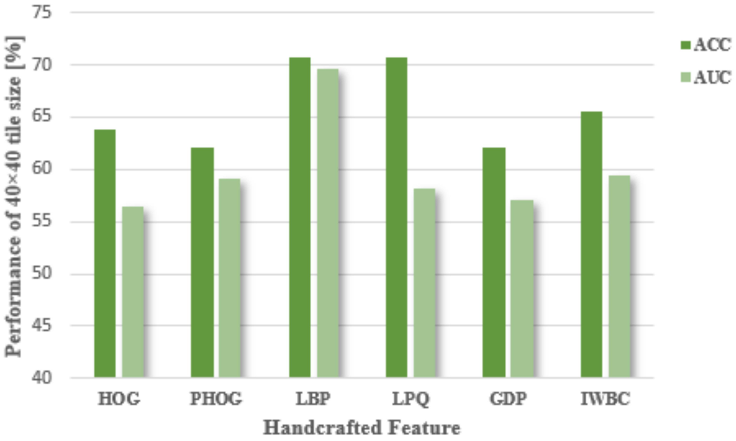

Figure 5.5: Performance comparison under the six Handcrafted Features with 40 × 40 CLAHE tile size.

The accuracy and AUC achieved by this model were 70.96% and 58.15%, respectively, at a decision threshold of T_d^{LPQ} equal to -0.3578. The corresponding confusion matrix was M_{conf}^{LPQ} = (10, 22, 19, 7), where FP, TP, TN, and FN denote true positive, false positive, true negative, and false negative, respectively. The LPQ-based model used 16 features (N_f^{LPQ}) and a regularization parameter of λ_0^{LPQ} equal to 1.00.

Similarly, the other handcrafted-based model works with an (ACC, AUC) of {(63.79%, 56.48%), (62.07%, 59.10%), (70.69%, 69.68%), (62.07%, 57.07%), (65.52%, 59.45%)} at the T_d equal to (-0.1358, 0.0003, 0.9627, -0.6772, -1.0945), and a confusion matrix of M_{conf} (FP, TP, TN, FN) = {(9, 17, 20, 12), (10, 17, 19, 12), (12, 24, 17, 5) , (11, 18, 18, 11) , (15, 24, 14, 5)} with (N_f, λ_0) = {(51, 0.90), (5, 0.65), (5, 0.25), (80, 0.85), (70, 0.75)} for the (HOG, PHOG, LBP, GDP, and IWBC), respectively.

(Figure 5.6) Shows the case of (80 × 80) tiles size, the performance of the LPQ-based model in terms of (ACC, AUC) is still the best one and reaches (68.97%, 64.68%) at -0.6025 of the decision threshold (T_d^{LPQ}), and a confusion matrix of M_{conf}^{LPQ} (FP, TP, TN, FN) = (9, 20, 20, 9) with a (N_f^{LPQ}=86 features and a λ_0^{LPQ}= 0.60).

Also, the other handcrafted-based model works with an (ACC, AUC) of {(60.34%, 48.99%), (60.34%, 55.29%), (65.52%, 61.59%), (62.07%, 65.99%), (68.97%, 62.07%)} at the T_d equal to (0.1340, -0.0413, -1.5100, 1.0429, -0.9061), and a confusion matrix of M_{conf} (FP, TP, TN, FN) = {(18, 24, 11, 5), (7, 13, 22, 16), (9, 18, 20, 11), (12, 19, 17, 10), (9, 20, 20, 9)} with (N_f, λ_0) = {(11, 0.80), (25, 0.90), (30, 0.35), (5, 0.95),

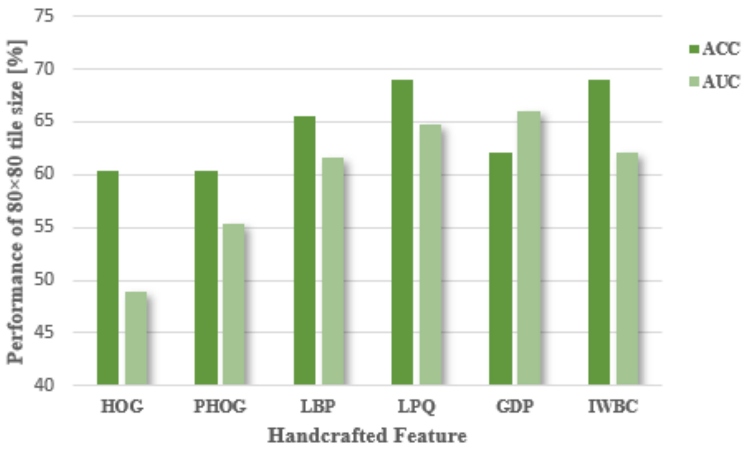

Figure 5.6: Performance comparison under the six Handcrafted Features with 80 × 80 CLAHE tile size.

(5, 0.20)} for the (HOG, PHOG, LBP, GDP, and IWBC), respectively.

Additionally, all six methods for feature extraction were utilized on the entire image. The accuracy (ACC) and area under the curve (AUC) of the system were graphed to demonstrate the results. Based on the various graphs presented, two key conclusions can be drawn:

- The LPQ technique proved to be more effective than the other methods in terms of ACC and AUC, irrespective of the tile size employed.
- In overall, the tile size of 40 × 40 displayed the greatest effectiveness, as depicted in (Figure 5.7).

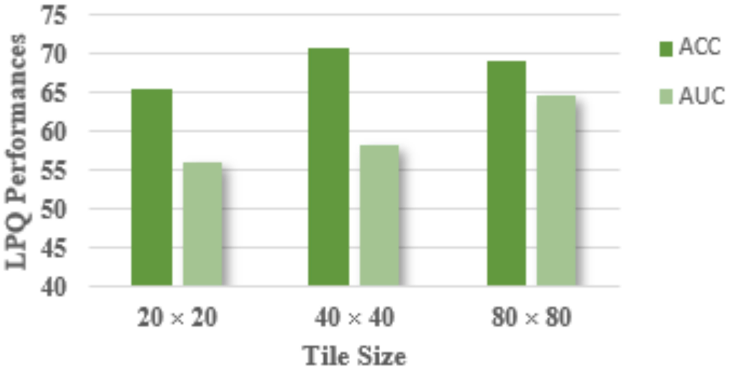

Figure 5.7: Performance comparison under numerous CLAHE tile sizes with the LPQ descriptor.

(Figure 5.7) shows that LPQ achieves a higher AUC with 80x80 tiles size compared to

40x40 tiles size. However, (Table 5.1) demonstrates that 40x40 tiles size have higher values for (SPE), (SEN), and F_1-score, which further highlights their superiority over larger tiles.

Table 5.1: Evaluation Results for Various Tile Sizes Using CLAHE Preprocessing

	(20×20)			(40×40)			(80×80)		
(%)	**SPE**	**SEN**	F_{1score}	**SPE**	**SEN**	F_{1score}	**SPE**	**SEN**	F_{1score}
HOG	37.93	79.31	65.71	58.62	68.97	65.57	82.76	37.93	48.89
PHOG	65.52	55.17	58.18	65.52	58.62	60.71	75.86	44.83	53.06
LBP	75.86	58.62	64.15	58.62	82.76	73.85	68.97	62.07	64.29
LPQ	48.28	82.77	70.59	75.86	65.52	69.09	68.97	68.97	68.97
GDP	82.76	44.83	55.32	62.07	62.07	62.07	58.62	65.52	63.33
IWBC	44.83	82.76	69.57	48.28	82.76	70.59	68.97	68.97	68.97

Based on the results presented in the table, it can be concluded that the LPQ model performs better with 40 × 40 sized tiles than with 80 × 80 sized tiles in terms of SPE and F_1-score. Hence, for image normalization, we will use tiles of size 40 × 40 in the subsequent experiments.

2. Block-based Analysis markedly Improves Performance

Over the last ten years, block-based image analysis has emerged as a dominant processing approach in numerous visual systems. This approach has found widespread application in image processing, particularly for tasks such as data compression and pattern recognition.

Block-based analysis involves partitioning an image into smaller sub-images or blocks. This approach is preferred in image processing due to the significant computational time and memory space required for processing the entire image. Instead, it is more practical to process multiple sets of reduced data obtained by dividing the image into smaller blocks.

In this section of the experiment, we aimed to evaluate the effectiveness of block-based image analysis in the osteoporosis diagnosis system. To achieve this, we followed a specific approach:

We divided the original images into blocks of different sizes ($S_{BLK} = \{$ 100 × 100, 200 × 200, 300 × 300$\}$) and applied four different Overlap (OLP) rates ($S_{OLP} = \{0\%, 25\%,$

50%, 75%}) to each block size. This allowed us to investigate the impact of block size and (OLP) rate on the performance of the system.

To determine the accuracy (ACC), the six handcrafted feature extraction methods were applied to the blocks. Each feature extraction method was tested 12 times, and the parameters that resulted in the highest ACC values were selected. System performance, as measured by ACC and area under the curve (AUC), was plotted for the six feature extraction methods as a function of block size and overlap.

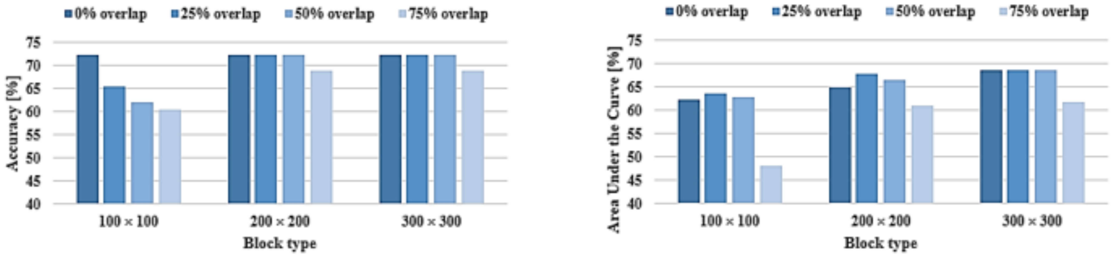

Figure 5.8: HOG-based Osteoporosis diagnostic system. Comparison of performance using a variety of analysis block sizes based on ACC (a), and AUC (b).

By observing and analyzing (Figure 5.8) Compared to the analysis of the entire image, the adoption of a block-based analysis in HOG led to a substantial improvement in system performance, with a 13.50% increase observed.

Table 5.2: Evaluating System Performance with Different Analysis Block Sizes.

Analysis	**HOG**								
Block type	T_d^{HOG}	SPE	SEN	ACC	AUC	F_{1score}	N_{feat}	λ_0	O
100 × 100	-0.1390	51.72	93.10	72.41	62.19	77.14	11	1	0
200 × 200	-0.2484	58.62	86.21	72.41	64.80	75.76	16	0.55	0
300 × 300	0.0538	72.41	72.41	72.41	68.61	72.41	61	1	0
400 × 400	-0.1358	58.62	68.97	63.79	56.48	65.57	51	0.90	/

Under optimal conditions (100 × 100 and 0% overlap), the system can operate with (AUC, ACC) values of (62.19% , 72.41%) at T_d^{HOG}= - 0.1390 and a confusion matrix of M_{conf}^{HOG} = (2, 15 , 27, 14) with (λ_0^{HOG}, N_f^{HOG}) values of (1.00 , 11). (Table 5.2) presents further outcomes of the block-based image analysis.

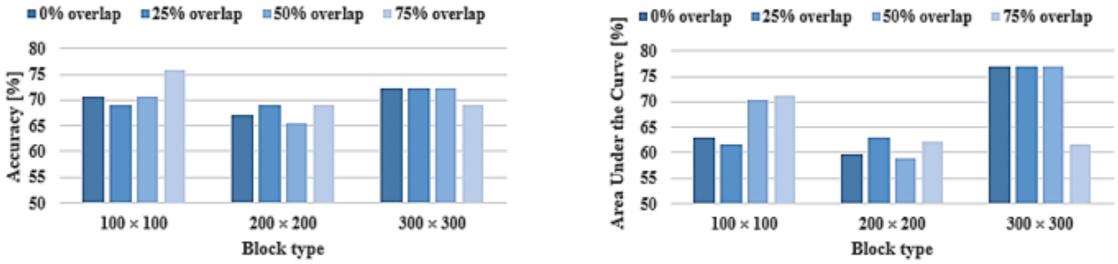

Figure 5.9: Analyzing the Performance of LPQ-Based Osteoporosis Diagnostic Systems Using Different Analysis Block Sizes: Comparison Based on ACC (a) and AUC (b)

As a result, the proposed system was able to achieve (ACC, AUC) values of (75.86%, 71.34%) by using a block size of (100 x 100) and a 75% overlap in LPQ analysis, resulting in an improvement in ACC of approximately 7.32%, at $T_d^{LPQ} = 0.4441$ and a confusion matrix of $M_{conf}^{LPQ} = (9, 24, 20, 5)$ with (N_f^{LPQ}, λ_0^{LPQ}) values of (41, 0.75). (Table 5.3) presents further outcomes of block-based image analysis. The results presented in Figure 5.9 demonstrate that using a block size of 100 × 100 with a 75% overlap still produces the best performance, even with the LPQ feature extraction technique. This configuration leads to an improvement in ACC of approximately 7.32%. With this setting, the system can achieve an ACC and AUC of 75.86% and 71.34%, respectively, at the decision threshold T_d^{LPQ} of 0.4441. The corresponding confusion matrix is $M_{conf}^{LPQ} =$ (9 , 24, 20, 5), and the values of N_f^{LPQ} and λ_0^{LPQ} are 41 and 0.75, respectively. (Table 5.3) presents additional results of block-based image analysis.

Table 5.3: Comparison of performance using different block sizes for image analysis.

Analysis	**LPQ**								
Block type	T_d^{HOG}	SPE	SEN	ACC	AUC	F_{1score}	N_{feat}	λ_0	O
100 × 100	0.4441	82.76	68.97	75.86	71.34	74.07	41	0.75	75
200 × 200	-0.2897	72.41	65.52	68.97	63.02	67.86	66	0.20	25
300 × 300	-0.7760	79.31	65.52	72.41	77.05	70.37	41	0.80	0
400 × 400	-0.3578	75.86	65.52	70.69	58.15	69.09	16	1	/

In contrast to the HOG and LPQ methods, the remaining handcrafted feature extraction methods did not yield satisfactory results or provide a significant improvement. (Table 5.4) displays the best-case outcomes for the PHOG, LBP, GDP, and IWBC descriptors.

Table 5.4: Performance for different analysis block sizes.

Block	**100 × 100**			**200 × 200**			**300 × 300**		
Methods	SPE	SEN	ACC	SPE	SEN	ACC	SPE	SEN	ACC
PHOG	41.38	82.76	62.07	55.17	68.97	62.07	44.83	79.31	62.07
LBP	72.41	58.62	65.52	62.07	75.86	68.97	62.07	68.97	65.52
GDP	75.86	58.62	67.24	55.17	75.86	65.52	51.72	79.31	65.52
IWBC	48.28	75.86	62.07	75.86	55.17	65.52	65.52	65.52	65.52

By observing and analyzing (Table 5.4), we find the best-case scenario in the case of LBP (200 × 200 and 50% overlap), we can see that the block-based analysis increased system performance just with 1.73% improvement, compared to the whole image analysis. As for the PHOG and the IWBC, we found that it was not affected in terms of Accuracy by this analysis. In the case of the GDP (100 × 100 and 75% overlap), the block-based analysis improves the system by 5.17%. However, these improvements are very small compared to what we have obtained in (Table 5.2) and (Table 5.3).

The system can operate with (AUC, ACC) values of (67.90% , 68.97%), (61.24% , 67.24%), (61.71% , 65.52%), (57.19% , 62.07%) in the case of LBP, GDP, IWBC, and PHOG. The results presented in (Table 5.4) emphasize the importance of using the HOG and LPQ methods in block-based image analysis due to their effectiveness and potential for enhancing research outcomes. As a result of this analysis, it is recommended to use a block size of 100 × 100 for future experiments.

Initial tests were performed without the filter layer, referred to as "Filtering-free", using CLAHE tiles of size 40 × 40 and analysis blocks of size 100 × 100. The subsequent experiments aimed to evaluate the impact of the filtering layer on system performance.

5.3.2 Enhancing Performance Through Input Image Filtering

Following normalization of the image with a pre-determined CLAHE tile, each block measuring 100 × 100 is filtered using a set of Gabor filters to generate multiple descriptors. These descriptors are then combined and passed through a HOG/LPQ algorithm. The resulting vectors are concatenated to form a feature vector, with the HOG method operating on 3 × 3 cells and producing a 9-bin histogram, while the LPQ algorithm employs a window size of 15 × 15. The blocks were analyzed using N Gabor filters, where N ranges from 2 to 8, and three different filter sizes $(k_1 \times k_2) \equiv \{(3 \times 3),(5 \times 5),(7 \times 7)\}$. It is worth mentioning that the initial values of f_0, γ, and η for the Gabor (GBR) filters were chosen randomly. Moreover, to reduce the number of tests, only the first scale of the Gabor filter bank was utilized.

1. Diagnosis System for Osteoporosis Using GBR-HOG Technology

In the Gabor-HOG (GBR-HOG)-based system, the parameters f_0, γ, and η were assigned random values of 0.637, 0.921, and 0.834, respectively. Varying the number/size of the Gabor filter (N and $k_1 \times k_2$) produces different feature representations, so we can experimentally select a combination of (N, $k_1 \times k_2$) that improves the system's accuracy. (Figure 5.10) illustrates the effect of the number of filters (N) on the ACC results for all filter sizes ($k_1 \times k_2$). This investigation was carried out to analyze the impact of these parameters, as the initial values of f_0, γ, and η for the GBR filters were chosen randomly, and only the first scale of the Gabor filter bank was employed to limit the number of tests.

The results shown in (Figure 5.10) indicate that smaller filter sizes yield better performance when the number of filters is high, while larger filter sizes perform better when the number of filters is low. (Table 5.5) provides a summary of the improvements observed.

The Gabor-HOG (GBR-HOG) based system achieved the highest ACC with either $N = 2$ and ($W = 7 \times 7$) sized filters with orientations of $\theta = 90° \pm 101.25°$ or with $N = 7$ and ($W = 3 \times 3$) sized filters with orientations of $\theta = 90° \pm 101.25° j \mid_{j=0..3}, 135°$. Among these configurations, the optimal one in terms of processing time is using two (7×7) sized filters, which produced a confusion matrix of $M_{conf}^{GBR-HOG} = (6, 22, 23, 7)$ and ($N_f^{GBR-HOG}$, $\lambda_0^{GBR-HOG}$) values of (15, 0.25). It is worth noting that the filtering layer significantly improved the system's performance by 7.15% compared to the filtering-free configuration. To understand the effect of these parameters, (Figure 5.10) illustrates the ACC outcomes in terms of the number of filters (N) used for each filter size ($k_1 \times k_2$).

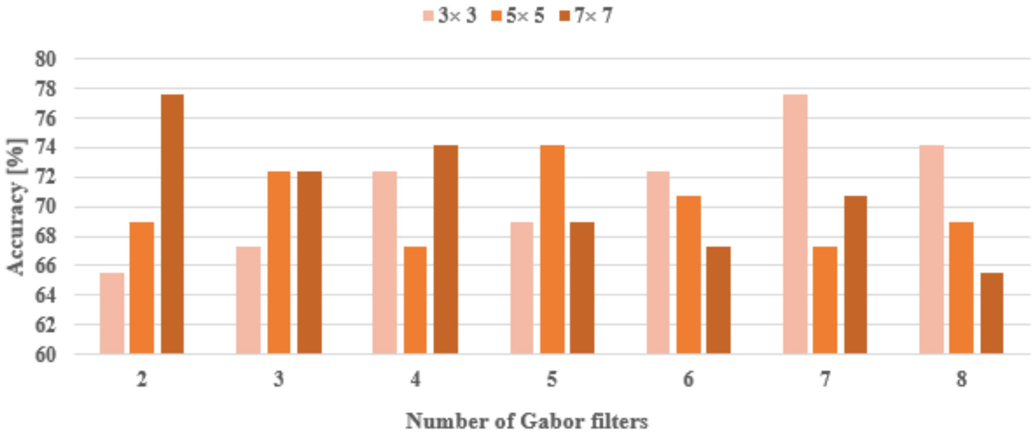

Figure 5.10: Evaluating the Performance of HOG-Based Systems with Different Gabor Filter Numbers and Sizes Based on ACC.

Table 5.5: Improvement of HOG-based system ACC with different Gabor filter sizes and numbers.

Analysis	**GBR-HOG**								
Filter Size	T_d^{HOG}	SPE[%]	SEN[%]	ACC[%]	AUC[%]	F_{1score}	N_{feat}	λ_0	N
3 × 3	0.0493	75.86	79.31	77.59	71.22	77.97	15	0.25	7
5 × 5	0.0195	65.52	82.76	74.14	69.08	76.19	43	0.10	5
7 × 7	-0.1131	79.31	75.86	77.59	73.48	77.19	37	0.55	2
without flt	-0.1390	51.72	93.10	72.41	62.19	77.14	11	1.00	/

2. Diagnosis System for Osteoporosis Using GBR-LPQ Technology

Likewise, for the Gabor-LPQ (GBR-LPQ)-based system, the parameters f_0, η , and γ were randomly assigned values of 0.898, 0.334 and 0.700, respectively. The impact of varying the number of filters (N) and their sizes ($k_1 \times k_2$) on the system's accuracy was analyzed, and the results are presented in (Figure 5.11).

This figure demonstrates that the system's performance significantly improved (by over 75%) when a Gabor filter of size ($W = 3 \times 3$) was used. Moreover, the best case results are summarized in (Table 5.6).

It is clear from the results that using N=8 filters improved the system performance by 2.28% in terms of ACC. With this configuration, the system achieved an ACC of 77.59% and an AUC of 74.67%. The resulting confusion matrix is $M_{conf}^{GBR-LPQ} = (7, 23, 22, 6)$, while the values of ($\lambda_0^{GBR-LPQ}$,$N_f^{GBR-LPQ}$) are (0.70 , 11).

The results presented in this section are specific to certain values of the Gabor filter's

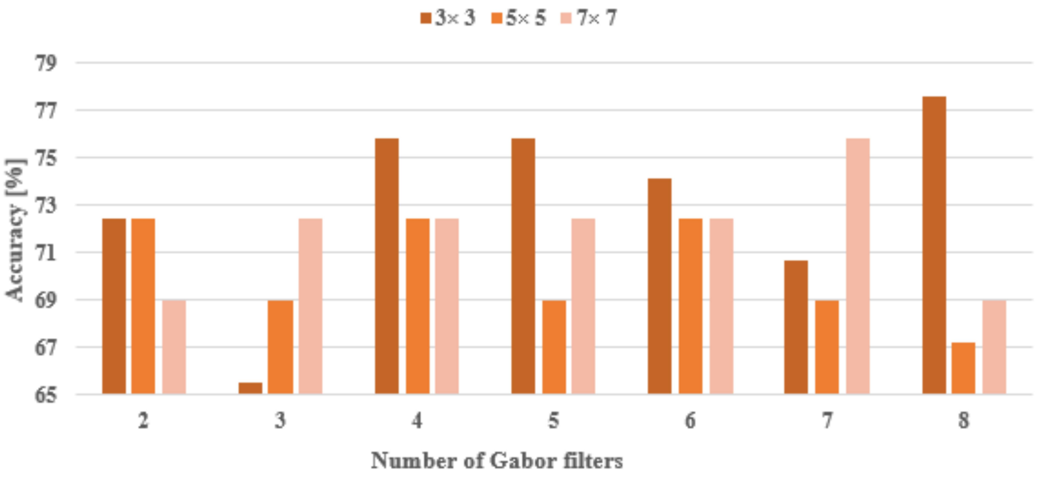

Figure 5.11: Comparison of Gabor filter number and size on ACC performance for LPG-based system.

parameters (f_0, γ, and η), indicating that modifying these parameter values could potentially lead to improved results. (Table 5.7) provides a summary of the overall results for the best case achieved.

Table 5.6: Comparison of ACC improvement in LPQ-based system using different Gabor filter numbers and sizes.

Analysis	**GBR-LPQ**								
Filter Size	T_d^{HOG}	SPE[%]	SEN[%]	ACC[%]	AUC[%]	F_{1score}	N_{feat}	λ_0	N
3 × 3	-1.0054	79.31	75.86	77.59	74.67	77.19	11	0.70	8
5 × 5	0.5814	75.86	68.97	72.41	74.32	71.43	45	0.65	6
7 × 7	-0.5829	68.97	82.76	75.86	72.53	77.42	11	0.70	7
without flt	0.4441	82.76	68.97	75.86	71.34	74.07	41	0.75	/

Table 5.7: Performance comparison of GBR-HOG and GBR-LPQ systems using an effective configuration with a Gabor filter size of $w = (3 \times 3)$

Methods	T_d^{HOG}	SPE	SEN	ACC	AUC	F_{1score}	N_{feat}	λ_0	N
GBR-HOG	0.0493	75.86	79.31	77.59	71.22	77.97	15	0.25	7
GBR-LPQ	-1.0054	79.31	75.86	77.59	74.67	77.19	11	0.70	8

To illustrate the significance of incorporating the filtering layer, (Figure 5.12) compares the best results obtained with and without the filtering layer (filtering-free).

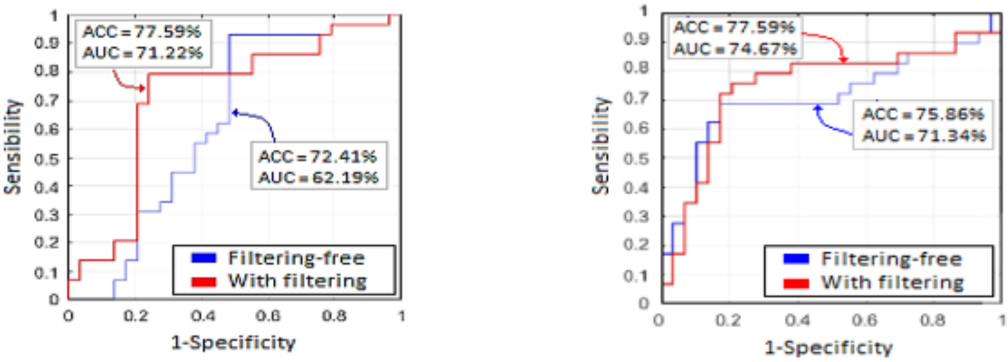

Figure 5.12: Comparing the Performance of Osteoporosis Diagnosis Systems with and without Filtering: HOG and GBR-HOG on the Left, LPQ and GBR-LPQ on the Right.

The addition of the filtering layer resulted in a significant improvement in system performance, and the ACC exceeded 77%, as shown in Figure 5.12. This demonstrates the importance of incorporating the filtering layer in the system. The HOG and LPQ techniques have several parameters that can be fine-tuned to further improve the performance of the Osteoporosis diagnosis system. For example, the number of bins in the HOG histogram or the size of the LPQ window can be adjusted to optimize the feature extraction process. Additionally, other image processing techniques, such as wavelet transforms or deep learning, can also be explored to improve the accuracy of the system.

5.4 The Effect of Optimizers on Model Performance

In earlier trials, the HOG and LPQ feature extraction techniques randomly chose the Gabor parameters, which consist of the digital frequency (f_0) and the two normalized scales (γ, η). In this section, we aim to determine the ideal values for these parameters that produce the best results. Unlike previous optimization efforts that were limited to the best settings identified earlier, we will consider all available configurations, including values from 2 to 8 for n and the three filter sizes used previously. The search range for these parameters is limited to a value between 0 and 1. The outcomes of the optimization algorithm are presented in (Table 5.8), which displays the optimal results.

Table 5.8 indicates that the optimization process has enhanced the system's perfor-

Table 5.8: Evaluating System Performance with Optimal Gabor Filter Settings ($w = (3 \times 3)$)

Methods	T_d^{HOG}	SPE	SEN	ACC	AUC	F_{1score}	N_{feat}	λ_0	N
GBR-HOG	0.1565	86.21	75.86	81.03	80.86	80.00	61	0.30	2
GBR-LPQ	0.3775	93.10	65.52	79.31	75.86	76.00	46	0.10	2

mance by 4.45% and 2.22% for GBR-HOG and GBR-LPQ, respectively, compared to the previous results. It is evident that the most favorable outcomes were obtained when using two Gabor filters with a size of $W = 3 \times 3$ for both methods. For the optimal parameters of the Gabor filter (0.730, 0.801, 0.619), in the case of GBR-HOG, the system works with values (AUC, ACC) of (80.86%, 81.03%) at $T_d^{GBR-HOG} = 0.1565$ and a confusion matrix of $M_{conf}^{GBR-HOG} = (7, 25, 22, 4)$, with $(\lambda_0^{GBR-HOG}, N_f^{GBR-HOG})$ values of (0.30, 61). The GBR-LPQ feature extraction method achieved optimal parameters for the Gabor filter of (0.880, 0.701, 0.719), resulting in a system that can operate with (AUC, ACC) values of (75.86%, 79.31%). at $T_d^{GBR-LPQ} = -0.3775$ and a confusion matrix of $M_{conf}^{GBR-LPQ}$= (10, 27, 19, 2), with $(\lambda_0^{GBR-LPQ}, N_f^{GBR-LPQ})$ values of (0.10, 46),To underscore the significance of the optimization procedure, (Figure 5.13) presents a comparison between the optimal outcomes and those attained without optimization.

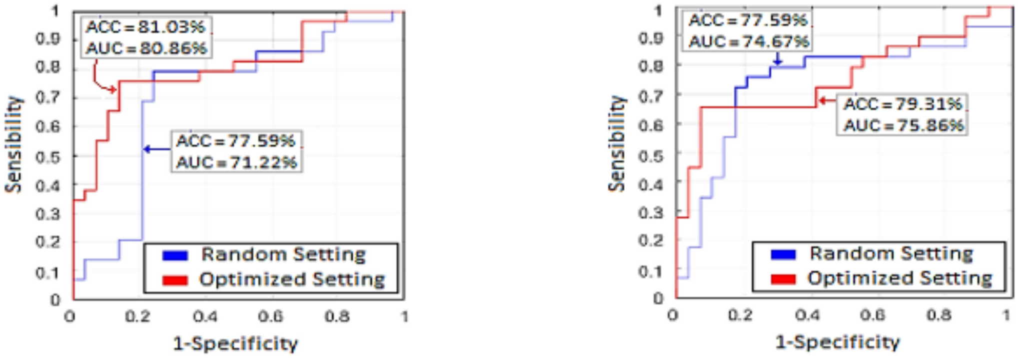

Figure 5.13: Comparison of performance between optimized and non-optimized systems for Osteoporosis diagnosis using HOG and GBR-HOG-based systems on the left and LPQ and GBR-LPQ-based systems on the right.

These two figures displays the influence of the optimization procedure on the system's performance. It's important to note that other optimization algorithms like Genetic Algorithm (GA) or Particle Swarm Optimization (PSO) can be implemented to search a broader range and enhance the Gabor filter parameters.

5.5 Data Fusion's Influence on Model Performance

A diagnostic system that relies on a single source of information cannot guarantee accurate diagnosis, as the associated error rates are significant, rendering the system's decisions unreliable. To address this limitation, multi-source diagnostic systems that integrate information from various sources in the input image can be developed. In this section, we aim to investigate whether combining several pieces of information derived from the bone sub-image can enhance the system's performance.

Pattern recognition systems have the potential to improve their efficiency by integrating multiple sources of information. The data fusion principle is a technique that enables the processing of information from several sources by combining the data to obtain a more accurate decision than that obtained from each source individually. Typically, data fusion involves integrating multiple data to extract new information that is more representative of all the data.

Our study utilized a multi-algorithm approach, where the bone image was analyzed independently using both HOG and LPQ algorithms. The resulting information from both algorithms was fused together to improve system performance. In this approach, the fusion process can be integrated at three different levels, namely Feature Level, Matching Score Level, or Decision Level.

By utilizing all the available configurations, multiple single-source subsystems can be developed. However, in our experiment, we will restrict our focusTo select the optimal configuration for the GBR-HOG and GBR-LPQ-based feature extraction methods, the optimal parameters obtained for all filter sizes can be used. To determine which fusion technique produces the highest ACC, we conducted an experiment using three fusion levels.

5.5.1 Feature Level

At the feature-level fusion, multiple feature vectors (observations) derived from the feature extraction step are combined. Several techniques have been described in the literature for implementing feature-level fusion. In our study, we employed four different techniques for feature-level fusion, namely Average (AVR), Concatenation (CAT), Canonical Correlation Analysis (CCA), and Discriminant Correlation Analysis (DCA) [110].

1. Average (AVR)

$$\mathcal{V}_{FUS} = \frac{1}{2}(\mathcal{V}_{HOG} + \mathcal{V}_{LPQ}) \tag{5.1}$$

2. Concatenation (CAT)

$$\mathcal{V}_{FUS} = (\mathcal{V}_{HOG}, \mathcal{V}_{LPQ}) \tag{5.2}$$

In the two previous cases it is necessary that $\mathcal{V}_{HOG}$ and $\mathcal{V}_{LPQ}$ must be the same length.

3. Canonical Correlation Analysis (CCA)

CCA is a technique for feature-level fusion where the transformed feature vectors are combined either by concatenation or by summation:

$$\mathcal{V}_{FUS} = \mathcal{W}_{HOG}^{T} \cdot \mathcal{V}_{HOG} + \mathcal{W}_{LPQ}^{T} \cdot \mathcal{V}_{LPQ} \tag{5.3}$$

or:

$$\mathcal{V}_{FUS} = \mathcal{W}_{HOG}^{T} \cdot \mathcal{V}_{HOG}, \mathcal{W}_{LPQ}^{T} \cdot \mathcal{V}_{LPQ} \tag{5.4}$$

Where $\mathcal{W}_{HOG}^{T}$ and $\mathcal{W}_{LPQ}^{T}$ denote the transformation matrices (see Appendix D for more details).

4. Discriminant Correlation Analysis (DCA)

Similar to the Canonical Correlation Analysis (CCA) methodology, the details of the CCA and DCA methods are in the appendix D.

Based on the results shown in (Table 5.9), we can observe that the fusion at the feature level method is insufficient, as all the techniques used do not yield satisfactory classification rates and lead to a degradation of performance compared to classification without data fusion. Therefore, it is necessary to eliminate this method in our work.

Table 5.9: Fusion at Feature Level Osteoporosis diagnosis system performance.

	3 × 3	5 × 5	7 ×7	Rule	SPE[%]	SEN	ACC	AUC	F_{1score}
HOG$_{FUS}$	√		√	**CCA**	75.86	72.41	74.14	66.83	73.68
		√	√	**CAT**	72.41	72.41	72.41	73.01	72.41
	√		√	**AVR**	72.14	72.41	72.41	69.80	72.41
GBR-HOG	√			/	86.21	75.86	81.03	80.86	80.00
LPQ$_{FUS}$	√		√	**CAT**	75.86	65.52	70.69	68.85	69.09
		√	√	**AVR**	68.97	72.41	70.69	70.63	71.19
	√		√	**DCA**	79.31	58.62	68.97	63.50	65.38
GBR-LPQ	√			/	93.10	65.52	79.31	75.86	76.00
FUS$^{HOG}_{LPQ}$	√			**CCA**	79.31	65.52	72.41	65.99	70.37
	√			**DCA**	79.31	60.07	75.00	65.87	67.92
		√		**DCA**	55.17	86.21	70.69	58.86	74.63

5.5.2 Matching Score Level

At the final stage, the individual scores are integrated to form a single score, which is used to make the ultimate decision. The most widely used method of fusion is score-level fusion, which employs simple and effective techniques and can be applied to all types of systems. Various fusion rules, including the Sum of the Scores (SUM), the Minimum of the Scores (MIN), the Maximum of the scores (MAX), and the Product of the Scores (MUL) rules [113], are available for combining scores [09].

Assuming that the classification subsystems are denoted as S_{HOG} and S_{LPQ} and their matching scores are represented as d_{HOG} and d_{LPQ}, the fused score (d_{FUS}) is obtained through the following computation:

1. **Sum of the Score (SUM)**

$$d_{FUS} = d_{HOG} + d_{LPQ} \tag{5.5}$$

2. **Minimum of the Score (MIN)**

$$d_{FUS} = min(d_{HOG}, d_{LPQ}) \tag{5.6}$$

3. **Maximum of the Score (MAX)**

$$d_{FUS} = max(d_{HOG}, d_{LPQ}) \tag{5.7}$$

4. Product of the Score (MUL)

$$d_{FUS} = d_{HOG} \cdot d_{LPQ} \tag{5.8}$$

It is crucial to highlight that the fusion rules can be employed only when the scores from all subsystems have the same characteristics. Hence, it is necessary to perform an initial step of score normalization before applying the combination rules.

Table 5.10: Fusion at Matching Score Level Osteoporosis diagnosis system performance.

	3 × 3	5 × 5	7 ×7	Rule	SPE	SEN	ACC	AUC	F_{1score}
HOG$_{FUS}$	√	√		**MIN**	82.76	72.41	77.59	78.48	76.36
	√		√	**SUM**	79.31	79.31	79.31	78.24	79.31
		√	√	**SUM**	72.41	82.76	77.59	78.69	78.69
GBR-HOG	√			/	86.21	75.86	81.03	80.86	80.00
LPQ$_{FUS}$	√	√		**MIN**	86.21	68.97	77.59	77.29	75.47
	√		√	**MAX**	68.97	82.76	75.86	73.01	77.42
		√	√	**SUM**	75.86	75.86	75.86	75.03	75.86
GBR-LPQ	√			/	93.10	65.52	79.31	75.86	76.00
FUS$^{HOG}_{LPQ}$	√			**SUM**	72.41	82.76	77.59	74.91	78.69
		√		**SUM**	82.76	72.41	77.59	75.98	76.36
			√	**MAX**	75.86	75.86	75.86	79.79	75.86

As observed from (Table 5.10), our results show that the Fusion at Feature Level method has a lower performance compared to our proposed approach. However, it is worth mentioning that the Precision of the classifier without data fusion is still superior. Therefore, the Fusion at Matching Score Level approach was also excluded as it did not contribute to the enhancement of the classifier's performance.

5.5.3 Deciding at the System Level

At this stage, the decisions made by the subsystems are integrated into a single decision. Each subsystem produces a binary decision in the form of "true" or "false", and the decision fusion process involves arriving at a final decision based on these outcomes. The most straightforward approaches for combining these decisions are based on AND, OR, and majority voting (VOTE) principles [113].

Suppose that $S_i^{HOG} \mid i = 1^N$ is a set of N HOG-based classification subsystems that utilize N distinct filter sizes, and let di^{HOG} denote the decision provided by each classification subsystem. The fused decision d_{FUS}^{HOG} is obtained using the following computation:

1. AND Rule

$$d_{FUS}^{HOG} = \&_{i=1}^{N} d_i^{HOG} = d_1^{HOG} \; \& \; d_2^{HOG} \; \& \; ... \; \& \; d_N^{HOG} \tag{5.9}$$

2. OR Rule

$$d_{FUS}^{HOG} = \|_{i=1}^{N} \; d_i^{HOG} = d_1^{HOG} \; \| \; d_2^{HOG} \; \| \; ... \; \| \; d_N^{HOG} \tag{5.10}$$

3. VOTE Rule

$$d_{FUS}^{HOG} = \begin{cases} 1 & if \quad N_{true} \geq [\frac{N}{2}] \\ 0 & otherwise \end{cases} \tag{5.11}$$

Here, N_{true} represents the number of classification subsystems that have made a decision of 1 ("true"), and the symbol $[\alpha]$ denotes the smallest integer greater than or equal to α (refer to Table 5.11).

Table 5.11: Fusion at Decision Level Osteoporosis diagnosis system performance.

	3 × 3	5 × 5	7 ×7	Rule	SPE[%]	SEN[%]	ACC[%]	F_{1score}
HOG$_{FUS}$	√	√	√	**VOTE**	88.46	81.25	84.48	85.25
GBR-HOG	√			/	86.21	75.86	81.03	80.00
LPQ$_{FUS}$	√	√	√	**VOTE**	92.59	87.10	89.66	90.00
GBR-LPQ	√			/	93.10	65.52	79.31	76.00
FUS$_{LPQ}^{HOG}$	√			**OR**	95.00	73.68	81.04	83.58
		√		**AND**	68.42	85.00	74.18	69.39
			√	**OR**	100.00	69.05	77.59	81.69

The results presented in the table demonstrate that the diagnostic system for osteoporosis only showed a significant improvement in performance with decision-level fusion. Specifically, utilizing the VOTE rule to fuse the information acquired by examining the image using all filter sizes in accordance with LPQ resulted in a substantial increase in system performance. The system achieved an accuracy of 89.66%, which is a substantial improvement of 26.85% compared to the original system. By using the same decision thresholds ($T_d^{GBR-LPQ}$) and the same number of selected features ($N_f^{GBR-LPQ}$), the three fused subsystems produced a confusion matrix M_{conf}^{FUS} with values (2, 25, 27, 4). However, at the score-fusion level, the osteoporosis diagnostic system can either maintain its performance level or experience degradation compared to the uni-source system.

5.6 Discussion

This section intends to present and discuss the significant results obtained from the study and provide recommendations based on the findings. Additionally, a comparative analysis will be presented with previous research in the field.

The purpose of this work is to examine how texture analysis can be used to distinguish between healthy and osteoporotic bones. The findings suggest that the direct application of handcrafted feature extraction methods on bone images fails to produce satisfactory outcomes compared to utilizing these techniques on descriptors obtained through deep image analysis. The contrast between the two approaches is demonstrated in (Figure 5.14).

The depicted figure allows us to infer that:

- The analysis indicates that bone deterioration might be concentrated in a specific area of the examined region. As a result, Performing a block-by-block analysis of bone images is recommended to minimize the inter-correlation ratio between healthy and diseased bone images. This approach can decrease the interdependence among a significant portion of the vector coefficients.

- The filtering process aims to remove any extraneous characteristics, leaving only the essential traits in the image. To extract the features of the bone image effectively, it is crucial to apply filters that enhance the contrast of the image lines, which are the most important traits.

- The integration of the feature extraction method with the classifier is critical since the classifier functions as an expert that can optimize the performance of the feature extraction method by selecting its parameters, which is commonly referred to as deep behavior.

- Due to the high correlation between healthy and diseased bone images, combining multiple analysis techniques and integrating their results can enhance the system's performance. This is because each analysis process provides additional data that can contribute to a more comprehensive understanding of the image.

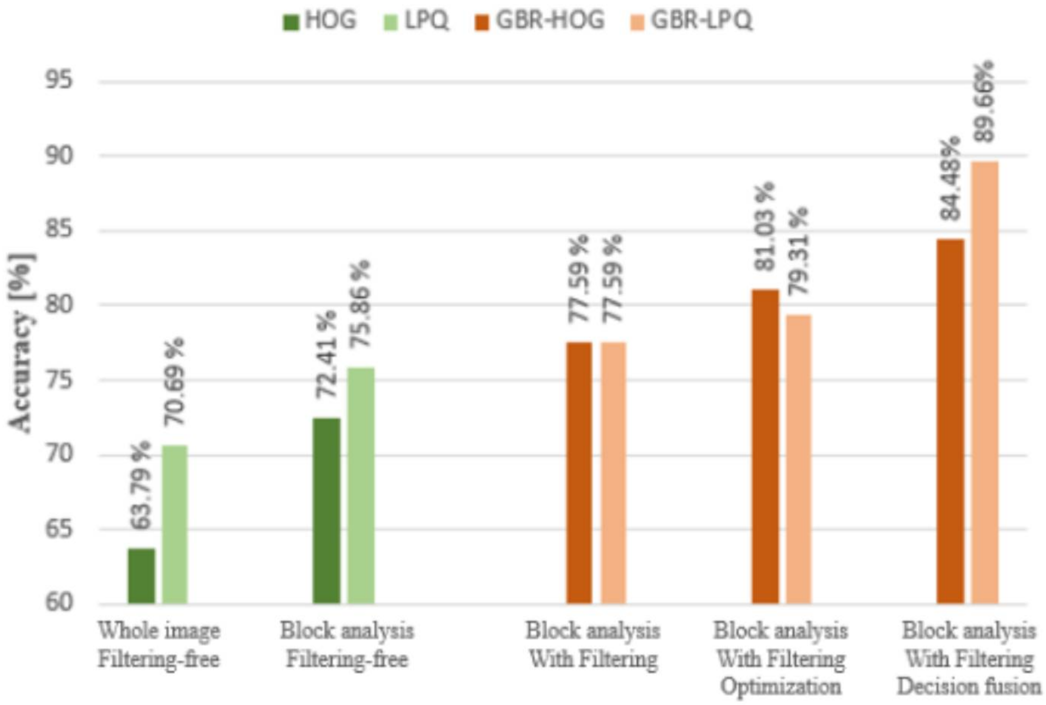

Figure 5.14: Progress in Enhancing System Performance: Achieving the Most Noteworthy Results.

It is important to note that there is still considerable room for improvement in the performance of this system. One approach to achieve this is through the adoption of techniques such as feature-level fusion and pyramid analysis. These methods can enhance the system's ability to extract and analyze image features, leading to improved performance.

When developing pattern recognition systems, it is crucial to compare the results with those obtained in prior research. To ensure a fair comparison, only studies that used the same dataset and evaluation protocol should be considered. In this study, we demonstrate the effectiveness of our proposed method in comparison to existing approaches (including handcrafted and deep learning-based methods) by conducting a comparative analysis using the dataset provided by IEEE-ISBI Challenge. (Table 5.12) summarizes the key findings from previous research.

The findings presented in (Table 5.12) highlight the effectiveness of our proposed osteoporosis diagnostic system. Whether based on a single source or multi-sources, our system consistently outperforms all other methods listed in terms of accuracy (up to 89.66%) and area under the curve (AUC) (up to 80.86%). These results demonstrate the potential of our system for use in Computer-Aided Diagnosis (CAD) of osteoporosis.

Table 5.12: Comparative Performance Analysis with State-of-the-Art Works

Authors	Methods	Classifier	ACC	SEN	SPE	AUC	F_{1score}
Yang et al [105]	SIFT-IFV	SVM	68.00	72.00	66.00	68.00	63.90
	LBP-IFV		68.50	70.00	64.00	64.00	68.40
Florian Yger [106]	Haar	SVM	64.00	62.00	66.00	-	63.90
Su et al [107]	AlexNet+ECD	SVM	77.50	74.70	83.30	82.10	76.40
Su et al [108]	FS	SVM	71.20	73.30	69.00	-	71.00
Palanivel et al [109]	LH	SVM	59.00	59.00	59.00	-	-
Proposed	Gabor-HOG	SVM	81.03	75.86	86.21	80.86	80.00
	Gabor-LPQ		79.31	65.52	93.10	75.86	76.00
	HOG-FUS		84.48	81.25	88.46	-	85.25
	LPQ-FUS		89.66	87.10	92.59	-	90.00

5.7 Conclusion

Osteoporosis diagnosis is a critical medical imaging application, and this chapter presents an AI-based technique for automating the detection of this condition using X-ray images of bone tissue. One of the key aspects of our proposed model for diagnosing osteoporosis is the use of handcrafted features. These features are derived from descriptors obtained through an extensive analysis of the bone image using a set of Gabor filters with varying orientations. To extract these features, we utilized several well-established handcrafted methods. To achieve high-performance levels, we utilized the BAT Algorithm optimization method to determine the optimal parameters for the Gabor filters. Furthermore, we combined information from three distinct levels: Feature, Score, and Decision levels. Our study covers all aspects of system development, Several decisions and choices were made in the development of the proposed osteoporosis diagnosis model, including selecting the optimal normalization approach, determining whether to analyze the entire bone image or divide it into blocks, selecting the best Gabor filter parameters, and integrating information from multiple subsystems to enhance system performance. Through rigorous testing, our proposed system achieved excellent performance (with accuracy up to 89.66%), surpassing several previously published studies.

Chapter 6

General Conclusion

The growing demand for radiologists can be attributed to the rapid advancements in Medical Imaging technology. This has resulted in an increased workload for radiologists, which unfortunately can lead to diagnostic errors. To address this issue, Artificial Intelligence (AI) approaches have been applied to medical imaging to improve diagnostic Accuracy and bridge the gap between inexperienced and experienced clinicians or generalists and specialists [6]. One essential diagnostic practice requiring medical imaging is the diagnosis of Osteoporosis. This thesis introduces an AI-based technique that utilizes X-ray images of bone tissue for the automatic detection of osteoporosis [13].

The present study involves the creation of a diagnostic model for osteoporosis using handcrafted features extracted from bone images. To obtain these features, we analyzed the images using a set of Gabor filters with different orientations and used two well-known methods, HOG and LPQ, to extract descriptor features. We optimized the Gabor filter parameters using a bat-based optimization method to achieve high performance. Additionally, we fused information at both the score level and decision level. Our study covered all aspects of system development, including selecting the optimal normalization approach, analyzing the full image or blocks, selecting Gabor filter parameters, and combining information from various subsystems. Our model demonstrated exceptional performance (89.66% Accuracy), surpassing several previously published studies. In our future research, we intend to integrate these features with clinical data to create a multimodal model, as well as generate additional predictive handcrafted features to enhance diagnostic accuracy [113].

The surge in demand for radiologists can be attributed to the rapid growth of medical imaging resulting from advancements in imaging technology. Unfortunately, this increase in demand has also led to a heavier workload for radiologists, which may have contributed to diagnostic errors. The application of AI techniques in clinical medical imaging has significantly enhanced diagnostic accuracy and efficacy. These strategies not only improve diagnosis accuracy, but also bridge the gap between medical professionals with different levels of experience, including generalists and specialists. Osteoporosis detection is one of the most crucial diagnostic procedures that require medical imaging. To address this, we present an AI-based approach for automatically detecting osteoporosis by analyzing X-rays [14].

The present study involves the development of a diagnostic model for osteoporosis through the creation of handcrafted features, which were extracted from descriptors generated by performing a comprehensive analysis of bone images using a set of Gabor filters featuring varying orientations. The raw image was examined using this specific set of Gabor filters before applying the feature extraction method.

In this study, we utilized the Histogram of Oriented Gradient (HOG) and Local Phase Quantification (LPQ) to extract features from the resulting descriptor. To achieve optimal performance, we utilized a bat-based optimization strategy to select the best Gabor filter settings. Additionally, our proposed method can make use of the multimodality principle by combining HOG and LPQ data or conducting texture analysis with various filter sizes.

Furthermore, in this study, we combined data at two distinct levels: the decision level and the score level. We aimed to cover all aspects of system development and our tests yielded positive results, outperforming several previously published studies with an accuracy of 89.66%. In future work, we plan to develop a multimodality model by combining these features with clinical data. Additionally, utilizing more predictive handcrafted features can further enhance the accuracy of the diagnosis.

Improving follow-up care and identifying personnel with a higher risk of fracture can lead to prompt treatment and cost-effective management of osteoporosis, which can ultimately reduce downstream costs. However, despite its advantages, DXA is not widely accessible or cost-effective, and it is not a comprehensive solution. Therefore, it is essential to develop a diagnostic system that is reliable, easily available, cost-effective, and clinically acceptable. In this review study, a computer-aided diagnosis (CAD) system using machine learning techniques was explored for the automatic detection and diagnosis of osteoporosis, incorporating various imaging modalities such as X-rays, DXA scans, MRIs, and CT scans of the vertebrae. The process of detecting osteoporosis involves acquiring images, preprocessing, segmenting the region of interest, extracting features, and using classifiers based on machine learning techniques. It was also observed that texture analysis of trabecular microarchitecture using machine learning techniques can improve the sensitivity, specificity, F1-score, and accuracy. The advantage of using machine learning is its self-learning ability, which eliminates the need for further preprocessing. However, the standardization of the dataset is necessary to ensure a universal paradigm. Future research directions could focus on the development of low-cost, widely accessible x-ray diagnostic tools, and the use of deep learning models, which require a large amount of data and automatically learn features from the input data.

Appendix A

Region Of Interest

A.1 Extraction of the Region Of Interest (ROI)

The X-ray images of the calcaneus (heel bone) that we used in this study were acquired according to a standardized protocol, the X-rays of the calcaneus were obtained with a high-resolution direct-scan X-ray machine (BMATM, D3A Medical Systems, Orléans, France) with a focal length set at 1.15 m and X-ray parameters set at 55 kV and 20 mA. The heel is scanned by the device using anatomical landmarks positioned by the operator on the image to correctly extract the Region of Interest (ROI) 400 × 400 pixels. The ROI of the region of interest was defined by a physician by marking easily identifiable anatomical landmarks on the image of the calcaneus [91].

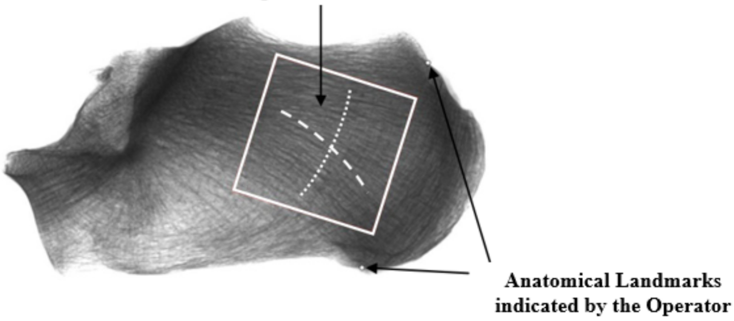

Figure A.1: Extracting the ROI. An x-ray of the calcaneus and its region of interest to be extracted (white square).

This ensures that the ROI (Figure A.1) is acquired in the same region as well as in the same orientation for each bone X-ray, as the effect of orientation on the scan is within the scope of our study. This ROI was located in a part of the calcaneus which contains only the trabecular bone. The role of this phase is to configure and modify the image in order to prepare it, to extract the features.

A.2 Data Acquisition

Bone structure can be easily assessed on traditional radiographs using 2D texture analysis [92][93]. Additionally, numerous research has demonstrated that 2D texture analysis can be used to evaluate 3D microarchitecture indirectly [91][92][93][94][95]. Pattern recognition and medical applications face a significant barrier when assessing osteoporotic illness from bone radiograph images. The degree of resemblance between the textured images of osteoporotic and healthy bone microarchitecture increases the difficulty of distinguishing such textures. This dataset uses texture analysis to separate osteoporotic cases from healthy controls on 2D bone radiograph images. It consists of 87 patients with osteoporotic fractures and 87 control participants in two groups (Figure A.2). The distribution of the fractures is as follows: 21 other fractures, 22 wrist fractures, 22 neck fractures, and 22 spinal compressions.

This dataset of bone X-ray images (encoded 16-bit, TIFF format, 400×400 pixels-size) from Challenge IEEE-ISBI: Bone Texture Characterization, contained 116 images divided into 58 from osteoporotic patients (with fractures) and 58 from healthy people, used for testing and training in creating the model. After this, 58 new images for BLIND classification were used as external validation.

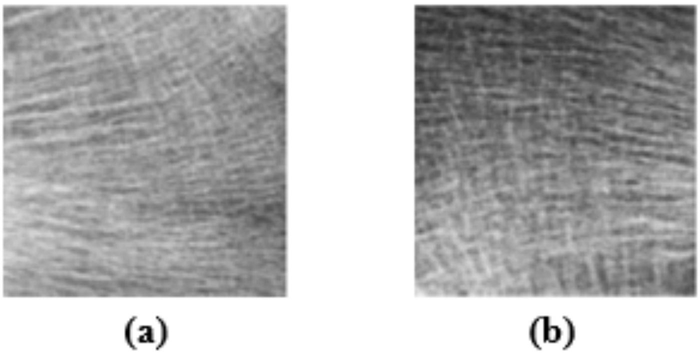

Figure A.2: Control image (a), and Osteoporosis image (b).

Appendix B

Support Vector Machine

A classifier that represents the training data as points in space separated into categories as large a distance as possible. New points are then added to the space by predicting which category they fall into and which space they will belong to. It is highly effective in high-dimensional spaces and requires a small subset of training points in the decision function, making it memory efficient. SVM can be applied not only to nonlinear distribution and regression problems but also to unsupervised problems. As shown in (Figure B.1) The goal is to find the plane with the highest edge, i.e. the maximum distance between points of a given class.

The Support Vector Machines (SVM) classifier is designed to identify a hyperplane (Equation B.1) that can accurately separate two classes while maximizing the margin between them [96].

$$g(x) = w^T x + b \tag{B.1}$$

The process of learning an SVM involves solving a constrained optimization problem that aims to minimize the following objective function:

$$j(w, b, \varepsilon) = \frac{1}{2} \parallel w \parallel^2 + c \sum_{i=1}^{N} \varepsilon_i \tag{B.2}$$

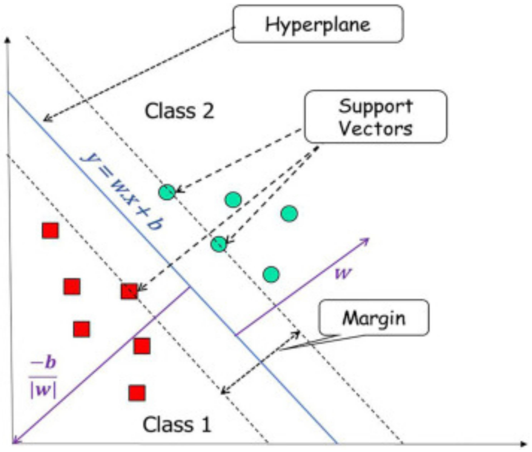

Figure B.1: Components of Support Vector Machine.

The optimization problem for learning an SVM is subject to certain constraints, which must be satisfied during the process of optimization:

$$\begin{cases} y_i[x_i w_i + b] \geq 1 - \varepsilon_i \\ \varepsilon_i \geq 0 \end{cases} \quad i = 1, 2, ..., N \tag{B.3}$$

The margin size control parameter is denoted by C, and it plays a crucial role in the optimization problem for learning an SVM. To construct the Lagrangian function for SVM, a weighted sum of the constraints is added to the objective function:

$$\mathcal{L} = \frac{1}{2} \parallel w \parallel^2 + c \sum_{i=1}^{N} \varepsilon_i - \sum_{i=1}^{N} \alpha_i [y_i[x_i w_i + b] - 1 + \varepsilon_i] - \sum_{i=1}^{N} \mu_i \varepsilon_i \tag{B.4}$$

Once the relevant processes have been executed, the optimal hyperplane orientation is determined by the values obtained for w and b.

$$w = \sum_{i=1}^{N} \alpha_i y_i x_i \tag{B.5}$$

and

$$b = \frac{1}{N_s} \sum_{s \in S} (y_s - \sum_{m \in S} \alpha_m y_m x_m . x_s) \tag{B.6}$$

In the equation used to classify each new point x_{new}, S refers to the set of indices of the Support Vectors, which are defined by $i/\alpha_i > 0$, while x_s denotes the data point that satisfies the condition $\sum_{i=1}^{N} \alpha_i y_i = 0$. The classification of x_{new} is performed by computing the following formula:

$$y_{new} = sgn(w_i.x_{new} + b) \tag{B.7}$$

Appendix C

Performance Evaluation

The performance of a laboratory test is usually assessed by its sensitivity, specificity, and positive and negative predictive values. However, these indices only imperfectly reflect the ability of a test to distinguish the disease from non-disease and cannot classify it concerning pre-existing tests. The use of the Receiver Operating Characteristic (ROC) curve seems to be a necessary tool to overcome these limits.

C.1 Receiver Operating Characteristics

Originally developed in the 1950s for military purposes (using Radar data), its interest in the medical field was emphasized by Lee Lusted in 1960. Since then, this statistical tool has been used especially in the pharmaceutical field, radiology, and biology.
The ROC curve is a graphical representation of the relationship between test sensitivity and specificity, calculated for all possible cut-off values [100]. It is a useful technique for organizing classifiers and visualizing their performance, it facilitates our classifier concept and is, therefore, useful for classification data and learning.

C.2 Test Characteristic

For a given osteoporosis condition, the best possible test can be selected based on the calculated Accuracy (ACC), Specificity (SPE), Sensitivity (SEN), and F-score which are widely used statistics to describe the osteoporosis test. In particular, they are used to determine the quality and reliability of the test. These features are described in terms of True Positive (TP), True Negative (TN), False Positive (FP), and False Negative (FN).

$$ACC = \frac{TP + TN}{TP + TN + FP + FN} \tag{C.1}$$

$$SEN = \frac{TP}{TP + FN} \tag{C.2}$$

$$SPE = \frac{TN}{TN + FP} \tag{C.3}$$

$$F - score = \frac{2TP}{2TP + FN + FP} \tag{C.4}$$

Accuracy and F-score are often used in classification quality assessment. Accuracy is the probability that the test correctly classifies subjects. F-score is a measure of the accuracy of a test. It considers both the Accuracy and Sensitivity of the test to calculate the Score, it can be interpreted as a weighted average of Accuracy and Sensitivity, where an F-score ∈[0,1], a perfect classifier has an F -score = 1, on the other hand, a bad one, has an F-score = 0.

The Area Under the Curve (AUC) is also calculated, to measure the ability of a classifier to distinguish between classes, this is because the higher the AUC, the better the performance of the model in distinguishing positive and negative classes.

We summarize the classifier results of the test data for each class in a matrix called the confusion matrix, as shown in (Figure C.1)

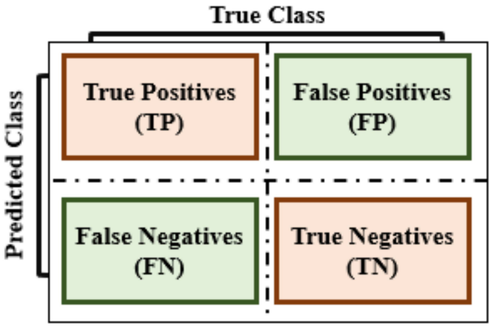

Figure C.1: Confusion Matrix Model [98].

The ordinate represents the SEN and the abscissa corresponds to the quantity (1 -

SPE) (Figure C.2). Its construction requires an adequate computer program. The test results are ranked in descending order and for each threshold value, a Confusion Matrix identical to (Figure C.1) is produced. The calculation of the numbers TP, FP, TN, and FN makes it possible to deduce the Sensitivity and Specificity of the test for each value obtained. The couples 1 – Specificity, Sensitivity are then placed on the curve. Joining them with straight lines leads to a stepped path connecting the lower left corner of the graph (SEN = 0 and SPE = 1) to the upper right corner (SEN = 1 and SPE = 0).

To obtain a quantitative Evaluation of the Classification Performance, from the ROC curve, we use the Area Under this Curve, generally noted as AUC [103]. Since the AUC is a portion of the area of a unit square, its value is always between 0 and 1. The closer the AUC value is to 1, the better the classification result. In the ideal case, the area under the ROC curve is equal to 1, while in the case of a failed system, the area is equal to 0.5 (Figure C.2). The bleu curve has the value of the AUC which is closer to 1 than to 0.5, this curve, therefore, represents good classification results.

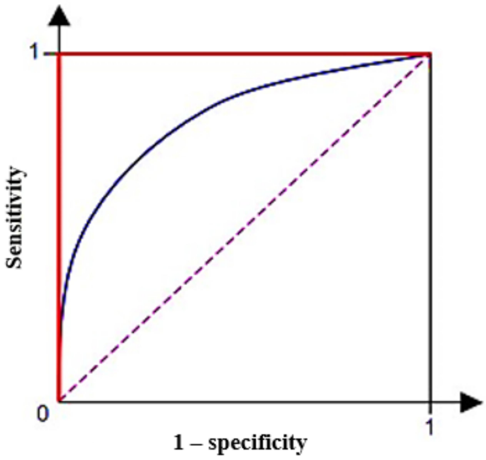

Figure C.2: Interpretation of the ROC Curve. Perfect Diagnostic Test (red line) AUC=1, a very informative Diagnostic Test (blue line) AUC between 0.5 and 1, and a zero contribution Diagnostic test that does not discriminate between individuals (dashed line) AUC=0.5 [99].

Although most of the authors use the AUC as a single criterion for evaluating the performance of the classification method, other statistical criteria derived from the analysis of the ROC curves can be used in (Equation C.1).

Appendix D

Data Fusion

Feature Level Fusion

Data fusion is a technique used to process information from multiple sources [104]. It consists of combining data from several sources to obtain a better decision. Data fusion was originally developed in a military context for purposes such as locating enemy targets and the fusion of radar images. The systems used to use various techniques from various fields such as Signal Processing, Artificial Intelligence, Pattern Recognition, Classification, etc.

In general, data fusion is an operation of integrating several data to extract new information that is more representative of all the data. Currently, data fusion is becoming increasingly important in many areas. It makes it possible to effectively help scientists to extract increasingly relevant and precise information. Data fusion initially aimed to improve the quality of responses to problems posed by the military, but today it greatly affects areas such as [107]: remote sensing, weather forecasting, multimodal biometrics, application medicine, and robotics.

Numerous techniques have been described in the literature for implementing feature-level fusion. Among these, Canonical Correlation Analysis (CCA) and Discriminant Correlation Analysis (DCA) are commonly used.

D.1 Canonical Correlation Analysis (CCA)

The useful multi-data processing technique of CCA has been used frequently to examine the interrelationships between two sets of variables.

Assume that $X \in \mathbb{R}^{p \times n}$ and $Y \in \mathbb{R}^{q \times n}$ are two matrices that each contain n training feature vectors from two distinct modalities. That is, for each sample, two feature vectors with p and q dimensions are extracted from the first and second modalities, respectively.

Let $S_{xx} \in \mathbb{R}^{p \times p}$ and $S_{yy} \in \mathbb{R}^{q \times q}$ denote the within-sets covariance matrices of X and Y and $S_{xy} \in \mathbb{R}^{p \times q}$ denote the between-set covariance matrix (note that $S_{yx} = S_{xy}^T$). The overall $(p+q) \times (p+q)$ covariance matrix, S, consists of all the information on associations between pairs of features:

$$S = \begin{pmatrix} cov(x) & cov(x,y) \\ cov(y,x) & cov(y) \end{pmatrix} = \begin{pmatrix} S_{xx} & S_{xy} \\ S_{yx} & S_{yy} \end{pmatrix} \tag{D.1}$$

Understanding the links between these two sets of feature vectors from this matrix is challenging, as the correlation between these two sets of feature vectors might not follow a regular pattern [104].

CCA aims to find the linear combinations, $\dot{X} = W_x^T X$ and $\dot{Y} = W_y^T Y$ that maximize the pair-wise correlations across the two feature sets:

$$corr(\dot{X}, \dot{Y}) = \frac{cov(\dot{X}, \dot{Y})}{var(\dot{X}).var(\dot{Y})} \tag{D.2}$$

where $cov(\dot{X}, \dot{Y}) = W_x^T S_{xy} W_y, var(\dot{X}) = W_x^T S_{xx} W_x$ and $var(\dot{X}) = W_x^T S_{xx} W_x$ Maximization is performed using Lagrange multipliers by maximizing the covariance between $\dot{X}$ and $\dot{Y}$subject to the constraints $var(\dot{X}) = var(\dot{Y}) = 1$. The transformation matrices, W_x and W_y, are then found by solving the eigenvalue (Equation D.3) [105]:

$$\begin{cases} S_{xx}^{-1} S_{xy} S_{yy}^{-1} S_{yx} \widehat{W}_x = R^2 \widehat{W}_x \\ S_{yy}^{-1} S_{yx} S_{xx}^{-1} S_{xy} \widehat{W}_y = R^2 \widehat{W}_y \end{cases} \tag{D.3}$$

where $\widehat{W}_x$ and $\widehat{W}_y$ are the eigenvectors and R^2 is the diagonal matrix of eigenvalues or squares of the canonical correlations. The number of non-zero eigenvalues in each equation is $d = rank(S_{xy}) \leq min(n;p;q)$, which will be sorted in decreasing order, $r_1 \geq r_2 \geq ::: \geq r_d$. The transformation matrices, W_x and W_y, consist of the sorted eigenvectors corresponding to the non-zero eigenvalues. $\dot{X}$,$\dot{Y} \in \mathbb{R}^{d \times n}$ are known as canonical variates.

Feature-level fusion, as described in [104], is performed either by concatenation or summation of the transformed feature vectors:

$$Z_1 = \begin{pmatrix} \dot{X} \\ \dot{Y} \end{pmatrix} = \begin{pmatrix} W_x^T X \\ W_y^T Y \end{pmatrix} \tag{D.4}$$

or

$$Z_2 = \dot{X} + \dot{Y} = W_x^T X + W_y^T Y \tag{D.5}$$

D.2 Discriminant Correlation Analysis (DCA)

Assume that there are c distinct classes from which the samples in the data matrix are collected. Accordingly, the n columns of the data matrix are divided into c separate groups, where n_i columns belong to the i^{th} class ($n = \sum_{i=1}^{c} n_i$). Let $x_{ij} \in X$ denotes the feature vector corresponding to the j^{th} sample in the i^{th} class. $\bar{x_i}$ and $\bar{x}$ denote the means of the x_{ij} vectors in the i^{th} class and the whole feature set, respectively. That is, $\bar{x_i} = \frac{1}{n_i} \sum_{j=1}^{n_i} x_{ij}$ and $\bar{x} = \frac{1}{n} \sum_{i=1}^{c} \sum_{j=1}^{n_i} x_{ij} = \frac{1}{n} \sum_{i=1}^{c} n_i \bar{x_i}$

The between-class scatter matrix is defined as [107]:

$$S_{bx(p \times p)} = \sum_{i=1}^{c} n_i (\bar{x_i} - \bar{x})(\bar{x_i} - \bar{x})^T = \phi_{bx} {\phi_{bx}}^T \tag{D.6}$$

$$\phi_{bx(p \times c)} = [\sqrt{n_1}(\bar{x_1} - \bar{x}), \sqrt{n_2}(\bar{x_2} - \bar{x}), ..., \sqrt{n_c}(\bar{x_c} - \bar{x})] \tag{D.7}$$

If the classes were well-separated, $\phi^T \phi$ would be a diagonal matrix. Since $\phi^T \phi$ is symmetric positive semi-definite, we can find transformations that diagonalize it:

$$P^T (\phi_{bx}^T \phi_{bx}) P = \widehat{\Lambda} \tag{D.8}$$

where P is the matrix of orthogonal eigenvectors. Let $\mathcal{Q}_{(c \times r)}$ consist of the first r eigenvectors, which correspond to the r largest nonzero eigenvalues, from matrix P. We have:

$$\mathcal{Q}^T (\phi_{bx}^T \phi_{bx}) \mathcal{Q} = \Lambda_{(r \times r)} \tag{D.9}$$

The r most significant eigenvectors of S_{bx} can be obtained with the mapping $\mathcal{Q} \longrightarrow \phi_{bx}\mathcal{Q}$:

$$(\phi_{bx}\mathcal{Q})^T S_{bx}(\phi_{bx}\mathcal{Q}) = \Lambda_{(r\times r)} \tag{D.10}$$

if $W_{bx} = \phi_{bx}\mathcal{Q}\Lambda^{-1/2}$, we have:

$$W_{bx}^T S_{bx} W_{bx} = I \tag{D.11}$$

$$\acute{X}_{(r\times n)} = W_{bx(r\times p)}^T X_{(p\times n)} \tag{D.12}$$

$\acute{X}$ is the projection of X in a space, where the between-class scatter matrix is I and the classes are separated. Similarly:

$$W_{by}^T S_{by} W_{by} = I \tag{D.13}$$

$$\acute{Y}_{(r\times n)} = W_{by_{(r\times p)}}^T Y_{(p\times n)} \tag{D.14}$$

Although $\acute{S}_{bx} = \acute{S}_{by} = I$, the matrices $\acute{\phi}_{bx}^T\acute{\phi}_{bx}$ and $\acute{\phi}_{by}^T\acute{\phi}_{by}$ are strict diagonally dominant matrices. This makes the centroids of the classes have minimal correlation with each other, and thus, the classes are separated.

Now that the between-class scatter matrices are unitized, we need to make the features in one set have nonzero correlation only with their corresponding features in the other set. Therefore, we diagonalize the between-set covariance matrix $\acute{S}_{xy} = \acute{X}\acute{Y}^T$.

$$\acute{S}_{xy_{(r\times r)}} = U\sum V^T \Longrightarrow U^T\acute{S}_{xy}V = \sum(\underbrace{U\sum^{-1/2}}_{W_{cx}})^T\acute{S}_{xy}(\underbrace{V\sum^{-1/2}}_{W_{cy}}) = I \tag{D.15}$$

Transformation:

$$\dot{X} = W_{cx}^T\dot{X} = \underbrace{W_{cx}^T W_{bx}^T}\, X = W_x X \tag{D.16}$$

$$\dot{Y} = W_{cy}^T\dot{Y} = \underbrace{W_{cy}^T W_{by}^T}\, Y = W_y Y \tag{D.17}$$

Feature fusion:

$$Z_1 = \begin{pmatrix} \dot{X} \\ \dot{Y} \end{pmatrix} = \begin{pmatrix} W_x^T X \\ W_y^T Y \end{pmatrix} \tag{D.18}$$

or:

$$Z_2 = \dot{X} + \dot{Y} = W_x^T X + W_y^T Y \tag{D.19}$$

Appendix E

Scientific Production

E.1 Publications

1. Meriem Mebarkia, Abdallah Meraoumia, Lotfi Houam, Seddik Khemaissia, "*X-ray image analysis for osteoporosis diagnosis: From shallow to deep analysis,*" Displays, vol. 76, 2023, 102343, ISSN 0141-9382, doi:10.1016/j.displa. 2022.102343

E.2 Indexed International Conferences

E.2.1 IEEE Xplore Database

1. Meriem Mebarkia, Abdallah Meraoumia, Lotfi Houam, Seddik Khemaissia, Amel Bouchamha and Rachid Jennane, "*Hierarchical Multiscale Local Binary Pattern For Better Osteoporosis Detection,*" 2021 IEEE 1st International Maghreb Meeting of the Conference on Sciences and Techniques of Automatic Control and Computer Engineering MI-STA, Tripoli, Libya, 2021, pp. 387-392, doi: 10.1109/MI-STA52233.2021.9464493.

2. Meriem Mebarkia, Abdallah Meraoumia, Lotfi Houam and Seddik Khemaissia, "*Trabecular Bone Microarchitecture Assessment and Fracture Risk Prediction Using Machine Learning Techniques: A Short Review,*" 2021 IEEE 1st International Maghreb Meeting of the Conference on Sciences and Techniques of Automatic Control and Computer Engineering MI-STA, Tripoli, Libya, 2021, pp. 872-876, doi: 10.1109/MI-STA52233.2021.9464362.

3. Meriem Mebarkia, Abdallah Meraoumia, Lotfi Houam and Seddik Khemaissia, "*A Hierarchical Prototype-Based Approach for Osteoporosis Classification,*" 2021 International Conference on Recent Advances in Mathematics and Informatics (ICRAMI), Tebessa, Algeria, 2021, pp. 1-6, doi: 10.1109/ICRAMI52622.2021.9585919.

4. Meriem Mebarkia, Abdallah Meraoumia, Lotfi Houam, Seddik Khemaissia, "*Evaluation of Local Binary Pattern for Osteoporosis Classification,*" 2022 2nd International Conference on New Technologies of Information and Communication (NTIC), Mila, Algeria, 2022, pp. 1-6, doi: 10.1109/NTIC55069.2022.10100543.

E.2.2 Springerlink database

1. Meriem Mebarkia, Abdallah Meraoumia, Lotfi Houam, Seddik Khemaissia,and Rachid Jennane, " *Multi-resolution Texture Analysis for Osteoporosis Classification,* 2021 International Conference on Digital Technologies and Applications (ICDTA'21), Fez, Moroco, 2021, vol 211 pp. pp 769–779, doi: 10.1007/978-3-030-73882-2-70.

E.3 International Communications

1. Lotfi Houam, Abdallah Meraoumia, Meriem Mebarkia, Seddik Khemaissia,and Rachid Jennane,"*Improved Osteoporosis Detection AccuracyThrough Ensemble Classification,* 2021 International Conference on Embedded Systems and Artificial Intelligence (ESAI'21), Fez, Moroco, 2021.

E.4 Workshop

1. Meriem Mebarkia, 2020 Student Workshop on Electrical Engineering Virtual conference via ZOOM (SWEE 2020), Hangzhou, China, December 26, 2020.

2. Meriem Mebarkia, 2023 Workshop on Artificial Intelligence for Smart Agriculture, "Smart Agri-Tech", El Oued, Algeria, February 22-23, 2023.

Abbreviations

AI	Artificial Inteligence	12
ML	Machine Learning	14
DL	Deep Learning	16
CAD	Computer-Aided Diagnosis	17
CADe	Computer Aided Detection	18
CADx	Computer Aided Diagnosis	17
WHO	World Health Organization	41
BMD	Bone Mineral Density	41
DEXA	Dual-Energy X-ray Absorptiometry	42
QCT	Quantitative Computed Tomography	42

CT Computed Tomography 42

MRI Magnetic Resonance Image 42

HOG Histogram of Oriented Gradient 59

LPQ Local Phase Quantization 64

STFT Short-Term Fourier Transform 64

PSF Point Spread Function 66

ACF The Autocorrelation Function 68

CLAHE Contrast Limited Adaptive Histogram Equalization 82

PHOG Pyramid of Histogram of Oriented Gradients 82

LBP Local Binary Pattern 82

GDP Gradient Directional Pattern 82

IWBC Improved Weber Binary Coding 82

OLP Overlap 86

GBR	Gabor	90
AVR	Average	96
CAT	Concatenation	96
SUM	Sum of the Scores	97
MIN	Minimum of the Scores	97
MUL	Product of the Scores	97
MAX	Maximum of the scores	97
ROI	Region of Interest	107
ACC	Accuracy	112
ROC	Receiver Operating Characteristic	112
SEN	Sensitivity	112
SPE	Specificity	112
AUC	Area Under the Curve	113

CCA Canonical Correlation Analysis 115

125

DCA Discriminant Correlation Analysis 115

Bibliography

[1] Jha, Saurabh, and Eric J Topol. *Adapting to Artificial Intelligence: Radiologists and Pathologists as Information Specialists.* JAMA vol. 316,22 (2016): 2353-2354. doi:10.1001/jama.2016.17438

[2] Chartrand, Gabriel et al. *Deep Learning: A Primer for Radiologists.* Radiographics: a review publication of the Radiological Society of North America, Inc vol. 37,7 (2017): 2113-2131. doi:10.1148/rg.2017170077

[3] Bohr, A. and Memarzadeh, K. *Artificial intelligence in healthcare.* San Diego: Elsevier, Science & Technology. (2020).

[4] Reddy, Sandeep et al. *Artificial intelligence-enabled healthcare delivery.* Journal of the Royal Society of Medicine vol. 112,1 (2019): 22-28. doi:10.1177/0141076818815510

[5] Lakhani, Paras et al. *Machine Learning in Radiology: Applications Beyond Image Interpretation.* Journal of the American College of Radiology : JACR vol. 15,2 (2018): 350-359. doi:10.1016/j.jacr.2017.09.044

[6] Lynn, Lawrence A. *Artificial intelligence systems for complex decision-making in acute care medicine: a review.* Patient safety in surgery vol. 13 6. 1 Feb. 2019, doi:10.1186/s13037-019-0188-2

[7] Mueller, Dirk, and Afschin Gandjour. *Cost-effectiveness of using clinical risk factors with and without DXA for osteoporosis screening in postmenopausal women.* Value in health : the journal of the International Society for Pharmacoeconomics and Outcomes Research vol. 12,8 (2009): 1106-17. doi:10.1111/j.1524-4733.2009.00577.x

[8] Singh, Anushikha et al. *Classification of the trabecular bone structure of osteoporotic patients using machine vision.* Computers in biology and medicine vol. 91 (2017): 148-158. doi:10.1016/j.compbiomed.2017.10.011

[9] Lambin, Philippe et al. *Radiomics: the bridge between medical imaging and personalized medicine.* Nature reviews. Clinical oncology vol. 14,12 (2017): 749-762. doi:10.1038/nrclinonc.2017.141

[10] Davnall, Fergus et al. *Assessment of tumor heterogeneity: an emerging imaging tool for clinical practice?.* Insights into imaging vol. 3,6 (2012): 573-89. doi:10.1007/s13244-012-0196-6

[11] Office of the Surgeon General (US). *Bone Health and Osteoporosis: A Report of the Surgeon General.* Office of the Surgeon General (US), 2004.

[12] U.S. Preventive Services Task Force. *Screening for osteoporosis: U.S. preventive services task force recommendation statement.* Annals of internal medicine vol. 154,5 (2011): 356-64. doi:10.7326/0003-4819-154-5-201103010-00307

[13] Mitchell, P J. *Fracture Liaison Services: the UK experience.* Osteoporosis international : a journal established as result of cooperation between the European Foundation for Osteoporosis and the National Osteoporosis Foundation of the USA vol. 22 Suppl 3 (2011): 487-94. doi:10.1007/s00198-011-1702-2

[14] Lochmüller, Eva-Maria et al. *Effect of Fixation, Soft-Tissues, and Scan Projection on Bone Mineral Measurements with Dual Energy X-ray Absorptiometry (DXA).* Calcified Tissue International vol. 68 (2001): 140-145. doi:10.1007/s002230001192

[15] Kruse, Christian et al. *Machine Learning Principles Can Improve Hip Fracture Prediction.* Calcified tissue international vol. 100,4 (2017): 348-360. doi:10.1007/s00223-017-0238-7

[16] Bercovich, Eyal, and Marcia C Javitt. *Medical Imaging: From Roentgen to the Digital Revolution, and Beyond.* Rambam Maimonides medical journal vol. 9,4 e0034. 4 Oct. 2018, doi:10.5041/RMMJ.10355

[17] Adams, Matthew et al. *Computer vs human: Deep learning versus perceptual training for the detection of neck of femur fractures.* Journal of medical imaging and radiation oncology vol. 63,1 (2019): 27-32. doi:10.1111/1754-9485.12828

[18] Sampat, Mehul P. et al. *Computer-Aided Detection and Diagnosis in Mammography.* (2005). Corpus ID: 2643752

[19] Lawson, C. E., Martí, J. M., Radivojevic, T., Jonnalagadda, S. V. R., Gentz, R., Hillson, N. J., Garcia Martin, H. *Machine learning for metabolic engineering: A review.* Metabolic Engineering,(2021). vol. 63, 34–60. doi:10.1016/j.ymben.2020.10.005

[20] J. Keith Fisher, M.D. Amanda Barrell *Medically reviewed* on June 17, 2019

[21] Yan, Lijin, and Zhiqi Huang. *Application value and feasibility analysis of humanistic health management for cancer screening in physical examination.* American journal of translational research vol. 13,12 14229-14237. 15 Dec. 2021

[22] Osborne, Jacqueline A et al. *Physical Therapist Management of Parkinson Disease: A Clinical Practice Guideline From the American Physical Therapy Association.* Physical therapy vol. 102,4 (2022): pzab302. doi:10.1093/ptj/pzab302

[23] Xi, Xue-Jiao et al. *Bronchobiliary fistula following radiofrequency ablation for liver metastases from breast cancer: A case report and literature review.* Medicine vol. 97,43 (2018): e12760. doi:10.1097/MD.0000000000012760

[24] Nischal, Urmila et al. *Techniques of skin biopsy and practical considerations.* Journal of cutaneous and aesthetic surgery vol. 1,2 (2008): 107-11. doi:10.4103/0974-2077.44174

[25] Zhang, Yongde et al. *Design and experimental study of a novel 7-DOF manipulator for transrectal ultrasound probe.* Science progress vol. 103,4 (2020): 36850420970366. doi:10.1177/0036850420970366

[26] Kumar, Yogesh et al. *Artificial intelligence in disease diagnosis: a systematic literature review, synthesizing framework and future research agenda.* Journal of ambient intelligence and humanized computing, 1-28. 13 Jan. 2022, doi:10.1007/s12652-021-03612-z

[27] Zhang, Q., Lu, J., & Jin, Y. (2020). *Artificial intelligence in recommender systems.* Complex & Intelligent Systems, 7(1), 439–457. doi:10.1007/s40747-020-00212-w

[28] Hashimoto, Daniel A et al. *Artificial Intelligence in Anesthesiology: Current Techniques, Clinical Applications, and Limitations.* Anesthesiology vol. 132,2 (2020): 379-394. doi:10.1097/ALN.0000000000002960

[29] Erb, Benjamin. *Artificial Intelligence & Theory of Mind.* (2016). Doi: 10.13140/RG.2.2.27105.71526.

[30] Sarker, Iqbal H. *Machine Learning: Algorithms, Real-World Applications and Research Directions.* SN computer science vol. 2,3 (2021): 160. doi:10.1007/s42979-021-00592-x

[31] Jiang, Tammy et al. *Supervised Machine Learning: A Brief Primer.* Behavior therapy vol. 51,5 (2020): 675-687. doi:10.1016/j.beth.2020.05.002

[32] Lee, Joonsang et al. *Unsupervised machine learning for identifying important visual features through bag-of-words using histopathology data from chronic kidney disease.* Scientific reports vol. 12,1 4832. 22 Mar. 2022, doi:10.1038/s41598-022-08974-8

[33] Sarker, I.H., Kayes, A.S.M., Badsha, S., Alqahtani, H., Watters, P. and Ng, A. *Cybersecurity Data Science: An Overview from Machine Learning Perspective.* Journal of Big Data,(2020). vol 7, 1-29.https://doi.org/10.1186/s40537-020-00318-5

[34] Mohammed, M., Khan, M.B., & Bashier, E.B.M. . *Machine Learning: Algorithms and Applications.* CRC Press.(2016). https://doi.org/10.1201/9781315371658

[35] Niraula, Dipesh et al. *Quantum deep reinforcement learning for clinical decision support in oncology: application to adaptive radiotherapy.* Scientific reports vol. 11,1 23545. 7 Dec. 2021, doi:10.1038/s41598-021-02910-y

[36] Nadeem, Muhammad Waqas et al. *Deep Learning for Diabetic Retinopathy Analysis: A Review, Research Challenges, and Future Directions.* Sensors (Basel, Switzerland) vol. 22,18 6780. 8 Sep. 2022, doi:10.3390/s22186780

[37] Ferrante di Ruffano, Lavinia et al. *Computer-assisted diagnosis techniques (dermoscopy and spectroscopy-based) for diagnosing skin cancer in adults.* The Cochrane database of systematic reviews vol. 12,12 CD013186. 4 Dec. 2018, doi:10.1002/14651858.CD013186

[38] Lee, Juhun et al. *Optimal reconstruction and quantitative image features for computer-aided diagnosis tools for breast CT.* Medical physics vol. 44,5 (2017): 1846-1856. doi:10.1002/mp.12214

[39] Joseph, Seena, and Oludayo O Olugbara. *Preprocessing Effects on Performance of Skin Lesion Saliency Segmentation.* Diagnostics (Basel, Switzerland) vol. 12,2 344. 29 Jan. 2022, doi:10.3390/diagnostics12020344

[40] P. K. Singh, V. Chaudhary, S. Jain and G. A. Kumar, *Compare and Contrast of Machine Learning Classification Algorithms to Predict Accuracy and Performance of*

Lung Cancer Disease. 2021 International Conference on Technological Advancements and Innovations (ICTAI), Tashkent, Uzbekistan, 2021, pp. 96-101, doi: 10.1109/ICTAI53825.2021.9673483.

[41] Benyahia Souad Née Belaidi, *Application de la classe des méthodes d'apprentissagestatistique SVM (support vector machine) pour la reconnaissance des formes dans lesimages*, thesis to obtain the title of magister in computer science 2012.

[42] R. C. Gonzalez and R. E. Woods, *Digital Image Processing.* Third Edition, 2008

[43] Das, K. N., Bansal, J. C., Deep, K., Nagar, A. K., Pathipooranam, P., & Naidu, R. C. (Eds.). *Soft Computing for Problem Solving.* Advances in Intelligent Systems and Computing. (2020). doi:10.1007/978-981-15-0035-0

[44] Caspers, Julian et al. *Automated age- and sex-specific volumetric estimation of regional brain atrophy: workflow and feasibility.* European radiology vol. 31,2 (2021): 1043-1048. doi:10.1007/s00330-020-07196-8

[45] Li, Y., Zhang, C. C., Kathrin Weidacker, Zhang, Y., He, N., Jin, H., … Yan, F. *Investigation of anterior cingulate cortex gamma-aminobutyric acid and glutamate-glutamine levels in obsessive-compulsive disorder using magnetic resonance spectroscopy.* BMC Psychiatry,(2019). vol 19(1). doi:10.1186/s12888-019-2160-1

[46] Kawala, François. *Activity prediction in social-networks.* (2015).

[47] Nithiyaraj, Emerson & Pushparaj, Vijayakumari. *FPGA Based Real Time Classification With Support Vector Machine.* (2017).

[48] Zhao, Xin, Li, Yang, & Chen. *A Heterogeneous Ensemble Learning Framework for Spam Detection in Social Networks with Imbalanced Data.* Applied Sciences,(2020). vol 10(3), 936. doi:10.3390/app10030936 .

[49] H. Soltani, M. Amroune, I. Bendib and M. Y. Haouam, *Breast Cancer Lesion Detection and Segmentation Based On Mask R-CNN.* 2021 International Conference on Recent Advances in Mathematics and Informatics (ICRAMI), Tebessa, Algeria, 2021, pp. 1-6, doi: 10.1109/ICRAMI52622.2021.9585913.

[50] Cornelius, Carolin et al. *Cellular stress response, sirtuins and UCP proteins in Alzheimer disease: role of vitagenes.* Immunity & ageing : I & A vol. 10,1 41. 17 Oct. 2013, doi:10.1186/1742-4933-10-41

[51] MATSUSHITA, N., ARUGA, A., INOUE, Y., KOTERA, Y., TAKEDA, K., & YAMAMOTO, M. (2013). *Phase I clinical trial of a peptide vaccine combined with tegafur-uracil plus leucovorin for treatment of advanced or recurrent colorectal cancer.* Oncology Reports, 29(3), 951–959. doi:10.3892/or.2013.2231

[52] Sözen, Tümay et al. *An overview and management of osteoporosis.* European journal of rheumatology vol. 4,1 (2017): 46-56. doi:10.5152/eurjrheum.2016.048

[53] Tucci, Joseph R. *Importance of early diagnosis and treatment of osteoporosis to prevent fractures.* The American journal of managed care vol. 12,7 Suppl (2006): S181-90.

[54] Ruth Dennis, Robert M. Kirberger, Robert H. Wrigley. *Handbook of Small Animal Radiology and Ultrasound: Techniques and Differential Diagnoses.* Churchill Livingstone/Elsevier, 2010. ISBN: 0702028940, 9780702028946

[55] E. N. Marieb, T. Martin, and C. Tonini, *Human anatomy and physiology.*, 4th ed. USA: Menlo Park, Calif. : Benjamin/Cummings, c1998. , 1998.

[56] Gadre, Kiran & Kumar, Balasubramanya & Gadre, Divya. *Panfacial Fractures.* (2021). doi: 10.1007/978-981-15-1346-6-60.

[57] Yoganandan, Narayan et al. *Biomechanics of human thoracolumbar spinal column trauma from vertical impact loading.* Annals of advances in automotive medicine. Association for the Advancement of Automotive Medicine. Annual Scientific Conference vol. 57 (2013): 155-66.

[58] Roothaer, Xavier. *Multi-scale study of the mechanical behaviour of bearing and bone-bearing bones : towards personalization of FE human models.* (2019).

[59] Hammer, A. *The paradox of Wolff's theories.* Irish Journal of Medical Science (1971 -), (2014). 184(1), 13–22. doi:10.1007/s11845-014-1070-y

[60] Marquis, Marie-Eve et al. *Bone cells-biomaterials interactions.* Frontiers in bioscience (Landmark edition) vol. 14,3 1023-67. 1 Jan. 2009, doi:10.2741/3293

[61] Aguado, Eric et al. *Bone mass and bone quality are altered by hypoactivity in the chicken.* PloS one vol. 10,1 e0116763. 30 Jan. 2015, doi:10.1371/journal.pone.0116763

[62] WHO Scientific Group on the Prevention and Management of Osteoporosis. (2000: Geneva, Switzerland) *Prevention and management of osteoporosis : report of a WHO scientific group.* World Health Organization 2003.

[63] NIH Consensus Development Panel on Osteoporosis Prevention, Diagnosis, and Therapy. *Osteoporosis prevention, diagnosis, and therapy.* JAMA vol. 285,6 (2001): 785-95. doi:10.1001/jama.285.6.785

[64] W. A. Peck, *Consensus development conference: diagnosis, prophylaxis, and treatment of osteoporosis.* The American journal of medicine vol. 94,6 (1993): 646-50. doi:10.1016/0002-9343(93)90218-e

[65] Lotfi Houam. *Contribution à l'analyse de textures de radiographies osseuses pour le diagnostic précoce de l'ostéoporose.* University of Orlaans; Université 08 mai 45 Guelma (Algeria), 2013.

[66] Brown, Jacques P et al. *2002 clinical practice guidelines for the diagnosis and management of osteoporosis in Canada.* CMAJ : Canadian Medical Association journal = journal de l'Association medicale canadienne vol. 167,10 Suppl (2002): S1-34.

[67] Bener, Abdulbari, and Najah M Saleh. *Low vitamin D, and bone mineral density with depressive symptoms burden in menopausal and postmenopausal women.* Journal of mid-life health vol. 6,3 (2015): 108-14. doi:10.4103/0976-7800.165590

[68] Alawi, Malak et al. *Dual-Energy X-Ray Absorptiometry (DEXA) Scan Versus Computed Tomography for Bone Density Assessment.* Cureus vol. 13,2 e13261. 10 Feb. 2021, doi:10.7759/cureus.13261

[69] Pisani, Paola et al. *Screening and early diagnosis of osteoporosis through X-ray and ultrasound based techniques.* World journal of radiology vol. 5,11 (2013): 398-410. doi:10.4329/wjr.v5.i11.398

[70] Choplin, R.H., Lenchik, L. & Wuertzer, S. *A Practical Approach to Interpretation of Dual-Energy X-ray Absorptiometry (DXA) for Assessment of Bone Density.* Curr Radiol Rep 2, 48 (2014). https://doi.org/10.1007/s40134-014-0048-x

[71] Mazess, R B et al. *Dual-energy x-ray absorptiometry for total-body and regional bone-mineral and soft-tissue composition.* The American journal of clinical nutrition vol. 51,6 (1990): 1106-12. doi:10.1093/ajcn/51.6.1106

[72] Diez-Perez, Adolfo et al. *Radiofrequency echographic multi-spectrometry for the in-vivo assessment of bone strength: state of the art-outcomes of an expert consensus meeting organized by the European Society for Clinical and Economic Aspects of Osteoporosis, Osteoarthritis and Musculoskeletal Diseases (ESCEO).* Aging clinical and experimental research vol. 31,10 (2019): 1375-1389. doi:10.1007/s40520-019-01294-4

[73] Kaczmarczyk, Grzegorz Piotr et al. *Application of X-ray Computed Tomography to Verify Bond Failures Mechanism of Fiber-Reinforced Fine-Grain Concrete.* Materials (Basel, Switzerland) vol. 15,6 2193. 16 Mar. 2022, doi:10.3390/ma15062193

[74] Stagi, Stefano et al. *Peripheral quantitative computed tomography (pQCT) for the assessment of bone strength in most of bone affecting conditions in developmental age: a review.* Italian journal of pediatrics vol. 42,1 88. 26 Sep. 2016, doi:10.1186/s13052-016-0297-9

[75] Bras, Anthony. (2004). *Potentialities evaluation of EOS.*

[76] Readford, Thomas R et al. *Factors affecting chiropractor requests for full-length spinal radiography: A scoping review.* Journal of medical radiation sciences vol. 69,2 (2022): 236-249. doi:10.1002/jmrs.566

[77] Bharati, M. H., Liu, J. J., & MacGregor, J. F. (2004). *Image texture analysis: methods and comparisons.* Chemometrics and Intelligent Laboratory Systems, 72(1), 57–71. doi:10.1016/j.chemolab.2004.02.005

[78] Lotfi, Houam & Jennane, Rachid & Abdelhani, Boukrouche. (2015). *Contribution à l'Analyse de Textures de Radiographies Osseuses - Application au Diagnostic Précoce de l'Ostéoporose .*

[79] Lotfi, Houam. (2013). *Contribution to texture analysis of bone radiographs for early diagnosis of osteoporosis.*

[80] Yousfi, Laatra & Lotfi, Houam & Abdelhani, Boukrouche & Lespessailles, Eric & Ros, Frederic & Jennane, Rachid. (2019). *Texture Analysis and Genetic Algorithms for Osteoporosis Diagnosis. International Journal of Pattern Recognition and Artificial Intelligence. 34. 10.1142/S0218001420570025.*

[81] Fontes, Liseane & Pereira, Paulo & Pais, Jorge. (2022). *Improvement of the Functional Pavement Quality with Asphalt Rubber Mixtures.*

[82] Zhou, P., Zhang, J., Xue, M., & Lei, B. (2019). *Directional Relative Total Variation for Structure-Texture Decomposition.* IET Image Processing. doi:10.1049/iet-ipr.2018.5133

[83] W. Zhou, S. Gao, L. Zhang, X. Lou, *Histogram of oriented gradients feature extraction from raw bayer pattern images.* IEEE Trans. Circ. Syst. Exp. Briefs 67 (5) (2020) 946–950

[84] Y. Xiao, Z. Cao, L.i. Wang, T. Li, *Local phase quantization plus: a principled method for embedding local phase quantization into Fisher vector for blurred image recognition3.* Inf. Sci. 420 (2017) 77–95.

[85] Dash, S., Senapati, M.R. *Gray level run length matrix based on various illumination normalization techniques for texture classification.* Evol. Intel. 14, 217–226 (2021).

[86] V. Ojansivu, J. Heikkila, *Blur insensitive texture classification using local phase quantization.* in: Proceedings of International Conference on Image and Signal Processing, 2008, pp. 236–243

[87] M Kamaledin Ghiasi-Shirazi, *Learning 2D Gabor filters by infinite kernel learning regression.* J. Comput. Math. Data Sci. 1 (2021) 100016

[88] V. Tadic, Z. Kiraly, P. Odry, *Comparison of gabor filter bank and fuzzified gabor filter for license plate detection.* Acta Polytech. Hungar. 17 (1) (2020) 61–81.

[89] G. C. Jaideva and C. K. Andrew, *Digital Signal Processing Applications* in Fundamentals of Wavelets. Theory, Algorithms, and Applications Hoboken, New Jersey: John Wiley & Sons, Inc, 2011.

[90] R. Shang, Y. Meng, C. Liu, L. Jiao, A.M. Ghalamzan, R.S. Esfahani, *Unsupervised feature selection based on kernel fisher discriminant analysis and regression learning.* Mach. Learn. 108 (2019) 659–686

[91] R. Bartl, B. Frisch, *Osteoporosis: Diagnosis, Prevention, Therapy.* Second ed., Springer, 2009.

[92] S. Hough, *Fast and slow bone losers: Relevance to the management of osteoporosis.* Drug Aging. 12, 1-7, 1998.

[93] E. Martín-Badosa, A. Elmoutaouakkil, S. Nuzzo, D. Amblard, L. Vico, F. Peyrin, *A method for the automatic characterization of bone architecture in 3D mice microtomographic images*, Comput Med Imaging Graph. 27, 447-458, 2003.

[94] R. Jennane, R. Harba, G. Lemineur, S. Bretteil, A. Estrade, C. L. Benhamou, *Estimation of the 3d self-similarity parameter of trabecular bone from its 2D projection.* Med Image Analy., 11(1):91-98, 2007.

[95] R. Jennane, W. J. Ohley, S. Majumdar, G. Lemineur, *Fractal Analysis of Bone X-ray Tomographic Microscopy Projections.* IEEE Trans Medical Imaging 20(5):443–449, 2001.

[96] G. Luo, J. H. Kinney, J. J. Kaufman, D. Haupt, A. Chiabrera, R. S. Siffert, *Relationship between plain radiographic patterns and three-dimensional trabecular architecture in the human calcaneus.* Osteoporos Internat., 9(4):339-345, 1999.

[97] L. Pothuaud, C. L. Benhamou, P. Porion, E. Lespessailles, R. Harba, P. Levitz (2000) *Fractal dimension of trabecular bone projection texture is related to three-dimensional microarchitecture.* Journal Bone Miner. Res. 15(4):691–699, 2000.

[98] L. Pothuaud, P. Carceller, D. Hans, *Correlations between grey-level variations in 2D projection images (TBS) and 3D microarchitecture: applications in the study of human trabecular bone microarchitecture.* Bone 42(4):775–787, 2008.

[99] Huang, Shujun et al. *Applications of Support Vector Machine (SVM) Learning in Cancer Genomics.* Cancer genomics & proteomics vol. 15,1 (2018): 41-51. doi:10.21873/cgp.20063

[100] Nahm, Francis Sahngun. *Receiver operating characteristic curve: overview and practical use for clinicians.* Korean journal of anesthesiology vol. 75,1 (2022): 25-36. doi:10.4097/kja.21209

[101] Bittrich, Sebastian & Kaden, Marika & Leberecht, Christoph & Kaiser, Florian & Villmann, Thomas & Labudde, Dirk. (2019). *Application of an interpretable classification model on Early Folding Residues during protein folding.* BioData Mining. 12. 10.1186/s13040-018-0188-2.

[102] IRSTEA, Mathilde & Isenmann, Marc & Sanz, Thomas & Luque, Sandra. (2012). *Prédiction de la distribution d'alliances de végétation des milieux ouverts d'altitude à l'aide de l'approche dite du maximum d'entropie.* 10.13140/2.1.2352.6720.

[103] Andrew P. Bradley, *The use of the area under the ROC curve in the evaluation of machine learning algorithms.* Pattern Recognition, Vol 30, Issue 7, 1997, https://doi.org/10.1016/S0031-3203(96)00142-2.

[104] Z. Wang, L. Wang, H.a. Huang, *Sparse additive discriminant canonical correlation analysis for multiple features fusion*, Neurocomputing 463 (2021) 185–197

[105] M. Haghighat, M. Abdel-Mottaleb, W. Alhalabi, *Discriminant correlation analysis for feature level fusion with application to multimodal biometrics*, in: IEEEInternational Conference on Acoustics, Speech and Signal Processing (ICASSP), Shanghai, China, 2016, pp. 1866–870

[106] M. Haghighat, M. Abdel-Mottaleb, W. Alhalabi, *Discriminant correlation analysis: real-time feature level fusion for multimodal biometric recognition*, IEEE Trans. Inf. Forensics Secur. 11 (9) (2016) 1984–1996

[107] H.O. lhan, G. Serbes, N. Aydin, *Decision and feature level fusion of deep features extracted from public COVID-19 data-sets*, Appl. Intell. 52 (2022) 8551–8571.

[108] Yang Song, Weidong Cai, Fan Zhang, Heng Huang, Yun Zhou, David Dagan Feng, *Bone texture characterization with fisher encoding of local descriptors*, in: IEEE12th International Symposium on Biomedical Imaging (ISBI), Brooklyn, NY, USA, 2015, pp. 5–8.

[109] Florian Yger, Challenge IEEE-ISBI/TCB: *application of covariance matrices and wavelet marginals*, arXiv: 1410.2663, 2014

[110] S.u. Ran, T. Liu, C. Sun, Q. Jin, R. Jennane, Leyi Wei,*Fusing convolutional neuralnetwork features with hand-crafted features for osteoporosis diagnoses*,Neurocomputing 385 (2020) 300–309.

[111] Ran Su, Weijun Chen, Leyi Wei, Xiuting Li, Qiangguo Jin, Wenyuan Tao, *Encoded texture features to characterize bone radiograph images*, IN: 24th InternationalConference on Pattern Recognition (ICPR), Beijing, China, 2018, pp. 3856–3861

[112] Dhevendra Alagan Palanivel, Sivakumaran Natarajan, Sainarayanan Gopalakrishnan, Rachid Jennane, *Multifractal-based lacunarity analysis oftrabecular bone in radiography*, Compute. Biol. Med. 116 (2020) 103559.

[113] Meriem Mebarkia, Abdallah Meraoumia, Lotfi Houam, Seddik Khemaissia, *X-ray image analysis for osteoporosis diagnosis: From shallow to deep analysis*, Displays, Volume 76, 2023, 102343, ISSN 0141-9382, https://doi.org/10.1016/j.displa.2022.102343.

[114] Jorge Erazo-Aux, H. Loaiza-Correa, A.D. Restrepo-Giron, *Histograms of oriented gradients for automatic detection of defective regions in thermograms*, Appl. Opt. 58(13) (2019) 3620–3629.